UNIVERSITY OF TWENTE.

TNO

CFD-CAA Analysis of Light-Stall Noise Prediction Using DDES and FW-H Analogy for NACA 0012 Airfoil

By

Michael Lawrence Abdulla Zaki - s2207192

A thesis submitted to the University of Twente under the requirements for the degree of Master of Science in Mechanical Engineering.

Engineering Technology – Thermal and Fluid Engineering

Graduation number: 460

Graduation committee members

Chair:	prof.dr.ir. C.H. Venner
University Supervisor:	dr. H. Ozdemir
Company Supervisor:	dr. A. Koodly Ravishankara
External Member:	dr.ir. W.K. den Otter

Host institutions:
University of Twente
TNO Petten

Colloquium date: November 19, 2024

Acknowledgements

I would like to express my deepest gratitude to my supervisor, dr. Huseyin Ozdemir, at the University of Twente for his invaluable guidance, support, and encouragement throughout the course of this research. His expertise and insight have been fundamental to the successful completion of this thesis. I am also deeply thankful to dr. Akshay Koodly Ravishankara at TNO, whose supervision and collaboration provided me with practical insights and direction, enriching the quality of this work. Additionally, I would like to acknowledge the University of Twente for providing the resources and environment that enabled this research, and TNO for their partnership and support in facilitating this project.

Abstract

Accurate noise prediction is crucial, especially for reducing noise in modern aerodynamic applications such as wind turbines, which face challenges in social acceptance due to their acoustic impact. This study focuses on stall noise, which occurs at high angles of attack when the flow over the airfoil becomes separated, leading to increased noise levels. Although models like the Brooks-Pope-Marcolini (BPM) model accurately predict noise at moderate angles of attack before stall, there are no comprehensive models for stall noise, primarily due to the challenges in measuring and predicting stall at high Reynolds numbers.

This study aims to evaluate the use of a CFD-CAA framework, specifically Delayed Detached Eddy Simulations (DDES) coupled with the Ffowcs Williams-Hawkings (FW-H) analogy, to predict far-field noise generated by airfoil self-noise mechanisms, particularly in light-stall conditions. DDES is chosen to address previously mentioned challenges. This hybrid RANS/LES method combines the strengths of RANS for attached boundary layers and LES for separated flows. The surface pressure fluctuations obtained from the numerical flow solution are propagated to far-field observer locations using the FW-H analogy, allowing for noise predictions to be made and compared with experimental data. The CFD analysis of an airfoil in stall requires a large spanwise domain to accurately capture the full vortex structures and predict the emitted noise. However, increasing the domain size while maintaining the necessary mesh resolution to capture small pressure fluctuations can be computationally expensive, often making it impractical. A spanwise correction has been investigated to adjust the acoustic pressure distribution along the span, allowing for a reduction in the required spanwise length of the simulated domain.

The analysis is centered on the NACA0012 airfoil for two cases where the flow and geometrical parameters differ. Case 1 involves an incoming flow speed of 20 m/s, a chord length of 0.3 m, and a span length of 0.45 m. The results of this test case showed good agreement with experimental data in far-field noise spectra. Case 2 considers a higher flow speed of 50 m/s, chord length of 0.12 m, and span length of 0.3 m. The results of this case had large discrepancies when compared to the experimental data for the far-field noise spectra. To investigate these differences, the surface pressure fluctuations and the Reynolds stress were analyzed. It has been deduced that an inadequate time step resolution likely contributed to the observed discrepancies. Additionally, the spanwise correction was investigated to address the challenge of simulating smaller spanwise domains. This correction method effectively scaled the acoustic pressure distribution along the span, resulting in improved noise predictions and reduced computational costs.

Table of Contents

List of Tables

Table **Page**

List of Figures

Figure **Page**

Chapter 1

Introduction

The accurate prediction of airfoil self-noise is a critical aspect of modern aerodynamic research, particularly due to its impact on applications such as wind turbines, helicopter rotors, and aircraft. Among these, the noise generated by flow separation, commonly known as stall noise, presents significant challenges. Stall noise occurs when the boundary layer separates from the airfoil surface, leading to increased noise levels, especially in conditions involving high angles of attack. Unlike trailing edge noise, which is well-documented with established engineering models, stall noise lacks comprehensive modeling due to the complexity of predicting flow separation events.

Given these challenges, numerical and experimental approaches remain the primary methods for stall noise prediction. However, experimental methods often face limitations due to the difficulty in accurately capturing flow characteristics in high Reynolds number conditions and the inherent complexities of wind tunnel testing. This has driven the increasing reliance on Computational Aeroacoustics (CAA) techniques, where hybrid approaches combining Computational Fluid Dynamics (CFD) and acoustic analogies have proven to be effective.

This thesis focuses on utilizing a hybrid CFD-CAA framework, specifically employing Delayed Detached Eddy Simulations (DDES) coupled with the Ffowcs-Williams and Hawkings (FW-H) acoustic analogy, to predict far-field noise generated by light-stall conditions in a NACA 0012 airfoil. DDES offers a balance between computational efficiency and accuracy by resolving turbulent structures in critical flow regions while modeling the rest of the flow with Reynolds-Averaged Navier-Stokes Models (RANS). The FW-H analogy is then used to propagate near-field pressure fluctuations to far-field acoustic observers, enabling comprehensive noise predictions.

The scope of this thesis encompasses the development and validation of this hybrid approach through two distinct test cases. Each case involves different flow conditions and geometrical parameters to evaluate the method's robustness and accuracy. The methodology begins with a thorough literature review of relevant CFD-CAA techniques, focusing on the theoretical foundations of DDES and the FW-H analogy. The chosen numerical schemes, turbulence models,

and spanwise corrections are discussed in detail to justify their application.

Subsequent chapters present the computational setup, including spatial and temporal discretization, boundary conditions, and solver configurations. Validation of the method is performed by comparing the numerical results with available experimental data. This involves an in-depth analysis of surface pressure fluctuations, power spectral density, and far-field noise spectra. The thesis concludes with a discussion of the findings, potential improvements, and recommendations for future work in the field of airfoil noise prediction under stall conditions.

Chapter 2

Background

2.1 Airfoil Aerodynamics and Stall

Understanding the aerodynamics of airfoils is essential to fully grasp the concept of aeroacoustics and airfoil self-noise mechanisms. This section delves into key aspects of airfoil flow characteristics. This includes airfoil aerodynamics, the impact of pressure distribution on lift and drag, the influence of different flow regimes, and the stall phenomenon.

2.1.1 Airfoil Flow Characteristics

Airfoils are specifically designed for wings, blades, and other aerodynamic surfaces to generate lift while minimizing drag. Airfoils shapes come in symmetrical and cambered variations, where symmetrical airfoils have identical upper and lower surfaces, and cambered airfoils have a curved upper surface and a flatter lower surface. Each airfoil design has unique aerodynamic properties suited to its specific applications. For instance, cambered airfoils are more efficient at generating lift force at low angles of attack.

The flow over an airfoil can be categorized into different regimes: laminar, transitional, and turbulent. A Laminar flow regime occurs when the fluid particles move smoothly with orderly layers, which typically happens at low Reynolds numbers. The transitional flow regime, as the name suggests, is a transitional phase between the laminar and turbulent regimes. In a transitional regime, the flow starts to become unstable and inconsistent. A turbulent regime is characterized by unstable and chaotic motion of the fluid. High levels of mixing are present between particles with significant energy dissipation, this happens at higher Reynolds numbers.

The pressure distribution over an airfoil is crucial in determining and understanding the lift and drag forces. As air flows over the airfoil, the fluid particles create a pressure difference between the upper and lower surfaces of the airfoil. This difference is due to higher pressure on the lower surface compared to the upper surface. Consequently, a lifting force perpendicular to the flow velocity and a parallel drag force are created. The pressure distribution changes

with the angle of attack of the airfoil; as the angle increases, lift also increases until reaching a critical point where flow separation occurs at higher angles. This phenomenon is known as stall.

2.1.2 Stall phenomenon

Stall occurs when an airfoil reaches an angle of attack where flow separation happens as the flow over the upper surface is unable to overcome the adverse pressure gradient. At small angles of attack, flow separation begins even though the attached flow over the wing remains dominant. The size of the separated region rapidly increases with higher angles of attack, impeding the airfoil's ability to create a lifting force. There are three types of stall: thin-airfoil, leading-edge, and trailing edge [10]. Each type of stall has a distinctive relationship between the lift coefficient and the angle of attack.

Thin-airfoil and leading-edge stalls are usually more abrupt and are characterized by a sudden loss of lift. The trailing-edge stall, however, is more gradual and less dependent on the airfoil configuration. In low to moderate Mach numbers, most traditional subsonic wings lie in the trailing-edge stall. Thin-airfoil stall typically occurs in airfoils with low thickness-to-chord ratios. This type of stall is characterized by flow separation that occurs near the leading edge and extends rapidly over the entire length of the airfoil surface. The leading-edge stall occurs when the flow separates near the trailing edge and rapidly moves up the surface of the airfoil with a small change in the angle of attack. This occurs when the pressure gradient becomes too strong for the boundary layer to remain attached [10]. This type of stall is more common in airfoils with a smaller leading edge radius. Figure 2.1 compares different airfoil types for their effect of thickness and camber on the maximum lift coefficient. In this figure, a relation between the airfoil's thickness-to-chord ratio and the stall type can be seen. Airfoils with thicknesses between 10% and 15% tend to show leading-edge stall, this is the least desirable type of stall. In the trailing-edge stall, flow separation starts at smaller angles of attack from the trailing edge due to the adverse pressure gradient of the airfoil, while the rest of the flow remains attached to the airfoil. As the angle of attack increases, the separated region increases in size caused by the reversed flow. This type of stall is more gradual compared to leading-edge and thin-airfoil stalls [10].

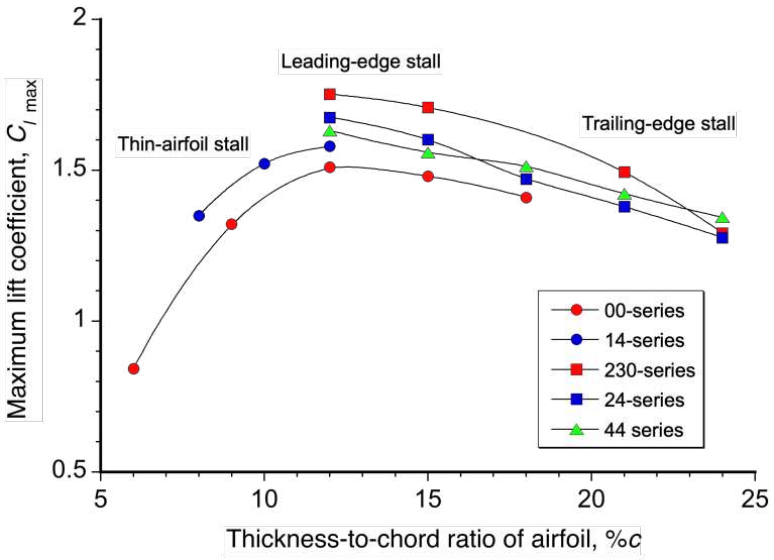

Figure 2.1: Effect of thickness and camber on the C_{lmax} of an airfoil [27]

2.2 Aeroacoustics and Noise Generation Mechanisms

Aeroacoustics is a field related to the interaction between the flow and the acoustic field. It is a branch of acoustics that studies the sounds generated by aerodynamic forces acting with bodies or turbulent flows, also referred to as aerodynamic noise. Aeroacoustics examines both the sound generation at the source and its propagation through the medium.

Aerodynamic noise is primarily generated by the interaction of objects with the flow and the inherent instabilities within the flow itself. Research regarding this topic has been ongoing for over a decade to better understand and predict different self-noise mechanisms. There are five different self-noise mechanisms associated with airfoils: turbulent boundary-layer trailing edge noise, separated boundary-layer stall noise, laminar boundary layer vortex shedding noise, blunt trailing edge vortex shedding noise, and turbulent inflow noise [5, 32].

Turbulent Boundary-layer Trailing Edge Noise

Trailing edge noise is one of the significant sources of aerodynamic noise associated with airfoils and other aerodynamic bodies operating in a fluid. A turbulent boundary layer can be characterized by chaotic pressure fluctuations on the surface. This occurs due to the interaction between turbulent flow at a high chord-based Reynolds number (R_c) and the surface of an airfoil. When the turbulent boundary layer experiences a sudden change in the boundary conditions, such as interacting with the trailing edge, strong turbulent kinetic energy is converted into acoustic energy and disperses into the far-field. This type of aerodynamic noise is known as turbulent boundary-layer trailing edge (TBL-TE) noise [26]. Figure 2.2 visualizes the TBL-TE noise mechanism.

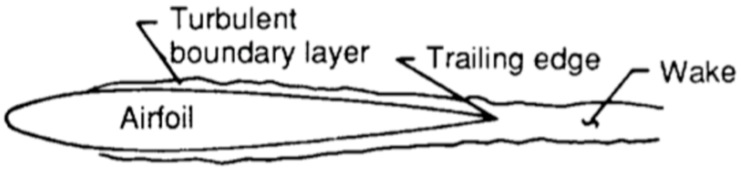

Figure 2.2: Turbulent Boundary-layer Trailing Edge Noise [41]

Separation Stall Noise

Airfoil self-noise generated by flow separation is not well understood in terms of the underlying mechanisms. This noise is generated by the detachment of a boundary layer from the surface of the airfoil, forming a wake. Separation occurs when the fluid flowing around an airfoil on the suction side experiences an adverse pressure gradient. When the pressure gradient exceeds the fluid's inertial forces, the flow starts to separate from the airfoil surface [60]. Figure 2.3 illustrates the separation phenomenon. In the top airfoil, separation can be observed in the early stages, while in the bottom airfoil, the separation extends along the entire airfoil length.

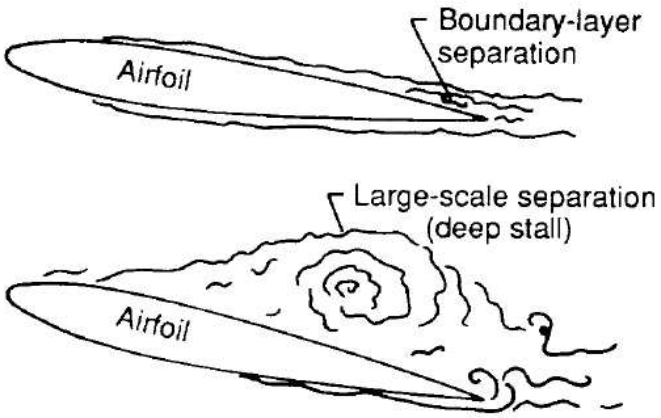

Figure 2.3: Separation stall noise for light and deep stall [50]

In the process, there are two different flow regimes, the separating boundary layer and the undisturbed free-stream, which are separated by a shear layer. This shear layer is inclined to be unstable and form vortices [66]. There are three noise-generation mechanisms possible: Coherent turbulent structures in the shear layer, shear layer instabilities, and shear layer flapping [25].

Coherent structures in the first mechanism, Figure 2.4a, are vortices forming in the spanwise direction due to the detached shear layer. These vortices break down and orient towards the streamwise direction downstream [49]. When these turbulent structures pass over the trailing edge, an unsteady hydrodynamic pressure will develop over the surface of the airfoil. This pressure is then scattered at the trailing edge to the far-field [66]. Instabilities in the separated

shear layer, such as Kelvin-Helmholtz (KH) instabilities, can occur as shown in Figure 2.4b. KH instabilities are wave-like disturbances that can grow and roll up into vortices. They occur when there is a velocity difference (shear) across the interface of two different layers[11, 14]. These waves yield pressure oscillations on the surface of the airfoil and emit noise. Shear layer flapping is the third noise mechanism caused by flow separation on the airfoil. In the early stages of separation, the shear layer can show an oscillatory motion, as shown in Figure 2.4c. The flapping typically occurs at characteristic frequencies that depend on flow conditions, this is found to occur mainly at low frequencies [67]. The non-dimensional frequency of the flapping motion exists within the Strouhal number range, $St_{Lr} \in [0.08, 0.20]$. This Strouhal number is defined as $St_{Lr} = fL_r/U_\infty$ where L_r is the mean reattachment length, U_∞ the free-stream velocity, and f is the frequency [14]. This flapping phenomenon is correlated with the separation and reattachment condition of the flow.

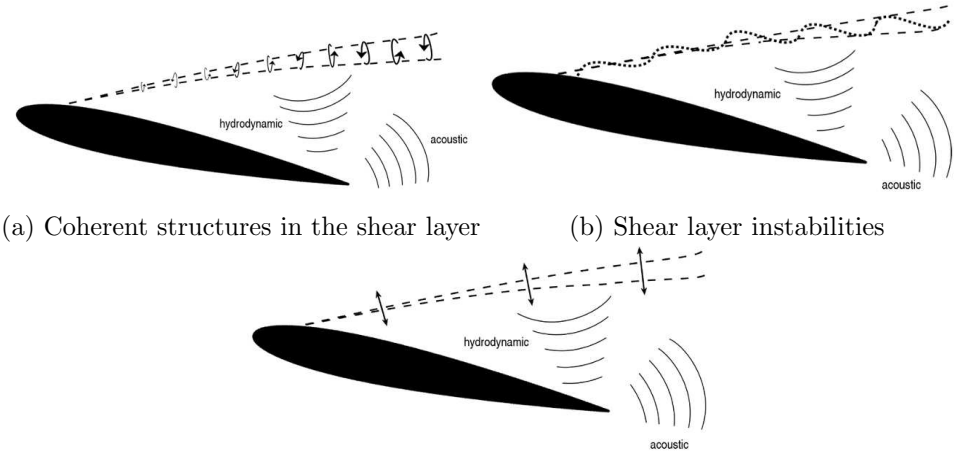

(a) Coherent structures in the shear layer

(b) Shear layer instabilities

(c) Shear layer flapping

Figure 2.4: Separation noise mechanisms [25].

Laminar Boundary Layer Vortex Shedding Noise (LBL-VS)

As implied by the name of this self-noise mechanism, it occurs when a laminar boundary layer is present on the surface of the airfoil when interacting with flows with low to moderate Reynolds numbers. At the trailing edge, vortex shedding emits pressure waves that propagate upstream, which creates and strengthens instability waves called Tollmien-Schlichting waves [5]. These waves are streamwise unstable waves that have a significant effect on beginning the boundary layer transition from a laminar to a turbulent regime [33]. The noise is generated from feedback loops that connect the trailing edge and the instability waves upstream, as shown in Figure 2.5. When the instability waves reach the trailing edge, vortices with similar frequencies are formed [28]. Loud, tonal, whistling sounds characterize LBL-VS noise.

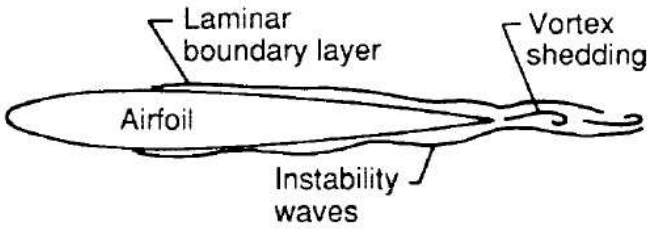

Figure 2.5: Laminar Boundary Layer Vortex Shedding Noise [50]

Trailing Edge Bluntness Vortex Shedding Noise

Trailing edge bluntness vortex shedding noise is another significant source of noise. The noise emitted is due to the vortex shedding created by blunt trailing edges. In the area behind a blunt trailing edge, there is a large-scale vortex-shedding phenomenon, which leads to the formation of the Kármán vortex street in the wake. The noise from the vortex shedding is typically linked to the fluctuations in wall pressure at the surface near the trailing edge, as shown in Figure 2.6. The noise is caused by the unsteady circulations associated with the shedding vortices in the wake [64]. The geometry of the trailing edge determines the frequency and amplitude of this noise mechanism [5].

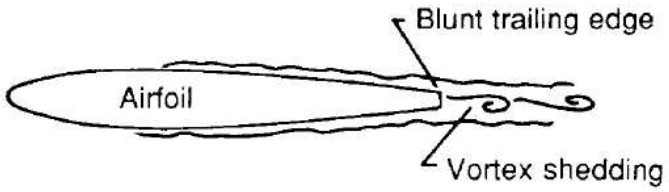

Figure 2.6: Trailing Edge Bluntness Vortex Shedding Noise [50]

Turbulent Inflow Noise

Turbulent inflow noise is generated when turbulent eddies in the inflow interact with the leading edge of an airfoil. The turbulent structures that are carried by the airfoil strike the leading edge, causing pressure fluctuations that propagate as sound waves. This interaction converts a portion of the turbulent kinetic energy into acoustic energy. Additionally, factors such as the geometry of the leading edge, turbulence intensity, and the Mach number of the flow influence the intensity of the generated noise. The turbulent inflow noise mechanism is shown in Figure 2.7, it is significant in various applications ranging from aircraft wings and turbine blades to fan blades [17, 51].

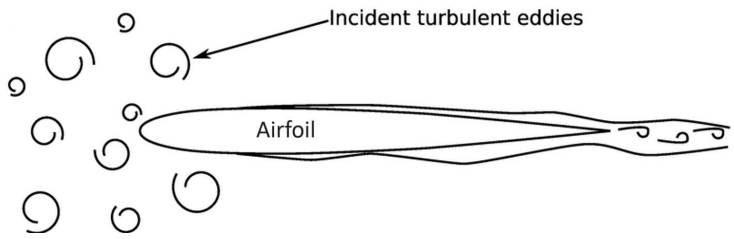

Figure 2.7: Trailing Edge Bluntness Vortex Shedding Noise [29]

2.3 Noise Propagation in Far-Field

Noise is a sequence of pressure waves that travel through a compressible medium. During the propagation of these sound waves, they can be altered by the medium. These changes occur in the waves' reflection, refraction, or attenuation. This introduces the vital challenge of accurately predicting the sound levels at a specific location in the near or far-fields [47]. As suggested by the name, the near field is the region closely surrounding the noise source. In this region, the sound waves have complex behavior where there aren't any set relations between the distance and pressure. The far-field in acoustics starts at approximately one wavelength away from the sound source and extends infinitely outward, this can be seen in Figure 2.8. The beginning of the far-field is dependent on frequency, as the wavelength is also frequency-dependent. This region's sound pressure level is characterized by the sound pressure and acoustic particle velocity being in phase [22, 54]. To ensure that measurements are taken in the far-field, acoustic standards are typically taken at least one meter away from the sound source.

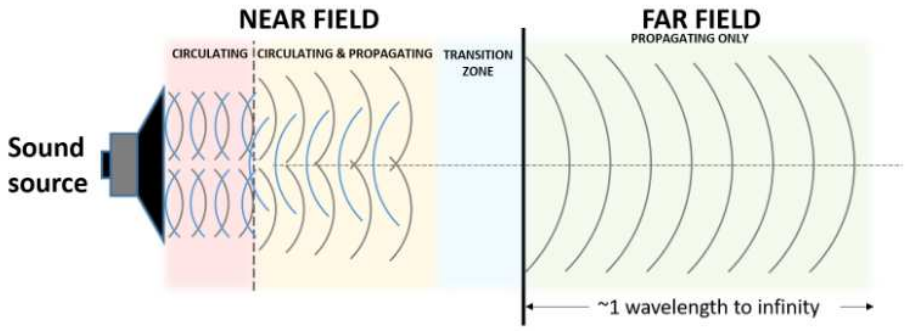

Figure 2.8: Near and far-field wave behavior [54]

Sound propagation is influenced by several aspects, including geometric spreading, surface effects, and atmospheric effects. Geometric spreading refers to how sound energy spreads. The two types of geometric spreading are spherical and cylindrical spreading. Spherical spreading portrays the spreading of noise from a point source equally in all directions, and cylindrical spreading depicts the spreading of noise from a line source, as shown in Figure 2.9. Generally, the losses from the spreading are expressed in 6 dB with each doubling of distance from the

source for spherical spreading and 3 dB for cylindrical spreading. In the far-field, the sound waves can be approximated as spherical waves radiating from a point source [58].

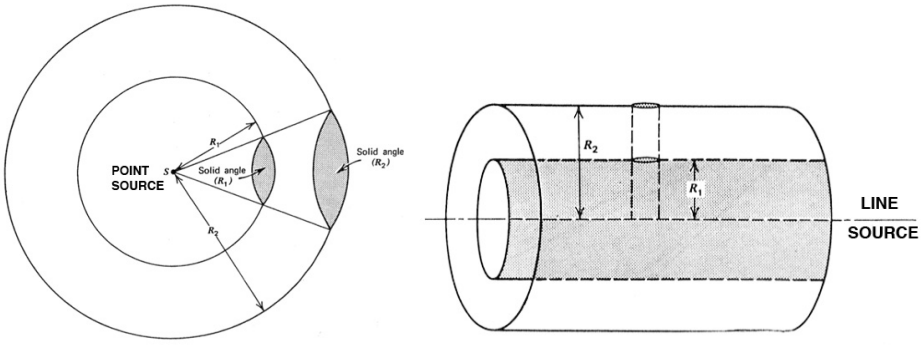

(a) Spherical spreading (b) Cylindrical spreading

Figure 2.9: Geometric spreading [58].

In sound propagation, the surface has significant effects on the sound pressure level as well. If the sound is propagating over the ground, there will be acoustic energy losses depending on the smoothness of the ground it is being reflected on. For instance, surfaces with grass will result in lower sound levels where high frequencies are attenuated. Another effect present from the ground effect is the interference of the reflected wave when the source and receiver are close to the ground. The reflected wave will destructively interfere with the direct wave. Other barriers and trees present within the vicinity of the sound source could also lead to interference with the direct waves [3]. Atmospheric effects are important in sound propagation. Several atmospheric conditions can largely impact the propagation of sound, this includes the wind speed and direction, temperature, and humidity. The acoustic energy can be absorbed by the atmosphere, depending on the temperature and levels of humidity. Generally, higher frequencies are absorbed more than lower frequencies [20]. The wind and temperature gradients in the atmosphere also have a significant effect on the sound propagation. The temperature of the gas is directly related to the speed at which the sound propagates. As the speed of sound waves will differ with temperature variations, the sound waves can bend upwards or downwards. Similarly, wind gradients can cause similar effects of sound wave bending caused by a stationary layer of air next to the ground. Such changes in temperatures and wind result in different measured sound levels from what is expected from geometrical spreading and atmospheric absorption, this can be as much as 20 dB [58].

2.4 Analytical Noise Prediction Methods

As aeroacoustic arises from the interaction of airflow with solid surfaces, aeroacoustic analogies are developed to predict and analyze this type of noise. These analogies bridge the gap between fluid dynamics and acoustics, they transform complex aerodynamic phenomena into manageable

acoustic problems. Aeroacoustic analogies are generally derived from the compressible Navier-Stokes equations. There are several acoustic analogies for different applications, in this section, the Lighthill's and Ffowcs Williams and Hawkings acoustic analogies will be explained in detail.

2.4.1 Lighthill's Acoustic Analogy

Lighthill's acoustic analogy is an essential theoretical framework for predicting aerodynamic noise. It provides the appropriate equations to connect the acoustic wave behavior outside the turbulent region with the significant velocity fluctuations occurring within the flow. This is valid as there were no assumptions made about the compressibility effects in the turbulent region. If incompressibility was assumed, no sound would be generated as acoustic effects would not exist. The Lighthill's equation is derived by taking the Navier-Stokes equations. Taking the time derivative of the continuity equation

$$\frac{\partial}{\partial t}\left(\frac{\partial \rho}{\partial t}+\frac{\partial(\rho v_i)}{\partial x_i}\right)=0 \tag{2.1}$$

and the divergence of the momentum equation

$$\frac{\partial}{\partial x_i}\left(\frac{\partial(\rho v_i)}{\partial t}+\frac{\partial(\rho v_i v_j+p_{ij})}{\partial x_j}\right)=0 \tag{2.2}$$

subtracting equation 2.2 from 2.1 gives

$$\frac{\partial^2 \rho}{\partial t^2}=\frac{\partial^2(\rho v_i v_j+p_{ij})}{\partial x_i \partial x_j} \tag{2.3}$$

where the pressure term, p_{ij}, can be written as $p_{ij}=(p-p_\infty)\delta_{ij}-\sigma_{ij}$ as the stress tensor's diagonal elements are defined as the gauge pressure, which is relative to the surrounding ambient pressure. The term $\partial\rho/\partial t$ is equal to $\partial\rho'/\partial t$ as the density perturbations relative to the surroundings are expressed as $\rho'=\rho-\rho_\infty$. Subtracting $\partial(\rho' c_\infty^2)/\partial x_i^2$ from each side of equation 2.3, where c_∞ is the ambient speed of sound, results in the Lighthill's wave equation [30].

$$\frac{\partial^2 \rho'}{\partial t^2}-c_\infty^2\frac{\partial^2 \rho'}{\partial x_i^2}=\frac{\partial^2 T_{ij}}{\partial x_i \partial x_j} \tag{2.4}$$

where

$$T_{ij}=\rho v_i v_j+(p-p_\infty)-(\rho-\rho_\infty)c_\infty^2\delta_{ij}-\sigma_{ij} \tag{2.5}$$

In this equation, the left side refers to the propagation in a uniform medium with a speed of sound c_∞ of an acoustic wave, where T_{ij} is the stress tensor given in equation 2.5. The right side of the equation relates to the effects that lead to the generation of acoustic waves, generally referred to as the source term. Including the stationary medium's speed of sound is appropriate,

as the intention is to assess the acoustic waves that propagate in the stationary medium in the far-field away from the turbulent region. The source term in the equation represents how will the turbulent region relate to the acoustic waves in the far-field [18].

Lighthill's equation has been used in multiple applications, however, there are limitations to this acoustic analogy. The term T_{ij} often cannot be resolved, thus several assumptions have to be made. This can lead to incorrect results depending on the case. For instance, an assumption of a homentropic flow, where the flow is uniform and has constant entropy, is valid in hydroacoustic applications but could be complicated for aeroacoustic applications, as a flow can be isentropic but not homentropic [18].

2.4.2 Ffowcs Williams and Hawkings Acoustic Analogy

Lighthill's acoustic analogy represented the wave equation in a medium where the object was stationary. The FW-H equation extends to Lighthill's equation to include surfaces in arbitrary motion. This is used in multiple aerodynamic applications where surfaces are moving, such as airfoils, rotor blades, and other structures immersed in a flow. The FW-H equation [62] is expressed as

$$\begin{aligned}\frac{\partial^2(\rho' H_s)}{\partial t^2} - c_\infty^2 \frac{\partial^2(\rho' H_s)}{\partial x_i^2} =& \frac{\partial^2(T_{ij} H_s)}{\partial x_i \partial x_j} - \frac{\partial}{\partial x_i}((\rho v_i(v_j - V_j) + p_{ij}) n_j \delta(f) |\nabla f|) \\ &+ \frac{\partial}{\partial t}((\rho v_j - \rho' V_j) n_j \delta(f) |\nabla f|)\end{aligned} \tag{2.6}$$

which is a wave equation including the effects of surfaces in motion. This equation was derived by examining the continuity and momentum equations in terms of $\mathbf{v}H_s$, ρH_s, and pH_s, which are defined throughout an infinite, unbounded volume V_∞. $H_s(f)$ is a Heaviside step function which is zero for $f < 0$, and one $f > 0$. $\delta(f)$ is the Dirac delta function, which has the same properties as the Heaviside step function. The function f is defined such that it is greater than zero outside a volume bounded by a surface S_o, less than zero inside the volume, and exactly zero on the surface itself, this is illustrated in Figure 2.10. The integral form of FW-H equation [18] is represented as

$$\begin{aligned}\rho'(\mathbf{x}, t) c_\infty^2 H_s =& \frac{\partial^2}{\partial x_i \partial x_j} \int_{V_o} \left[\frac{T_{ij}}{4\pi r |1 - M_r|} \right]_{\tau = \tau^*} dV(\mathbf{z}) \\ &- \frac{\partial}{\partial x_i} \int_{S_o} \left[\frac{(\rho v_i(v_j - V_j) + p_{ij}) n_j}{4\pi r |1 - M_r|} \right]_{\tau = \tau^*} dS \\ &+ \frac{\partial}{\partial t} \int_{S_o} \left[\frac{(\rho v_j - \rho' V_j) n_j}{4\pi r |1 - M_r|} \right]_{\tau = \tau^*} dS\end{aligned} \tag{2.7}$$

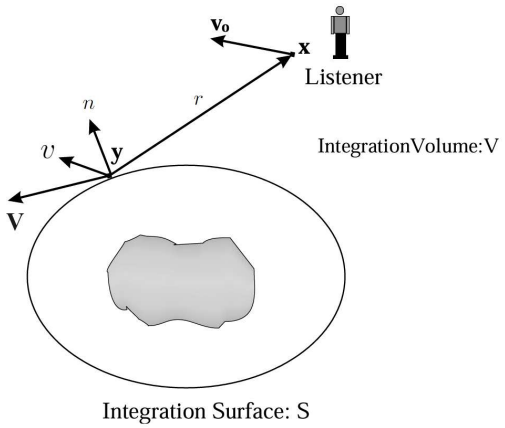

Figure 2.10: FW-H acoustic analogy scheme [6]

In equation 2.7 and 2.6, the variables t refers to the observer times, τ is the emission time, τ^* is the corrected retarded time given by $\tau^* = t - r(\tau^*)/c_\infty$, r is the distance from the data surface to the observer defined as $r = |\mathbf{x} - \mathbf{y}|$, M_r is defined as $M_i \hat{r}_i$ which is the Mach number of the source in observer direction, v_j is component of the fluid velocity at the surface, V_j is the component of the surface velocity, and n_j is the component of the unit surface normal. The first term in equation 2.7 is the quadrupole term which is influenced by the stress tensor T_{ij} and is the sound produced by distortions and turbulence in the flow, such as shockwaves. The second term is the dipole source term, which is related to the surface loading. The third term is the monopole source term, associated with volume displacement. The term $|1 - M_r|$ adjusts for the compression or expansion of the observer's timescale relative to the source's timescale, depending on whether the source is moving away from or towards the observer, respectively. This phenomenon is known as the Doppler effect [6].

The purpose of the FW-H surface is to provide a far-field solution to the wave equation, given accurate numerical calculations, on a surface that bounds the source region. It is preferable to choose the surface so that the Lighthill stress tensor does not contribute to the far-field in the region outside the FW-H surface to ensure confidence in the calculations. The FW-H equation becomes

$$\begin{aligned}\rho'(\mathbf{x},t)c_\infty^2 H_s \approx & \frac{1}{c_\infty}\int_{S_o}\left[\frac{x_i}{4\pi|\mathbf{x}|^2(1-M_r)^2}\left\{\frac{\partial L_i}{\partial\tau}+\frac{L_i}{(1-M_r)}\frac{\partial M_r}{\partial\tau}\right\}\right]_{\tau=\tau^*} dS \\ & + \int_{S_o}\left[\frac{1}{4\pi|\mathbf{x}|(1-M_r)^2}\left\{\frac{\partial Q_n}{\partial\tau}+\frac{Q_n}{(1-M_r)}\frac{\partial M_r}{\partial\tau}\right\}\right]_{\tau=\tau^*} dS\end{aligned} \tag{2.8}$$

where

$$L_i = (\rho v_i(v_j - V_j) + p_{ij})n_j \qquad Q_n = (\rho v_j - \rho' V_j)n_j \tag{2.9}$$

which is introduced by Farassat [4, 15]. In linear acoustics, where nonlinear interactions are negligible and viscous effects are disregarded, the term $\rho v_i v_j$ is considered to be zero.

Additionally, the variable ρ', defined as $\rho - \rho_\infty$, is substituted with $(p - p_\infty)/c_\infty^2$ [6].

2.5 Computational Noise Prediction Methods

Computational Aeroacoustics (CAA) is a specialized field that focuses on the numerical simulations of aeroacoustics field mentioned in an earlier section. It focuses on predicting noise generated by unsteady turbulent flows associated with aerodynamic structures. CAA employs various numerical methods to solve the complex equations governing aeroacoustic phenomena. These methods are generally divided into direct and hybrid methods.

2.5.1 Direct Method

The direct method refers to the process where the noise fields are computed at the same time with the flow field. This can be done by using the Direct Numerical Simulation (DNS), or Large Eddy Simulation (LES). The DNS method involves the direct solution of the Navier-Stokes equations, fully capturing all turbulence scales and their interactions without relying on modeling approximations. DNS provides a highly detailed and accurate representation of the flow field and the resulting noise generation mechanisms. It is considered the most accurate technique for noise prediction due to its ability to resolve all relevant motion and sound generation [55]. Due to its accuracy and detail, DNS is an ideal method for fundamental research into noise generation mechanisms, allowing researchers to capture intricate details of turbulent flows and their acoustic emissions. However, the computational cost is this method's primary challenge. To be able to produce such accurate results, extremely fine meshes and small time steps are required to resolve all the scales of the turbulent flow, which results in a high demand for computational resources. Additionally, the vast amount of data generated by DNS introduces another challenge where the data needs to be stored, managed, and analyzed. In a direct method, DNS is used if the flow is turbulent and the simulation aims to capture the dynamics of all physical scales. In contrast, LES only aims at capturing the larger, energy-containing eddies. It resolves large-scale turbulent structures directly while modeling smaller scales, offering a balance between accuracy and computational cost when compared to DNS. Nevertheless, it is still considered to be computationally expensive for the average aerodynamic case. For LES, only the sound field linked to the captured dynamics is available [8].

2.5.2 Hybrid Method

Unlike direct methods, hybrid methods do not aim to directly capture the generated sound field. Instead, hence the name, it combines Computational Fluid Dynamics (CFD) with acoustic analogies or computational models for noise generated by the flow. This allows for a more efficient computation compared to direct methods while still capturing important details of the noise generation process.

In the hybrid CFD-CAA method, CFD extracts the acoustic source terms from the flow field. The acoustic results can be computed using different computational models, such as linearized Euler equations (LEE), on an external grid from the flow field in a different simulation. The acoustic results can also be obtained using different analytical acoustic analogies discussed in Section 2.4 utilizing the CFD output. Acoustic analogies use integral formulas with different source terms to compute noise behavior, such as Lighthill's and the FW-H equations. The acoustic results are captured by observer locations in the far-field. The surface chosen contains all physical processes that contribute to the noise at the observer location [19]. The main benefit of the hybrid methods is their ability to provide such accurate acoustic results at a lower computational cost by focusing the computational resources on resolving the most important flow structures. However, the accuracy of such methods lies in the quality of the CFD simulations and the assumptions made in the acoustic analogy.

2.6 Self-Noise Mechanisms Models

In the study of aerodynamic noise generated by airfoils, understanding the self-noise mechanisms is crucial for accurate prediction and control. In section 2.2, the self-noise mechanisms have been introduced, and their physics were explained. This section delves into two primary approaches for predicting self-noise generated by airfoils: analytical, and computational models.

2.6.1 Analytical Models

Analytical models for self-noise prediction offer semi-empirical formulas derived from experimental data. These models provide quick and practical estimates, which are essential for preliminary assessments and standard configurations. They offer a balance between accuracy and computational efficiency.

One of the most widely used models is the BPM which has been introduced by Brooks, Pope, and Marcolini [5]. This model covers the most dominant self-noise mechanisms on an airfoil, including TBL-TE, separation stall noise, and LBL-VS. This model uses empirical relationships derived from extensive wind tunnel tests. It relates noise levels to parameters such as boundary layer thickness, flow velocity, airfoil geometry, and angle of attack since they significantly affect the turbulence in the boundary layer, especially near the trailing edge. The BPM model has become the standard reference for evaluating more advanced noise prediction methods, including those using LES.

Another widely used analytical model is introduced by Amiet [2]. This model is significantly designed for the trailing edge noise, it simplifies the complex interactions between turbulent boundary layer pressure fluctuations on the airfoil and its trailing edge into manageable calculations. This theory, in most cases, does not function effectively as a practical prediction tool. This is due to the thin-airfoil theory approximation of a flat plate that is used in a uniform

flow. While this approximation can serve as a satisfactory aeroacoustic model for a real airfoil, it is a poor model in accurately representing the detailed aerodynamics of the boundary layer.

A comparison case has been conducted for a NACA0012 airfoil at $\alpha = 0°$ with a chord length of 0.23 m, span length of 1.22 m, observers located at 3 m above the mid-span of the trailing edge, flow speed of 55.5 m/s, and heavily tripped airfoil boundary layer. The results can be seen in Figure 2.11. The data is shown in 1/3 octave band Sound Pressure Level (SPL). Overall, the prediction is very well. For Amiet, the predictions seem to be 5 dB below the experimental values at lower frequencies. Such a discrepancy is expected, as the adverse pressure gradient at the rear of the airfoil would increase the energy of larger boundary-layer eddies when compared to a flat plat boundary layer. BPM shows a larger difference at lower frequencies when compared to the measurement data. The difference might be due to the fact that the measurement data is obtained using a phased microphone array to distinguish the trailing edge noise from one side of the airfoil. In contrast, the BPM model includes only the noise contributions in antiphase across the chord line [18].

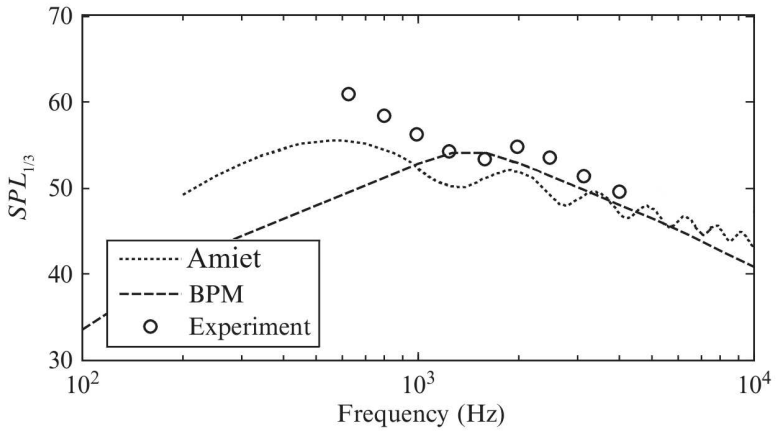

Figure 2.11: Comparison of trailing edge noise spectra between BPM and Amiet models at $\alpha = 0°$ [18]

Brooks, Pope, and Marcolini [5] utilized a series of 2D NACA0012 airfoils with chord lengths ranging from 2.5 cm to 30 cm during their investigation of turbulent boundary-layer trailing edge noise. They placed a pair of far-field microphones in their testing facilities on either side of the airfoil's chord line to isolate the trailing edge noise by exploiting antiphase characteristics relative to facility noise. Additionally, a second pair of microphones was placed at each airfoil's front and rear to remove unwanted leading edge noise caused by the model mounting. The tests were conducted on the airfoils for different angles of attack, with a boundary-layer trip and a clean configuration with a natural transition. From this extensive dataset, they extracted cases where the far-field noise was attributed to turbulent boundary-layer trailing edge noise. In Figures 2.12 and 2.13, the results of the BPM model are shown for the airfoils with chord lengths of 10.16 cm and span lengths of 45.72 cm at two different flow speeds for angles of

attack 6.7° and, 15.6° respectively. The observers are located at the midspan perpendicular to the trailing edge at a distance of $r = 1.22m$. Figure 2.12 shows the contributions of all the self-noise mechanisms and how they contribute to the total noise prediction compared to the measurement. In the second figure, Figure 2.13, a higher angle of attack is chosen where light-stall is considered, the total prediction is quite well compared to the measured data. It can also be noted that the measured data for higher Mach numbers increases the noise by almost 20 dB. As stall noise has a large contribution to the total prediction, it has been explored further in more detailed experiments.

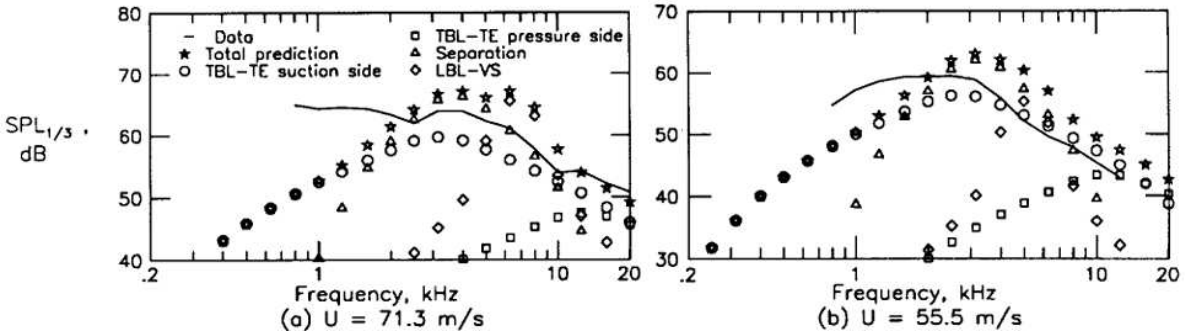

Figure 2.12: BPM model for NACA0012 with $c = 10.16$ cm, $L = 45.72$ cm, and $\alpha = 6.7°$ [5]

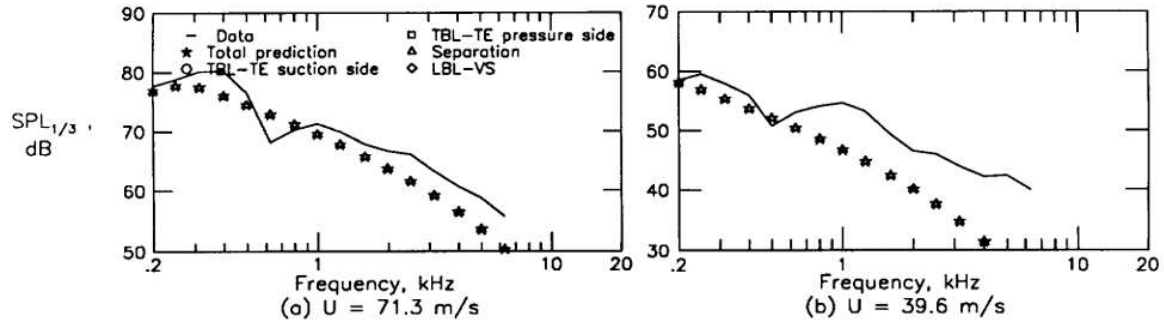

Figure 2.13: BPM model for NACA0012 with $c = 10.16$ cm, $L = 45.72$ cm, and $\alpha = 15.6°$ [5]

2.6.2 Computational Models

Computational models such as LES, DNS, and DDES provide detailed predictions that often match the accuracy of experimental data. These models can capture the complex interactions of unsteady flow features that might be missed by empirical models. However, computational models require significant computational resources. In most cases, analytical models can offer quick and practical estimates, making them give a suitable balance between accuracy and computational efficiency. In this section, computational tools will be examined and compared to measured data and analytical models.

In a study made by Chen et al. [7], the airfoil-noise has been predicted using FW-H using pressure fluctuations acquired from LES and DDES methods. The airfoil used in this study is NACA 65(12)-10 with a chord length of 0.15 m. The observers were located on the mid-span plane perpendicular to the trailing edge in the chord-wise direction 1.2 m away. The results obtained in this study for the incoming flow of 20 m/s are shown in Figure 2.14, showing that the results obtained by LES and DDES are quite well compared to the measured data, with some discrepancies at lower frequencies. The angle of attack in this study was set to be $-3.3°$ which causes a peak in the pressure fluctuations on the pressure side. This case was mainly chosen to observe the similarities and differences between using LES and DDES.

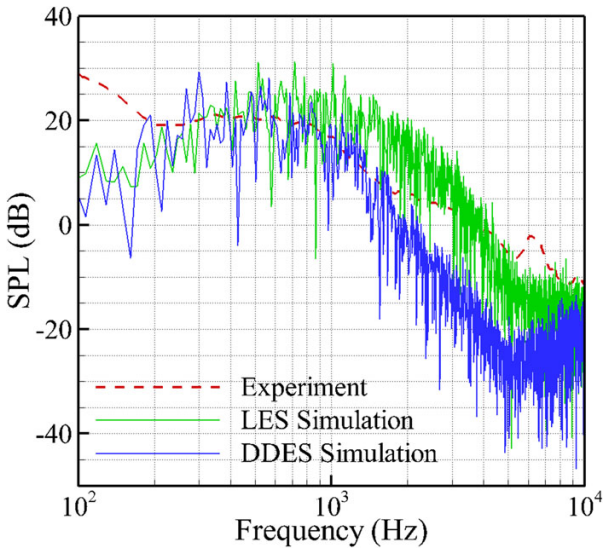

Figure 2.14: Comparison between predicted SPL and experimental data [7]

Chen et al. [7] compared the effects of DDES and LES at two different flow speeds. Figure 2.15 shows the results of LES, DDES, and predicted results from NREL Airfoil Noise (NAFNoise) for the flow speeds of 20 m/s and 50 m/s. NAFNoise is a program developed by National Renewable Energy Laboratory (NREL) [39] that predicts the noise for all types of airfoils, the noise predicted is for all the aforementioned self-noise sources. This program obtains the TBL-TE and LBL-VS using the BPM model. Comparison with NAFNoise is made to validate the results obtained.

In Figure 2.15a, the LES and DDES results are relatively accurate compared to NAFNoise predictions, with DDES SPL results even closer. However, for frequencies greater than 5 kHz, the LES and DDES results are quite different from the NAFNoise results. This can also be seen in Figure 2.15b for frequencies larger than 10 kHz. The inconsistencies for these frequency ranges are due to the limitations within the NAFNoise as its prediction is quite weak for higher frequencies. The SPL results shown in Figure 2.15b differ, in this case, the LES results show better agreement with the NAFNoise prediction. However, the DDES results show a great difference and are extremely inaccurate when compared to LES and NAFNoise in both, the

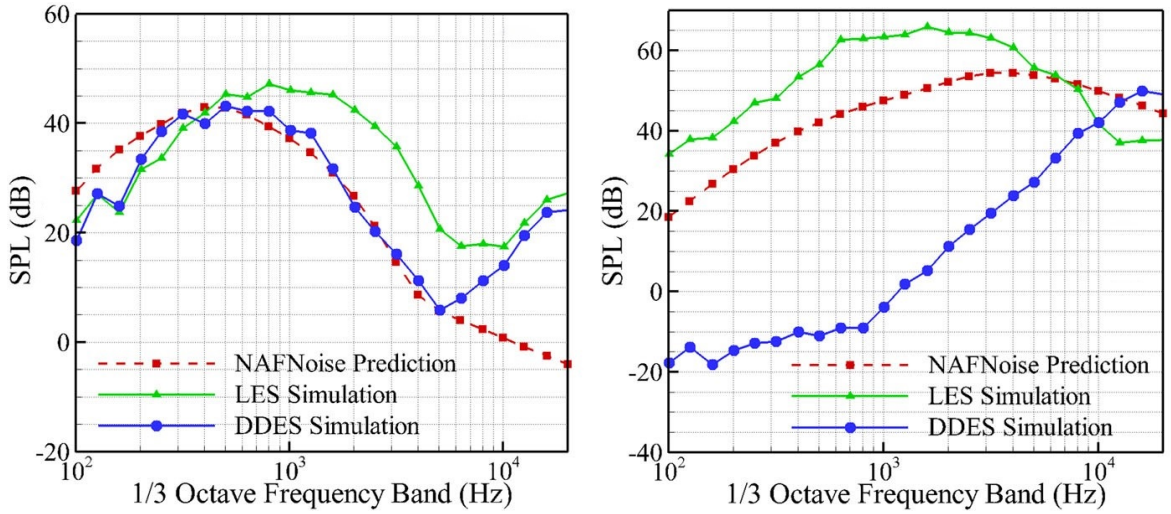

(a) 20 m/s ($Re_c = 2 \times 10^5$) (b) 50 m/s ($Re_c = 5 \times 10^5$)

Figure 2.15: Prediction of SPL at far-field with a direction angle of 90° for two different incoming flow speeds [7].

prediction and the trend of the broadband noise. This implies that the acoustic source captured from the DDES in an unsteady flow is different from LES.

Figure 2.16, shows other results obtained by Wolf [63], for the case of NACA0012, $\alpha = 5°$, and Re = 408000. In these results, the experimental results are compared to LES and BPM models to show the accuracy of the computational and analytical models. The results of the LES and BPM are in great agreement with the experimental data for this case.

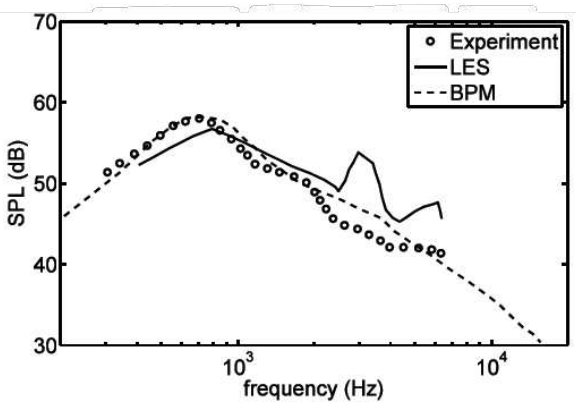

Figure 2.16: Comparison between BPM, LES, and experimental data for NACA0012, $\alpha = 5°$, Re = 408000 [63]

2.7 Turbulence Models

Turbulence is a complex and chaotic state of fluid motion characterized by irregular changes in pressure and flow velocity. Unlike laminar flow, where fluid particles move in smooth layers, turbulent flow involves eddies, vortices, and rapid variations in the flow field. The transition from laminar to turbulent flow typically occurs at high Reynolds numbers, where inertial forces dominate over viscous forces. The concept of turbulence plays a crucial role in aerodynamics, especially around airfoils at stall. Turbulent flow over an airfoil can increase drag, alter lift characteristics, and be a significant source of aerodynamic noise. The chaotic nature of turbulent eddies generates pressure fluctuations that propagate as sound waves, contributing to noise in various applications. As a consequence, choosing a suitable turbulence model in the CFD can affect the noise prediction, as seen in section 2.6.2.

Reynolds-Averaged Navier-Stokes Models

Reynolds-Averaged Navier-Stokes Models (RANS) models simplify the Navier-Stokes equations by decomposing the flow variables into mean and fluctuating components, $\mathbf{u}(\mathbf{x}, t) = \overline{\mathbf{u}}(\mathbf{x}) + \mathbf{u}'(\mathbf{x}, t)$. This approach averages the effects of turbulence over time, resulting in equations that describe the mean flow behavior without resolving all the turbulent scales. This was made to simplify complex systems by partially removing time variables. The RANS equations are used to compute the steady-state or time-averaged flow fields, making them computationally efficient for practical engineering problems. The RANS equations are expressed as a set of non-linear differential equations. There are other turbulence models based on the RANS model, these are divided into one-equation models and two-equation models.

The most common one-equation model is the Spalart-Allmaras (SA) model. This model solves a single kinematic equation to describe eddy turbulent viscosity. This model was specifically modeled for aerospace applications and turbomachinery, which is effective in predicting boundary layer flows. The SA model is also considered to be the least computationally expensive RANS model.

The most commonly used two-equation models are the standard $k - \varepsilon$, standard $k - \omega$, and Shear Stress Transport (SST) $k - \omega$ model. The computational cost increases with the mentioned order of these models. The $k - \varepsilon$ is a model that solves two transport equations for the turbulence kinetic energy (k), and its dissipation rate (ε). This model is the most used in industrial applications due to its robustness, reasonable accuracy, and its ability to use submodels for compressibility, buoyancy, combustion, etc. However, there are limitations while using the $k - \varepsilon$ model this includes the necessary use of wall functions as the ε equation cannot be calculated at the wall. This model also has poor performance in large pressure gradients, large streamline curvature, and strong separation. The $k - \omega$ model also solves for the turbulence kinetic energy (k) and the specific dissipation rate (ω), it is mainly used for cases with flow

separation and near-wall effects. Unlike $k-\varepsilon$, the $k-\omega$ model can be integrated at the wall without the use of wall functions. $k-\omega$ model shows high accuracy near the wall within the boundary layer, while the $k-\varepsilon$ performs exceptionally well in the free-stream region. To utilize the strengths of both models, the SST $k-\omega$ model was developed. The SST model uses a blending function to transition between the $k-\varepsilon$ in the free-stream to the $k-\omega$ near the wall improving the overall performance. The SST model uses an adjusted formulation for turbulent viscosity designed to include the transport effects of the turbulent shear stress [35].

Large Eddy Simulation

Large Eddy Simulation (LES) model simulates turbulent flow by resolving the large turbulent structures in the flow while modeling the smaller scales using subgrid-scale (SGS) models. LES captures the unsteady behavior of large eddies, which are responsible for most of the turbulent transport of momentum and energy, providing more detailed and accurate predictions than RANS models. LES has been more successful for higher-end applications such as flows around blunt bodies, mixing, and combustion. LES is much more computationally expensive than RANS models.

SGS models are essential for modeling the effects of the smaller eddies that are not resolved by the grid. The most commonly used SGS models in LES are Smagorinsky model, Dynamic Smagorinsky model (DSM), and Wall Adapting Local Eddy-viscosity (WALE) model. The Smagorinsky model is among the earliest and most widely used SGS models. The model assumes that the subgrid-scale stresses are proportional to the local strain rate tensor. The Smagorinsky model is expressed as

$$\nu_t = C_d \Delta^2 |\tilde{S_{ij}}| \tag{2.10}$$

where the ν_t is the sub-grid scale viscosity, $\tilde{S_{ij}}$ is the resolved strain rate tensor, Δ is the mesh size, and C_d is the Smagorinsky constant which is typically between 0.1 and 0.2. This constant doesn't have a guideline to determine its value, a calculation method was proposed to adjust the Smagorinsky constant automatically. This adjusted model is the DSM. The calculated flow fields are divided into larger and smaller scales, the Smagorinsky constant is calculated by assuming the interaction between those two scales is similar to the interactions between the grid scale and subgrid scale. The WALE SGS model is designed to improve the prediction of near-wall turbulence by adapting the eddy viscosity based on the local velocity gradients. This model accounts for both the strain rate and rotation rate of the fluid. It is, however, more complex and computationally intensive than the Smagorinsky model [65].

Detached Eddy Simulation

The Detached Eddy Simulation (DES) turbulence model combines elements from RANS and LES models to capture different regions of the flow that was proposed by Spalart [56]. For

regions close to the solid boundaries, where the grid resolution is typically insufficient to resolve all turbulent scales, DES uses RANS. Further away from the boundaries, it switches to LES to capture the larger turbulent structures. Using this method, the cost of LES has been reduced significantly. This is a more popular approach in industrial applications, as it improves the limitations of RANS and provides greater insight into the solution. There are also different varieties of DES, this includes Delayed DES (DDES), and Improved DDES (IDDES). DDES is an improvement over the original DES, DDES delays the switch from RANS to LES to prevent premature transition in attached boundary layers caused by the grid design. IDDES is a further enhancement to the DDES model, it incorporates sophisticated transition criteria and better handling of boundary layer separation. Even though DES is considered to be a great balance between accuracy and computational cost, it still may struggle with accurately predicting near-wall turbulence and transition phenomena. Due to its balance, DES is considered to be suitable for various applications like airfoil noise prediction, where capturing large-scale turbulence is crucial.

Well-Modeled Large Eddy Simulation

Well-Modeled Large Eddy Simulation (WMLES) is an advanced turbulence model designed to combine the benefits of LES with better computational efficiency by using wall models to approximate the effects of near-wall turbulence. This is particularly useful in cases of higher Reynolds number flows, where LES would require an excess amount of grid points near the wall to resolve the entire boundary layer. WMLES resolves large eddies in the outer flow by using LES and approximates the influence of the small-scale eddies close to solid boundaries using wall models. These models apply empirical or simplified turbulence equations to predict the boundary layer behavior without the need for high-resolution grids. This model also offers a good balance between computational cost and accuracy for complex flows.

2.8 Case Studies and Recent Advances

2.8.1 Experimental Data

Moreau et al. [38] have made a few experiments examining the effects of the noise generated by stall at different angles of attack to produce an analytical model based on Curle's analogy. The experiments they made were on a NACA0012 airfoil with a chord of 8 cm, and a span of 13 cm. Using a horizontal nozzle, two regimes have been recorded. The first regime is characterized by broadband noise occurring between angles of attack of 5° and 15°, and the second regime is characterized by a narrowband low-frequency peak for angles of attack higher than 26°. The results can be seen in Figure 2.17, showing the effects of the angles of attack on the sound levels.

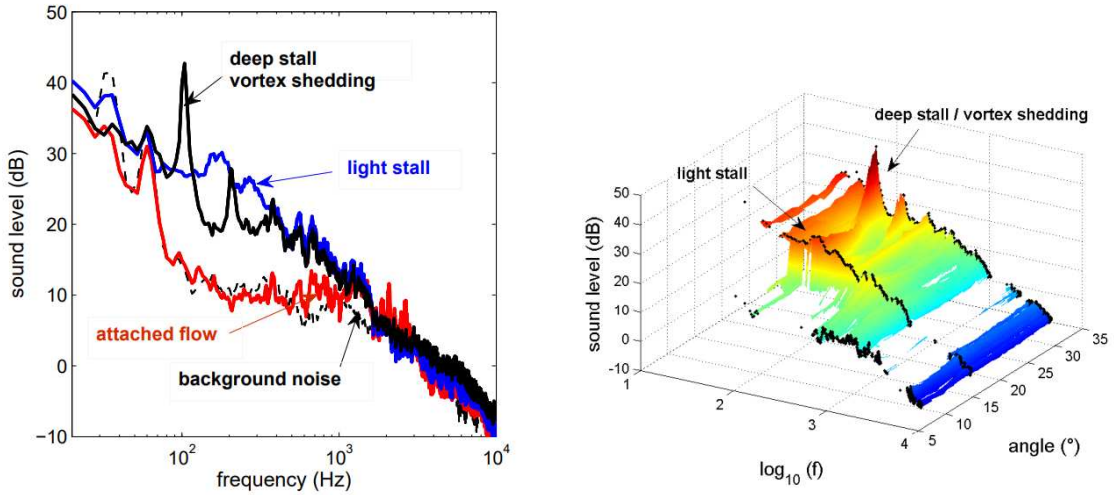

(a) (b)

Figure 2.17: Far-field noise spectra for NACA0012 with $c = 8$ cm, and $L = 13$ cm at deep stall $\alpha = 26°$, light-stall $\alpha = 15°$, and attached flow $\alpha = 5°$. (b) Shows the development between those angles of attack [38].

Figure 2.18, shows the final results of Moreau's analytical model in predicting stall noise. The observers are located in the mid-span plane at $\theta = 90°$. The black lines show the measured noise spectrum at the far-field for that case, the blue line is the measured noise spectrum on the airfoil shifted to the far-field results for comparison, and the red line is the predicted noise from the analytical model. The results are beneficial and reliable compared to the measured data.

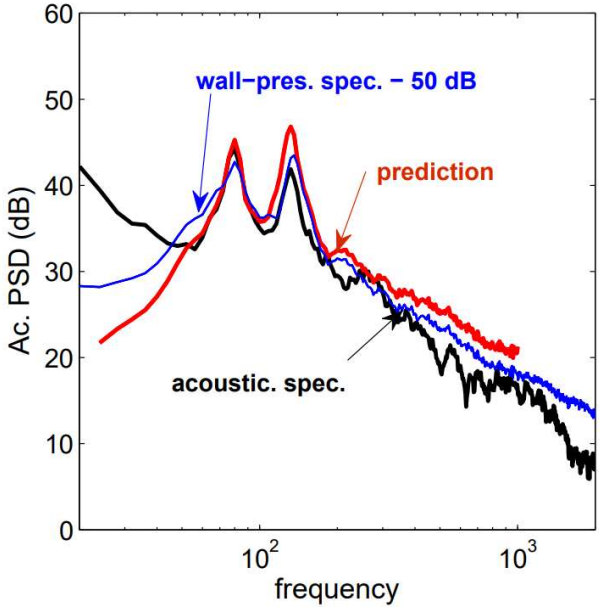

Figure 2.18: Stall-noise prediction for NACA0012 at $\alpha = 18°$, with a flow speed of 22 m/s [38]

Another significant study related to the topic of this study was written by Mayer [34] for his PhD thesis. In this study, Mayer [34] discusses the aeroacoustic characteristics of static and dynamic stall. The work of this study analyzes the NACA 0012 airfoil for different angles of attack. The experimental setup included a Kevlar-walled test section with a servo motor to be able to control the angle of attack of the airfoil in a wind tunnel. The airfoil had a chord length of 300 mm and a span of 500 mm. The free-stream velocity set in this study is 20 m/s. The far-field noise measurements were obtained by using a microphone arc mounted on the ceiling and a large beamforming array 1 m above the test section. All measurements were obtained at $Re_c = 4.2 \times 10^5$ and $M = 5.8 \times 10^{-2}$.

Some results discussed in Mayer [34] are the pressure coefficient for various angles of attack, far-field spectra, and boundary layer measurements. In Figure 2.19, the pressure coefficients obtained show a movement of the suction peak towards the leading edge. This can be seen in the graph at an angle of attack of 13.5° with a peak of $|C_p| = 6.3$. These results show that the suction side near the leading edge has an unfavorable increase in pressure gradient on the boundary layer when approaching stall. On the other hand, the pressure gradient at the pressure side is suitable for all angles.

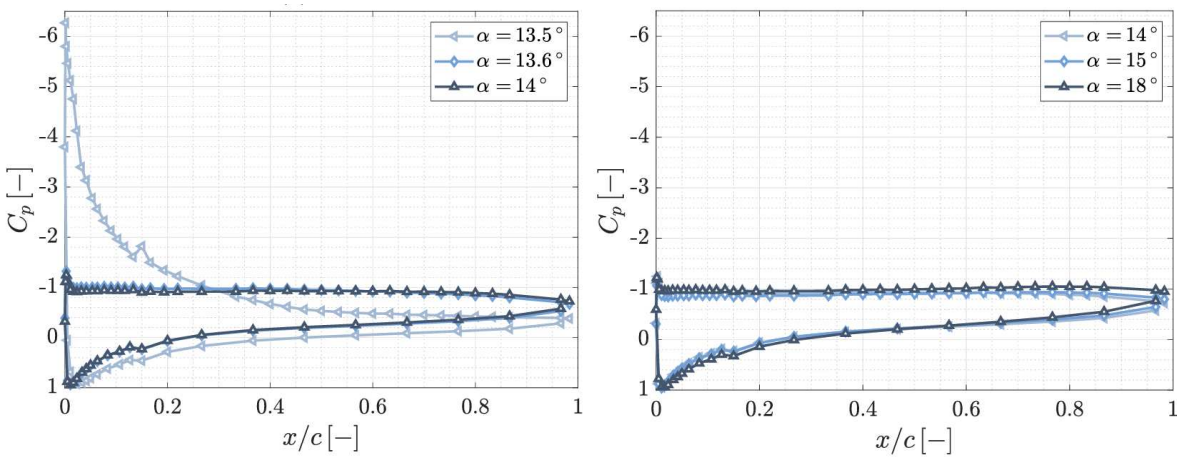

(a) $\alpha = 13.5°$ to 14° (b) $\alpha = 14°$ to 18°

Figure 2.19: Static pressure coefficient [34].

Figure 2.20 shows the far-field noise spectra obtained from Mayer [34] experiments for α from 0° to 18°. This data was obtained by using the microphone array directly above the trailing edge at a distance of 1.75 m and has been corrected for the losses introduced by the Kevlar wall. Mayer [34] has noted that as the angle of attack increases, the peak noise level compared to the background noise tends to occur at lower frequencies, which agrees with the changes observed at the surface pressure spectra at the trailing edge. It has also been observed that when the flow separates, peak noise levels further increase and the peak noise levels shift to the cut-off frequency of the anechoic chamber. The variations observed for α at 13.6°, 15°,

and 18° are quite small, which matches the variations observed in the pressure spectra at the surface.

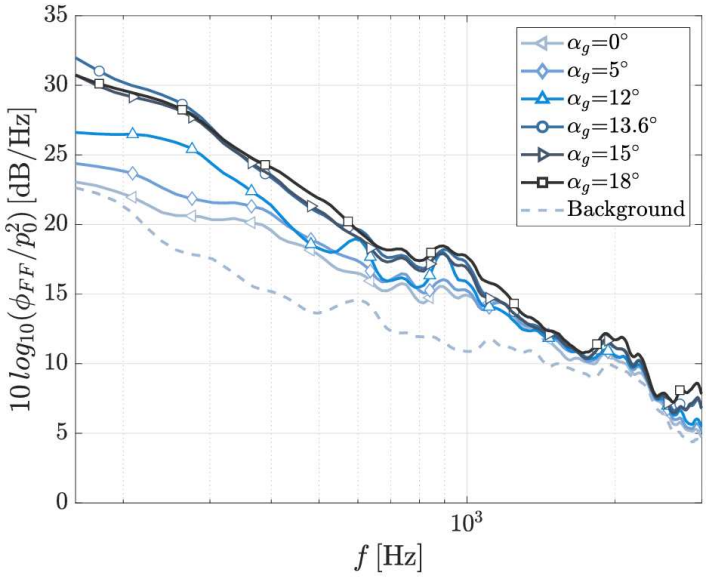

Figure 2.20: Far-field noise spectra [34].

Figure 2.21 shows the boundary layer profiles at $x/c = 0.93$ and 0.98 for the mean velocity (U/Ue), and the turbulence intensity (U'_{rms}/U_∞) in post-stall. Mayer [34] notes that reverse flow measurement using a hot-wire is not attainable, as a result, the mean velocity profiles obtained are distorted. This can be observed in the case of $\alpha = 18°$ at $x/c = 0.98$ where the flow is not attached, the mean velocity profile does not follow the conventional profile. Figure 2.22 shows the boundary layer thickness development over the surface. A linear increase can be observed due to the growing free-shear flow that initiates from the leading edge.

Raus et al. [45, 46] has conducted two experimental studies for a NACA0012 airfoil as well. The studies were conducted around the same experimental setup where they revolved around the noise generated by an airfoil above stall for an airfoil with a chord length of 120mm, and a span length of 300 mm. The noise data was obtained using a microphone located 2 meters away, mid-span, center-chord to the airfoil pressure side, and perpendicular to the incoming flow. In the first study, the free-stream velocity was set to 50 m/s which corresponds to $Re_c = 4.1 \times 10^5$. Figure 2.23, shows the pressure PSD on the surface at $x/c = 0.92$, and the far-field PSD for different angles of attack. For the angle of attack of 15°, the amplitude increases by about 15 dB rapidly at low frequencies compared to lower angles of attack at pre-stall. This noise resembles the light-stall regime. For high angles of attack ($\alpha > 27°$), the airfoil shows blunt body behavior. In the second study, the free-stream velocity was set to 25 m/s which corresponds to $Re_c = 2.1 \times 10^5$. Figure 2.24 shows the pressure PSD on the surface at $x/c = 0.92$, and the far-field PSD for different angles of attack. In the light-stall regime, where the angle of attack is 15°, broadband noise can be seen for frequencies between 50 and 700 Hz with a similar increase

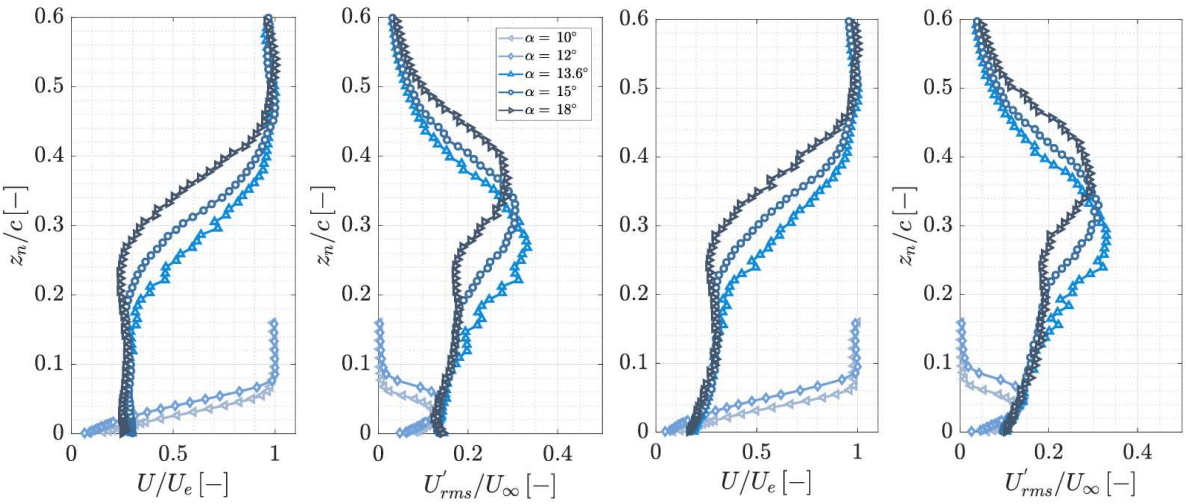

(a) $x/c = 0.93$ (b) $x/c = 0.98$

Figure 2.21: Boundary layer measurements from $\alpha = 10°$ to $\alpha = 18°$ [34].

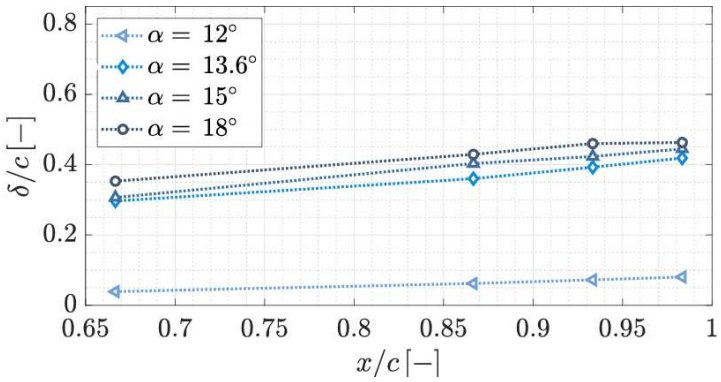

Figure 2.22: Boundary layer thickness for α from 12° to 18° [34].

in noise levels as seen in the first study shown in Figure 2.23. However, it is evident that for the study where the flow speed is set to 50 m/s, the noise levels are generally about 15 dB higher in comparison to the study with a flow speed of 25 m/s.

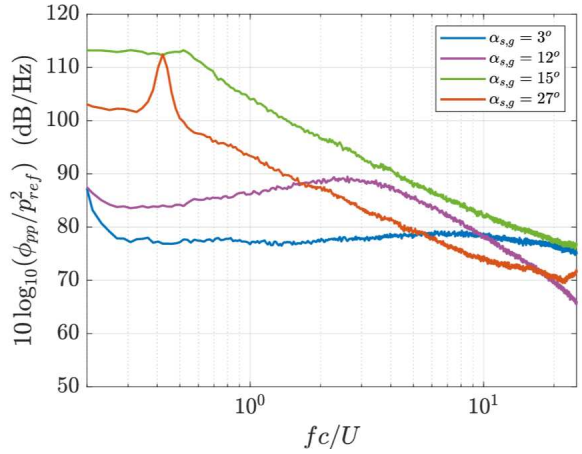

(a) Surface pressure PSD on the suction side at $x/c = 0.92$

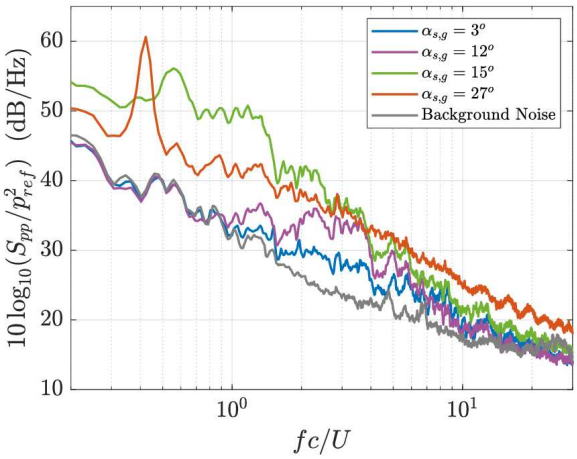

(b) Far-field noise spectra

Figure 2.23: NACA0012 acoustic results for α from 3° to 27°, $U = 50$ m/s [46].

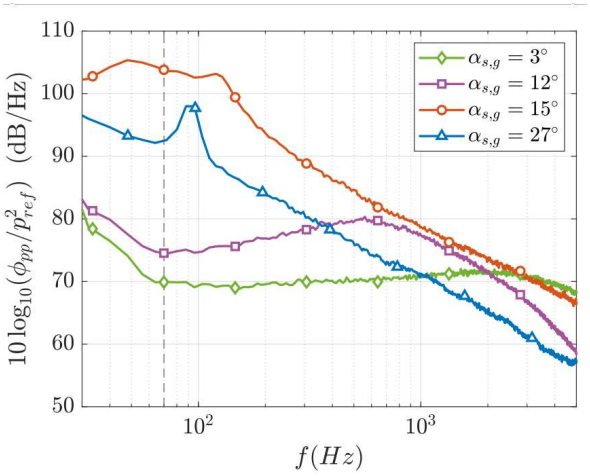

(a) Surface pressure PSD on the suction side at $x/c = 0.92$

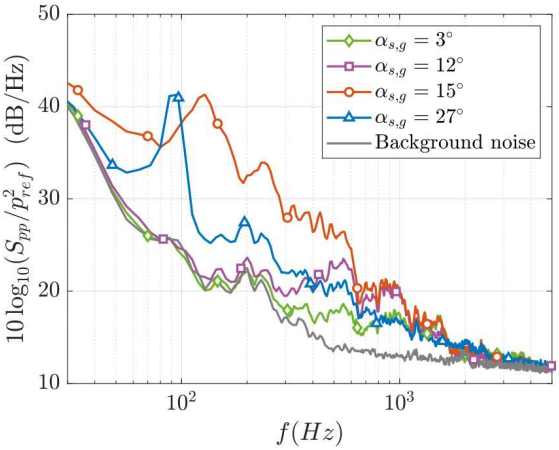

(b) Far-field noise spectra

Figure 2.24: NACA0012 acoustic results for α from 3° to 27°, $U = 25$ m/s [45].

2.8.2 Previous Work

Nataraj [40] has conducted a study revolving around the airfoil self-noise prediction using the FW-H analogy for NACA0021 in deep stall. The case parameters chosen were a chord length of 1 m, angle of attack 60°, a free-stream Mach number $M_\infty = 0.1$, and chord-based Reynolds number $Re_c = 2.7 \times 10^5$. The CFD simulation was run using the DDES turbulence model and the FW-H analogy was used to obtain the acoustic results. The results obtained are shown in Figures 2.25 and 2.26, where the Overall Sound Pressure Level (OASPL) directivity, far-field SPL spectra, and the SPL directivity are shown, respectively. The OASPL plot shown in Figure

2.25a resembles the noise signal power. In these results, the power of the noise is consistent in all directions. The angles in this plot are the azimuthal coordinates to the x axis. Figure 2.25b, SPL spectra at far-field with observer location on the midspan plane perpendicular to the airfoil chord at a distance of $r/c = 20$. In the case of airfoils in deep stalls, stall noise is indicated with two tonal peaks at lower frequencies, which is observed in this figure.

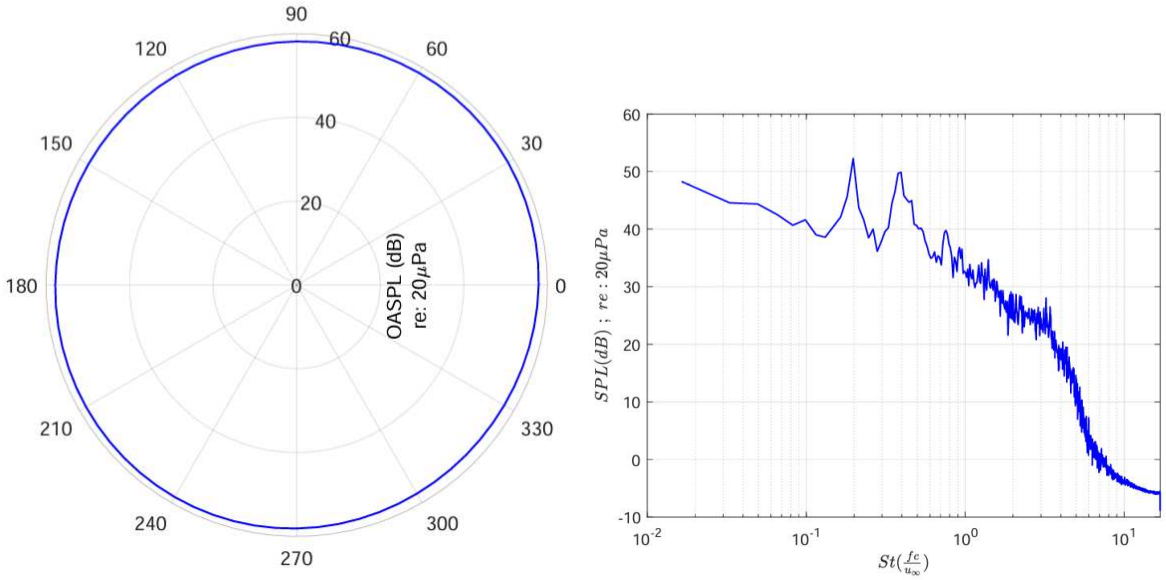

(a) OASPL directivity

(b) Far-field SPL spectra

Figure 2.25: NACA0021 acoustic results [40].

Figure 2.26, shows the SPL directivity for a range of different Strouhal and Helmholtz numbers. Nataraj [40] observes that for the Strohaul numbers 0.0165, and 1.2507 the acoustic field directivity plots are dipolar and symmetric. For Strohaul numbers 2.4850 and 3.7192 the directivity plots show dipolar shapes, however, the noise levels on the upper plane are higher. A quadruple pattern forms in the last two directivity plots for Strouhal numbers 4.9536 and 6.1879, where the airfoil transitions to a non-compact source. Nataraj [40] notes that normalizing the narrowband SPL spectra of NACA0012 aligns well with tonal frequencies in literature. An important discrepancy in the magnitude of the PSD is indicated, this is expected to be due to the difference in the span size between experiments and the span length used in this study. This issue is expected to be solved by either considering applying a long-span correction or obtaining the noise prediction from a flow solution that matches the span size used in experiments.

2.8.3 Spanwise Effects

In a study conducted by Aihara et al. [1], a correction method is carried out and examined on the acoustic pressure to account for the turbulence flow structures along the span of an airfoil. The purpose of this spanwise correction is to investigate the possibility of predicting the noise

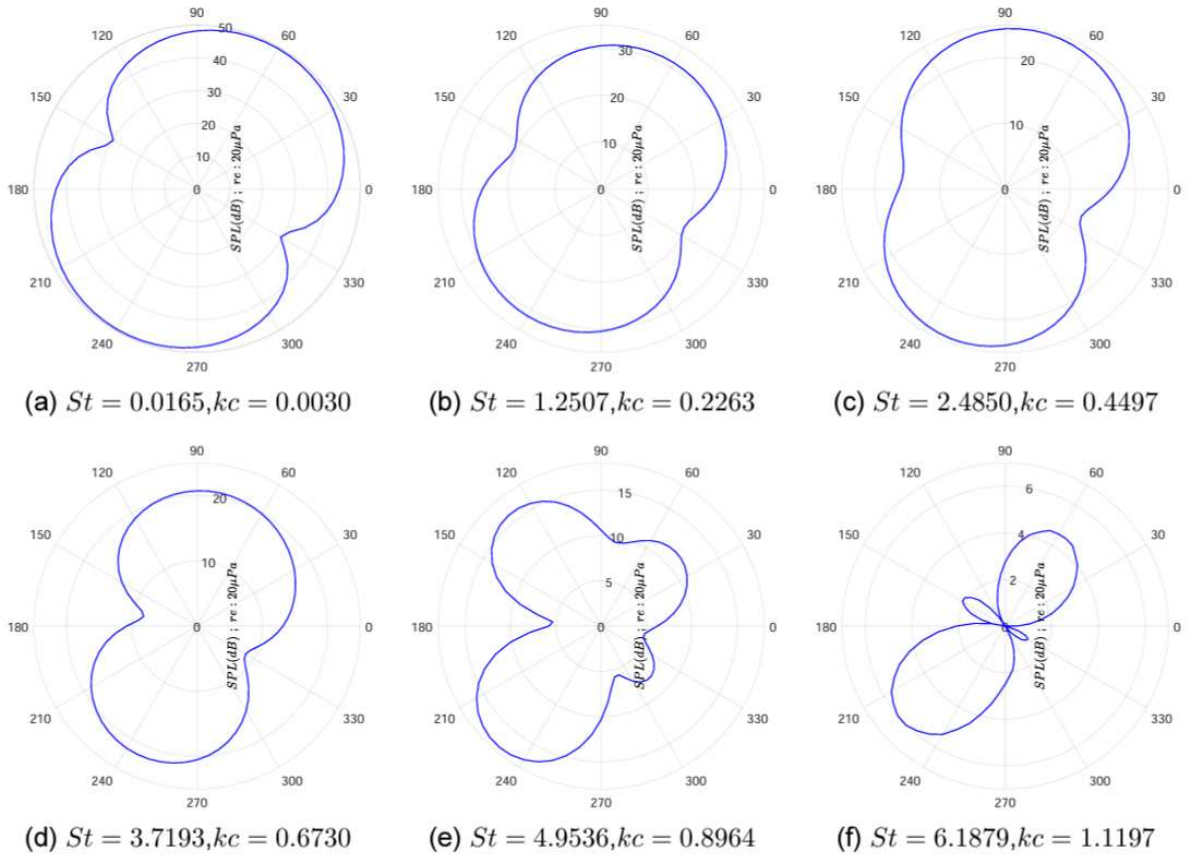

Figure 2.26: SPL directivity at different frequencies at $r/c = 20$ [40].

of a NACA 0012 airfoil by simulating a smaller domain in the spanwise extent. This correction has been conducted on an airfoil with a chord length of 10.16 cm in a stall region with an angle of attack of, 15.6° using LES and Curle's acoustic analogy. This study was conducted at a free-stream velocity of 71.3m/s, corresponding to a chord-based Reynolds number of 4.8×10^5, and a Mach number of 0.2. The far-field observer is located 11.8 chord lengths away from the trailing edge.

The correction has been investigated for two different simulated span lengths (Ls), 0.4c and 1.3c. These lengths are corrected and compared to the experimental span length model, $L = 4.5$c. Figure 2.27, shows 1/3 octave band SPL as a function of frequency for both cases before and including the correction. SPL_s refers to the sound pressure levels of the simulated span length only, and SPL_{all} includes the correction. SPL_{all} is defined as the sum of SPL_s and SPL_{cor}, where SPL_{cor} is the correction added as a function of frequency. The maximum and minimum values of the correction are 20.2 dB and 10.1 dB for the case with $L_s = 0.4$c, and 10.7 dB and 5.3 dB for the case with $L_s = 1.3$c. For both cases, the values are close at 500 Hz, but have a large difference. Aihara et al. [1] noted that the first case with a simulated span length of 0.4c is not adequate for accurately predicting the SPL at lower frequencies.

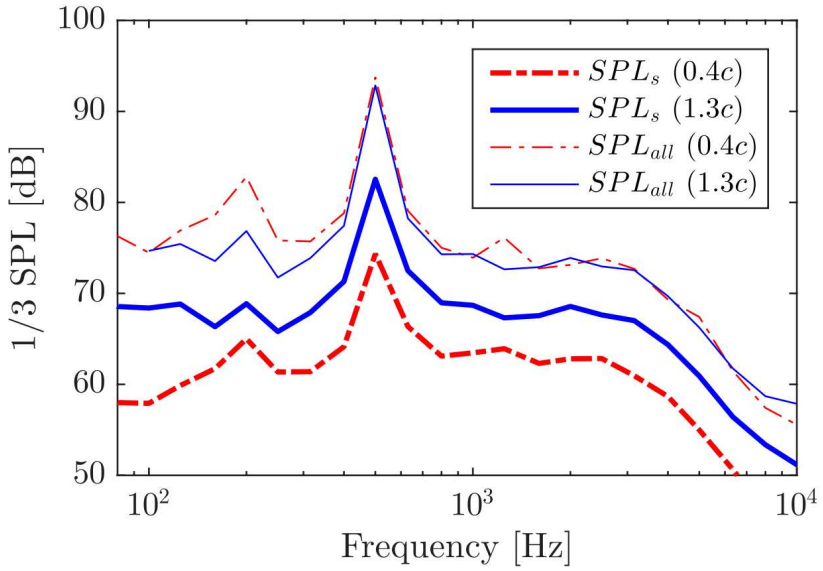

Figure 2.27: 1/3 octave band SPL for $L_s = 0.4c$ and $L_s = 1.3c$ before and after the correction [1].

It is significant to consider the spanwise extent that will be corrected. Additionally, the size of the simulated span length can also affect the correction. Turner and Kim [59] studied three different spanwise domain sizes to determine how large the spanwise domain should be to obtain accurate aeroacoustic results from numerical simulations of an airfoil in stall. The flow data in the study were obtained using DNS of a NACA 0012 airfoil with a Reynolds number of $50,000$ and a Mach number of 0.4, where the acoustic field was predicted using FW-H. The three span lengths considered were 0.2c, 0.6c, and 1c. The far-field observer locations were positioned at a distance of 5c above the mid-chord of the airfoil. The FW-H integration surface domain is 3c for all cases. In other words, for $L_s = 0.2$c the domain was repeated 15 times, for $L_s = 0.6$c the domain was repeated 5 times, and for $L_s = 1$c the domain was repeated 3 times.

Figure 2.28 shows the far-field SPL results conducted by Turner and Kim [59] at an angle of attack $\alpha = 15°$ averaged over $84° \leq \theta \leq 96°$. It can instantly be observed that using a smaller span leads to a significant overprediction in the acoustic pressure compared to the larger span lengths. Moreover, the peak frequency is inaccurately predicted for the span length of 0.2c, with a Strouhal number of 0.639, whereas the other two span lengths predict the peak at 0.775. There is a difference of about 10 dB or more between the smallest span length and the medium or larger span lengths for Strouhal numbers lower than 10.

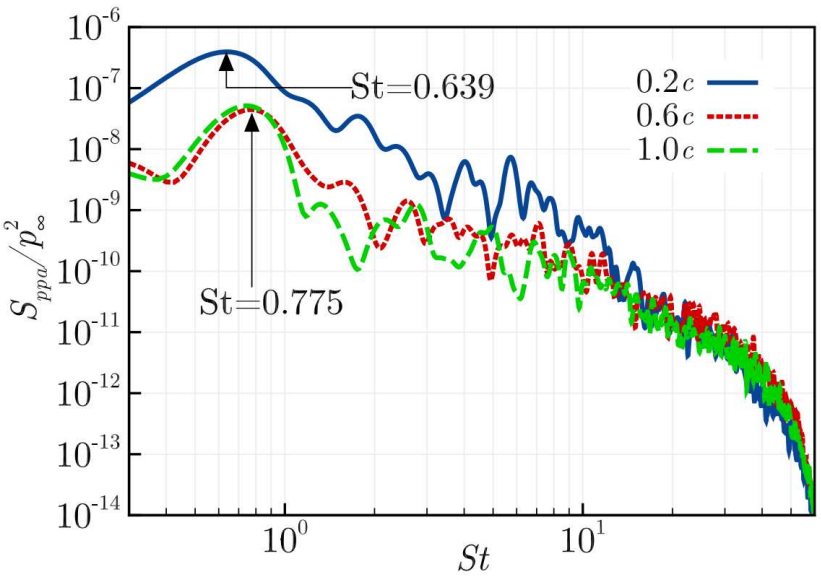

Figure 2.28: Far-field SPL for NACA 0012 at $\alpha = 15°$ [59].

Chapter 3

Objectives

The self-noise mechanisms of airfoils have been extensively studied, with various models investigating different flow conditions. However, stall-related noise has received less attention compared to other regimes. Previous research, including a recent thesis by Nataraj [40], focused on the noise prediction of airfoils in deep-stall conditions. To build on this work, this study focuses on addressing the gap in understanding noise prediction during light-stall.

The primary goal of this thesis is to investigate the aerodynamic and acoustic predictions of the NACA0012 airfoil under light-stall conditions using a DDES-FWH framework. This research aims to deepen understanding of how light-stall influences airfoil noise prediction and to explore the effectiveness of spanwise correction techniques in improving noise predictions. The research questions of this study are:

- What is the relationship between the aerodynamic characteristics of the NACA0012 airfoil at light-stall and the resulting far-field acoustic signatures?
- How does the span length of the computational domain influence the predicted noise levels of the NACA0012 airfoil, and how can spanwise correction mitigate these influences?
- How do computational predictions of aerodynamic and acoustic characteristics of the NACA0012 airfoil at light-stall compare with experimental data?
- How do spanwise corrections affect the identification and characterization of tonal versus broadband noise components in the far-field acoustic signature of the NACA0012 airfoil?
- How can the integration of the spanwise correction technique with advanced turbulence modeling improve the prediction of noise levels for airfoils in light-stall conditions?

The research questions are used to outline the results section, where the aerodynamics analysis, acoustic analysis, spanwise correction, comparison with experiments, and the influence of spanwise correction on results are presented.

Chapter 4

Methodology

This chapter outlines and describes the approach taken to obtain the aerodynamic and acoustic results for the aforementioned objectives in the previous section. The process integrates the SU2 software suite [13], which is an advanced CFD tool. SU2 has been used to simulate the complex flow characteristics associated with light-stall for the case of NACA0012 airfoil. Along with SU2, the FW-H solver has been used to predict the far-field noise generated by these aerodynamic conditions. This chapter includes the geometry preparation, mesh generation, simulation setup, FW-H solver, and the spanwise correction technique.

4.1 CFD Solver

The SU2 software suite [13] is designed to solve partial differential equations (PDE) and optimization problems involving PDE constraints on unstructured meshes. The software's core function is a RANS solver, although the framework is adaptable for various multiphysics analysis and design problems. This solver is particularly suited for simulating compressible, turbulent flows, making it highly relevant for aerospace and mechanical engineering applications.

4.1.1 Code Framework

The primary components of the SU2 suite are the C++ executables, with each executable with a specific function. These tools take full advantage of modern programming language features, ensuring that each module operates efficiently and effectively. The C++ tools are: SU2_CFD, SU2_DEF, SU2_DOT, SU2_GEO, SU2_MSH, and SU2_SOL [13].

SU2_CFD is used to solve adjoint, direct, and linearized problems for different equation sets such as Euler, Navier-Stokes, RANS nonequilibrium, Poisson, wave, etc. It uses a Discontinuous Galerkin Finite Element Method (DG-FEM) or Finite Volume Method (FVM). The software includes various advanced capabilities designed to enhance its robustness and improve the speed and reliability of convergence. SU2_DEF is a tool used in mesh deformation. It calculates the

deformation of a surface in a volumetric grid, which consists of the mesh and the surrounding nodes. This tool also offers several geometry parametrization techniques, which include free-form deformation (FFD) in two and three dimensions, and different bump functions in two dimensions. SU2_DOT is a tool where a dot product operation is used to calculate the derivative of a particular function. These functions include drag, lift, etc. An adjoint solution from SU2_CFD is used along with geometrical design variables. SU2_GEO tool is used to evaluate different geometric quantities such as volumes, etc. SU2_MSH is a tool used to perform mesh adaptation using different methods depending on the analysis of the flow to refine the mesh based on the key features in the flow. SU2_MSH is responsible for creating ghost cells, which are virtual boundary cells, for simulations with periodic boundary conditions. This tool then returns a new mesh where the periodic faces have a suitable communication structure. For all cases where the simulation uses periodic boundary conditions, SU2_MSH should be executed before SU2_CFD. SU2_SOL is the tool responsible for generating the surface and volume solution files. This is automatically executed and called by parallel_computation.py after running a parallel calculation using SU2_CFD. This tool can also be independently called if a mesh, configuration, and restart file containing the solution at each node is present.

4.1.2 Turbulence Model

The simulation used in this study is the DDES. As previously mentioned in Section 2.7, DDES is a newly developed method based on DES. It was proposed to resolve the issues regarding the premature transition to LES. This occurs when a scenario with shallow separation regions has a boundary layer thickness larger than the wall-parallel spacing in the mesh. Early transition to LES results in the deficient generation of turbulence in areas meant to be resolved, which can lead to Modelled Stress Depletion (MSD), and Grid Induced Separation (GIS). MSD refers to the reduction of turbulent stress caused, and GIS refers to the early flow separation. This method was implemented in SU2 by Molina et al. [37].

The use of the standard DDES SGS length scale Δ_{max} by Deck [9] was linked to the delay of instability formation in the free shear layer. Deck [9] has also contributed by adjusting a version of the SGS length scale, Δ_ω, specifically for zonal DES. This modification aims to address the common issue of separation caused by an adverse pressure gradient or geometry in flow problems. The modified SGS length scale Δ_ω for unstructured grids is expressed as

$$\Delta_\omega = \sqrt{\bar{S}_\omega} \tag{4.1}$$

where $\bar{S}_\omega$ represents the mean cross-sectional area of the cell perpendicular to the local vorticity.

The standard definition of DDES using the Δ_{max} length scale leads to a delay in the onset of KH instabilities, hindering their transition to turbulence. The Δ_{max} by definition overestimates the SGS eddy viscosity. The previously developed Δ_ω length scale has the same issue, even though it is considered an advancement. In an attempt to solve the problem at

hand, a modified version of the Δ_ω length scale, $\tilde{\Delta}_\omega$, has been defined for hexahedral cells [53]. However, this has also been overpredicting the SGS eddy viscosity. Shear Layer Adapted (SLA) SGS length scale (Δ_{SLA}) has been developed by modifying the $\tilde{\Delta}_\omega$ length scale. Δ_{SLA} consists of a non-dimensional function with an argument known as Vortex Tilting Measure (VTM), which detects regions in the initial shear layers where the KH instabilities are expected to form.

4.2 Numerical Methods

In this section, a brief description of the numerics available and the choices made for the SU2 simulation in this study will be provided. This will be divided into the spatial integration, time integration, and the convective schemes. All chosen parameters in the simulations are discussed in this section, parameters that are set by default will not be explored.

4.2.1 Spatial Integration

Spatial integration refers to the division of the computational domain into grids. Approximate solutions are obtained by reducing the governing equations using different numerical methods such as Finite Volume Method (FVM), Finite Element Method (FEM), and Finite Difference Method (FDM). FVM is based on the integral form of the governing equations, applied over discrete control volumes that make up the flow domain. Using the Gauss divergence theorem, volume integrals are transformed into surface integrals, which are then evaluated numerically. This leads to a set of linear algebraic equations that must be solved for each control volume. Unlike the Finite Difference Method (FDM), FVM allows the use of structured, unstructured, or arbitrary grids. The compressible RANS solver based on the FVM was selected in this study's simulations. A first-order upwind scheme is used to discretize the convective term in the SA turbulence model spatially. To compute gradients, the Weighted Least Squares (WLS) method is employed, ensuring accurate evaluation of flow variables across the computational grid [43].

4.2.2 Convective Schemes

In SU2, the convective fluxes can be approximated using centered or upwind discretization schemes. There are several numerical schemes implemented in SU2, this includes Jameson-Schmidt-Turkel (JST) [23], Roe [48], AUSM [31], and HLLC [57]. However, JST and Roe schemes will only be discussed as they are the most commonly used in practice. The JST scheme uses a central difference which utilizes an artificial dissipation term to stabilize the solution near shock waves and minimize unnecessary diffusion in smooth regions [23]. Roe's Scheme uses an upwind discretization, accounting for wave propagation's direction. This makes it particularly well-suited for flows with strong convective effects and discontinuities. Even though the upwind discretization has lower accuracy, it is rewarded for its robustness and ability to handle complex flows [48]. For the simulations in this study, JST numerical scheme was chosen.

4.2.3 Time Integration

In SU2, different methods can be used to address unsteady flows. These methods are implicit and explicit Euler schemes and Runge-Kutta. The implicit Euler method is the easiest way to discretize the system. It offers stability and allows for a larger Courant-Friedrichs-Lewy (CFL) number, a dimensionless number used in solving partial differential equations. A larger CFL number leads to bigger time steps and faster convergence. On the other hand, the explicit Euler method is more stable but requires small time steps, causing the simulation to be less efficient. The Runge-Kutta method provides an increased level of accuracy. For the simulations in this study, the Euler implicit method has been used for its mentioned benefits.

For simulations with unsteady flows, a dual-time-stepping strategy is recommended for time-accurate calculations. This method converts the unsteady problem into a sequence of steady problems at each physical time step, allowing each to be solved successively. The chosen strategy in the simulations of this study is the second-order dual time stepping, where a devised time variable (τ) is used to converge the steady state problem [13]. The use of this method results in the application of two distinct CFL numbers. The unsteady CFL number is for the physical time domain and the steady CFL number is related to the devised time domain. The unsteady CFL number is ignored due to the choice of the Euler implicit method in the time integration, the steady CFL number affects the time-step selection in the devised fictitious time. A CFL number of 10 was chosen for great convergence in the steady-state solutions.

4.3 FW-H Analogy

This section will delve into continuing the CFD-CAA process. The CAA part includes the integral solver of the FW-H, this is done using a Python script developed by Molina [36]. This script was developed and used to predict the far-field noise generated for a model of a plane landing gear. In this solver, the FW-H integral solution used is derived by Farassat [16] for permeable surfaces in the time domain.

4.3.1 FW-H Integral Solution

The FW-H integral solution, derived by Farassat [16], is formulated differently than what is expressed in Section 2.4.2 while maintaining. The variation in acoustic pressure as a function of

the observer's location and time is expressed as

$$
\begin{aligned}
4\pi p'(\mathbf{x},t) = &\int_S \left[\frac{\dot{Q}_n}{r(1-M_r)^2}\right]_{\tau=\tau*} dS + \int_S \left[\frac{Q_n c_\infty (M_r - M^2)}{r^2(1-M_r)^3}\right]_{\tau=\tau*} dS \\
&+ \frac{1}{c_\infty}\int_S \left[\frac{\dot{L}_r}{r(1-M_r)^2}\right]_{\tau=\tau*} dS + \int_S \left[\frac{L_r - L_M}{r^2(1-M_r)^2}\right]_{\tau=\tau*} dS \\
&+ \frac{1}{c_\infty}\int_S \left[\frac{L_r(M_r - M^2)}{r^2(1-M_r)^3}\right]_{\tau=\tau*} dS
\end{aligned}
\tag{4.2}
$$

$$
L_i = (\rho v_i(v_j - V_j) + p_{ij})n_j \qquad Q_n = (\rho v_j - \rho' V_j)n_j \tag{4.3}
$$

where τ is the emission time, τ^* is the corrected retarded time given by $\tau^* = t - r(\tau^*)/c_\infty$, r is the distance from the data surface to the observer defined as $r = |\mathbf{x} - \mathbf{y}|$, v_j is component of the fluid velocity at the surface, V_j is the component of the surface velocity in the i direction, and n_j is the component of the unit surface normal. M_r is defined as $M_i\hat{r}_i$ which is the Mach number of the source in the observer direction, similarly, $L_r = L_i\hat{r}_i$, $L_M = L_i M_i$, and $\dot{L}_r = \dot{L}_i\hat{r}_i$. It should be noted that $\dot{Q}_n$ and $\dot{L}_r$ are time derivatives with respect to the emission time τ. Equation 4.2 can be simplified further for a fixed solid FW-H surface and a fixed observer as the variables V_j, v_j, and M_i are zero. The implemented simplified integral solution in the FW-H script is shown in Equation 4.4.

$$
4\pi p'(\mathbf{x},t) = \frac{1}{c_\infty}\int_S \left[\frac{\dot{L}_r}{r}\right]_{\tau=\tau*} dS + \int_S \left[\frac{L_r}{r^2}\right]_{\tau=\tau*} dS \tag{4.4}
$$

4.3.2 FW-H Script

This subsection will explain the script's operation in more detail. The script implements the simplified integral solution presented in Equation 4.4. The necessary variables required for obtaining the acoustic pressure are the local pressure perturbations, surface normal vectors, CFD data at every time step, and the vectors from the FW-H surface to the observer locations, known as radiation vectors. Figure 4.1 shows a flowchart of the necessary steps to be taken. The blocks consist of user-defined functions, input, and output files. The Surface Pressure Data, User Inputs, and Binary Data file are the inputs used in the FW-H script. Observer Noise Data is the output acoustic pressure data file. The rest of the blocks are defined functions responsible for the generation of the far-field acoustic pressure data file, except for the *CSVToArray* and *write_binary_fwh* which are responsible for generating the Binary Data file.

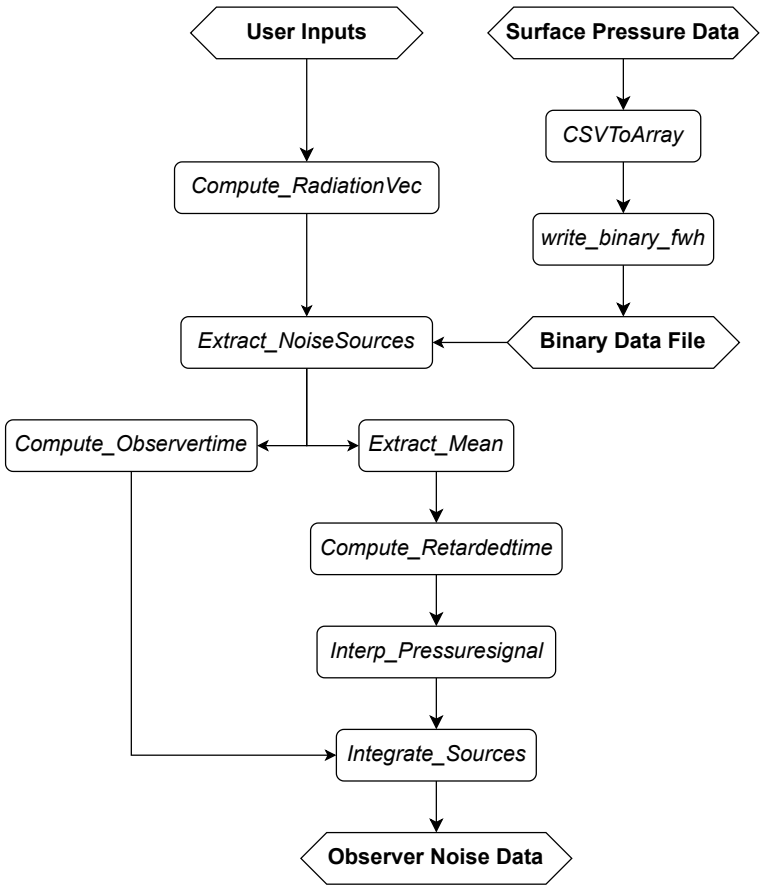

Figure 4.1: Flowchart of the FW-H script.

Input Files

The input files consist of the Binary Data file, Coordinate Normals file, Surface Coordinate file, and Observer Location file, where all those files except for the latter are obtained from the surface pressure data files. The user inputs that are required to be set are the sampling frequency, the number of dimensions, the type of analogy, the time step, and the starting iteration number. From those inputs, the type of analogy and number of dimensions are set by default to 1A and 3, respectively.

SU2 outputs the surface pressure data files directly with the preferred writing frequency. As SU2 writes the data at the cell vertices, the data is interpolated to the cell centers as a requirement for the FW-H script to operate properly. The airfoil surface in this case is considered to be the FW-H integration surface, where the no-slip and adiabatic boundary conditions are applied. The surface coordinates are extracted from the surface pressure data files at the center of the cells, and the surface normals are generated at those locations. In Figure 4.2 the surface

coordinates are plotted in blue and the unit surface normal vectors are shown in red. The interpolation from cell vertices to cell centers and generation of the coordinates for unit surface normals are made using ParaView [21]. The Coordinate Normals file consists of the cell center coordinates, surface normals coordinates, and the area of the cells.

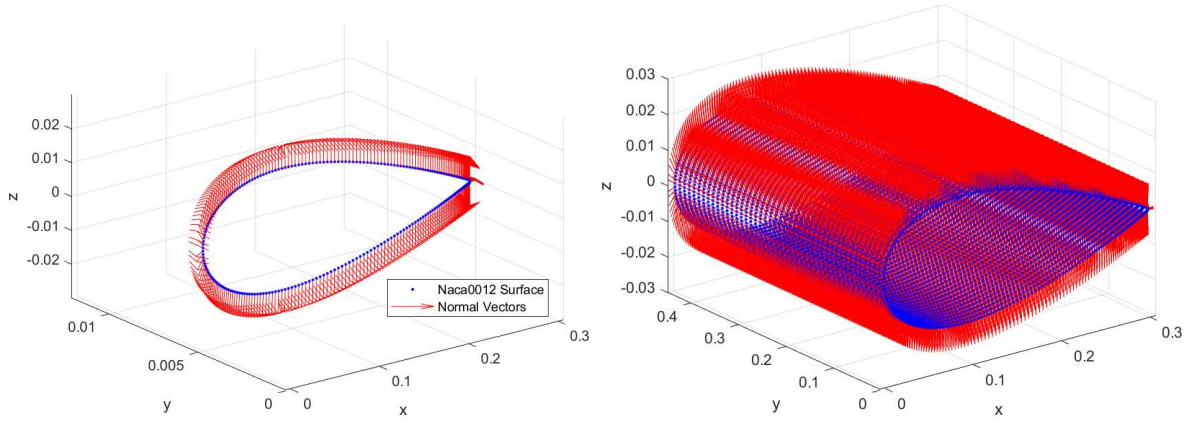

(a) (b)

Figure 4.2: Surface and surface normal vectors

Lastly, the observer location file is created with the desired locations at the far-field. This is required to calculate the acoustic pressure data, and observer times at those locations. The acoustic results aimed for are the directivity data and noise spectra, for this purpose a simple circular pattern of observers around the surface with a desired distance is sufficient. The observer locations for one of the cases in the study are shown in Figure 4.3, where a total of 40 observers are evenly distributed in a circular pattern around the mid-span of the airfoil surface at a distance of 5.8 the chord length. In this graph, two extra observer locations, marked in red, were added for further analysis at those specific locations. The number of observer locations was kept constant at 40 points for all cases in this study, with varying distances from the surface.

Output File

The output file generated is the observer noise date. This file consists of the predicted acoustic pressure and the observer times at the chosen observer locations at every time step.

User Defined Functions

The functions used in the FW-H script that are responsible for the generation of the Observer Noise Data shown in Figure 4.1 will be briefly discussed.

The surface pressure data for all the time steps written are combined into a single Binary Data File for a more convenient and efficient procedure. This is done by using the *CSVToArray* and *write_binary_fwh* functions. The *CSVToArray* is responsible for assigning the surface pressure data files (*.csv*) into a 2D array where the columns are the point indices and the rows

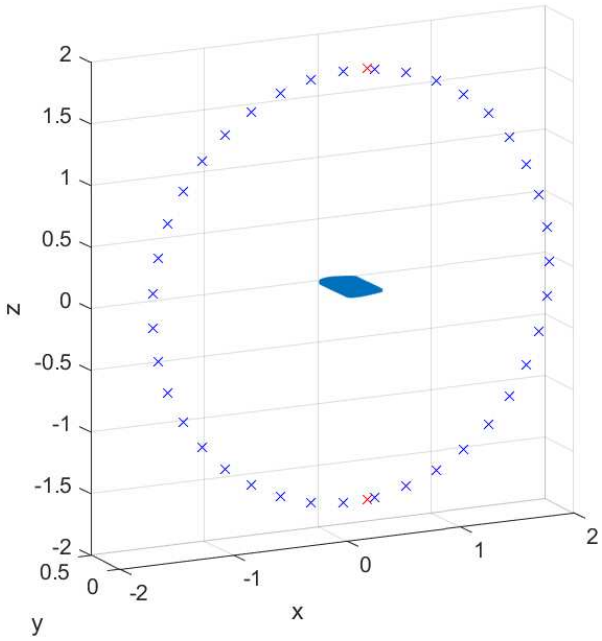

Figure 4.3: Observer locations at 5.8 the chord length

are the number of iterations. The *write_binary_fwh* function is then responsible for combining the results from the *CSVToArray* into a binary file.

The *Compute_RadiationVec* function is the first user-defined function in the Python script. This function is initiated after setting the Surface Coordinate, Coordinate Normals, Binary Data, and Observer Location files along with the input variables. It generates radiation vectors between all the cell-centered points to each observer location. The result is an array of all the vectors' components and their magnitude.

The *Extract_NoiseSources* function is responsible for calculating the loading term in the direction of the radiation vector, L_r. This is computed for every time step and cell.

The function *Extract_Mean* is used to calculate the desired fluctuating part of L_r for the surface integral. This is determined by subtracting the time-averaged value, from the value of L_r at every time step.

The *Compute_RetardedTime* function evaluates the integrands in Equation 4.4. As L_r is calculated, the next step to evaluate the integrands is to compute the time derivative of the term L_r with respect to the emission time for all time steps. This was possible by using a second-order central differencing scheme. The *Compute_Retardedtime* then computes the integrands of the surface integral and assigns it to the array *pp_ret*.

The *Compute_Observertime* function calculates the observer time for every cell, time step, and observer location. This is calculated using the following equation.

$$t = \tau + \frac{r}{c_\infty} \tag{4.5}$$

The *Interp_PressureSignal* function is used to cubically interpolate the calculated *pp_ret* in terms of the emission time τ to observer time t.

Finally, the function *Integrate_Sources* is used to calculate the surface integral in Equation 4.4 and obtain the far-field acoustic pressure fluctuation $p'(\mathbf{x}, t)$. The results are written for the indicated observer locations and times in the Observer Noise Data file.

4.4 Acoustic Post-processing

After following the CFD-CAA framework, the outcome is the raw acoustic pressure data at the defined observer locations. It is necessary to post-process the data to understand and analyze the sound signatures. This is done by obtaining the Sound Pressure Level (SPL) spectrum, SPL directivity, and Overall Sound Pressure Level (OASPL). Sound is generally measured on a decibel scale, as the human ear's sensitivity is logarithmic. This scale is referred to as SPL, and the acoustic pressure time series determines it. SPL is expressed as

$$SPL(f) = 10log_{10}(\phi_{FF}(f)/p_{ref}^2) \tag{4.6}$$

where ϕ_{FF} is the PSD of the far-field acoustic pressure determined using Welch's PSD estimate [61], and p_{ref} is the reference pressure. SPL can also be calculated by replacing ϕ_{FF} with ϕ_{pp}, which is the PSD of the surface pressure. The reference sound pressure is determined based on applications. For aerial applications, the standard p_{ref} is $20\mu Pa$. Plotting the SPL directivity is obtained when SPL is calculated at different observer locations in the far-field. It can show the monopole and multipole effects at different frequencies. The SPL spectrum is calculated at the desired observer location to evaluate the noise signature at different frequencies.

The OASPL is expressed as

$$OASPL = 20log_{10}(p_{rms}/p_{ref}) \tag{4.7}$$

where p_{rms} is the root-mean-square pressure. It is defined as the time average of the square of the fluctuating pressure. p_{rms} is expressed as

$$p_{rms} = \sqrt{\frac{1}{2T}\int_{-T}^{T} p'(t)^2 dt} \tag{4.8}$$

where $p'(t)$ is the time-varying pressure perturbation given as

$$p'(t) = p(t) - p_0 \tag{4.9}$$

p_0 is the average background pressure and $p(t)$ is the pressure at a given point in the fluid.

4.5 Spanwise Correction

The predicted acoustic pressure data at the far-field is typically analyzed by assuming the turbulence at the airfoil is homogenous. However, the noise prediction for a stalled airfoil requires correction, as the characteristic length of the vortex shedding is larger compared to an airfoil at lower angles of attack. The spanwise correction that is used in this study is proposed by Seo et al. [52] where it was used to correct the acoustic pressure based on the turbulence flow structure along the span for long-span bodies. This correction is beneficial in practice, as it can predict the sound pressure of airfoils by simulating the case with a smaller span length. This would result in more efficient simulations with fewer computational constraints.

4.5.1 Fundamentals

The SPL for the airfoil's simulated span (L_s) must be corrected to approximate the SPL for the entire span (L). The correction method proposed by Seo et al. [52] has been made by revisiting previous work from Kato et al. [24] and Perot et al. [44] for long-span bodies. Kato et al. [24] introduced the SPL correction by adding $10log(L/L_s)$ if $L_c \leq L_s$ or $20log(L/L_s)$ if $L_c > L$, where L_c is the coherence length of the pressure fluctuations. However, this correction is only limited to $L_s \leq L_c \leq L$. Perot et al. [44] has also introduced a correction method based on Curle's analogy which provides more accurate results in the near-field. Nevertheless, this method has not been fully adapted for practical application.

The first step in the method proposed by Seo et al. [52], is to divide the length of the airfoil into N subsections of L_s so that $L = N \cdot L_s$. Figure 4.4 shows the division of the airfoil, where $\hat{p}'_L$ is the PSD of the acoustic pressure for the entire span length, and $\hat{p}'_i$ is for the subsection N_i. The SPL for the entire span, L, is expressed as

$$SPL_{all} = SPL_s + SPL_{cor} \tag{4.10}$$

where SPL_s is the calculated SPL for the simulated span L_s and SPL_{cor} is the correction added defined in Equation 4.11.

$$SPL_{cor}(f) = \begin{cases} 20log\left(\frac{L}{L_s}\right) & \left(\frac{L}{\sqrt{\pi}L_s} \leq \frac{L_c}{L_s}\right) \\ 10log\left(\frac{L_c}{L_s}\right) + 10log\left(\frac{\sqrt{\pi}L}{L_s}\right) & \left(\frac{1}{\sqrt{\pi}} < \frac{L_c}{L_s} < \frac{L}{\sqrt{\pi}L_s}\right) \\ 10log\left(\frac{L}{L_s}\right) & \left(\frac{L_c}{L_s} \leq \frac{1}{\sqrt{\pi}}\right) \end{cases} \tag{4.11}$$

The first term in Equation 4.11 is applied when the pressure fluctuations are uniform and in phase, when those fluctuations are irregular the last term is used. When the phase shift of the pressure fluctuations falls in a range between the previous expressions, the middle term is applied. The modulus of the acoustic pressure PSD emitted is the same for each subsection.

$$|\hat{p}'_1| = |\hat{p}'_2| = ... = |\hat{p}'_N| = |\hat{p}'_s| \tag{4.12}$$

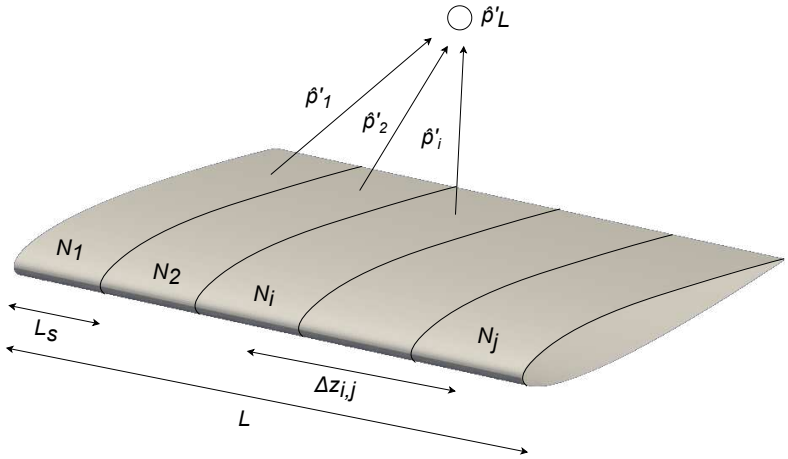

Figure 4.4: Schematic of the spanwise correction

where $\hat{p}'_s$ is the PSD of the acoustic pressure emitted from the span L_s. The acoustic pressure emitted from each subsection, shown in Figure 4.4, is delayed by a phase shift described using the following coherence function

$$\gamma'_{i,j} = \frac{\overline{Re(\hat{p}'_i \hat{p}'^*_j)}}{\sqrt{|\hat{p}'_i|^2}\sqrt{\left|\hat{p}'_j\right|^2}} \tag{4.13}$$

where $*$ denotes a conjugate. Using this function, the coherence length L_c can be calculated. The coherence function is a function of frequency f and the spanwise distance between two subsections $\Delta z_{i,j}$.

$$\gamma'_{i,j} = \gamma'(\Delta z_{i,j}), \qquad \Delta z_{i,j} = |z_i - z_j| = |i - j| \cdot L_s \tag{4.14}$$

Since the phase lagging follows a Gaussian distribution in the spanwise direction, the coherence function $\gamma'(\Delta z_{i,j})$ can be expressed as the following.

$$\gamma'(\Delta z_{i,j}) = \exp\left(-\frac{\Delta z_{i,j}^2}{L_c^2}\right) \tag{4.15}$$

The coherence length L_c in Equation 4.15 is determined for the SPL correction to fit the Gaussian distribution for a set of $\Delta z_{i,j}$ and $\gamma'_{i,j}$ calculated in Equation 4.13.

4.5.2 Spanwise Correction Script

This subsection will dive into the process of applying the SPL correction in more detail. Figure 4.5 shows a flowchart of the necessary steps for the spanwise correction. As this correction is applied in the post-processing, multiple operations in the FW-H script will be used. In the flow

chart, the cells shaded in blue are the extra steps taken apart from the FW-H script. The white cells are repeated from Section 4.3.2.

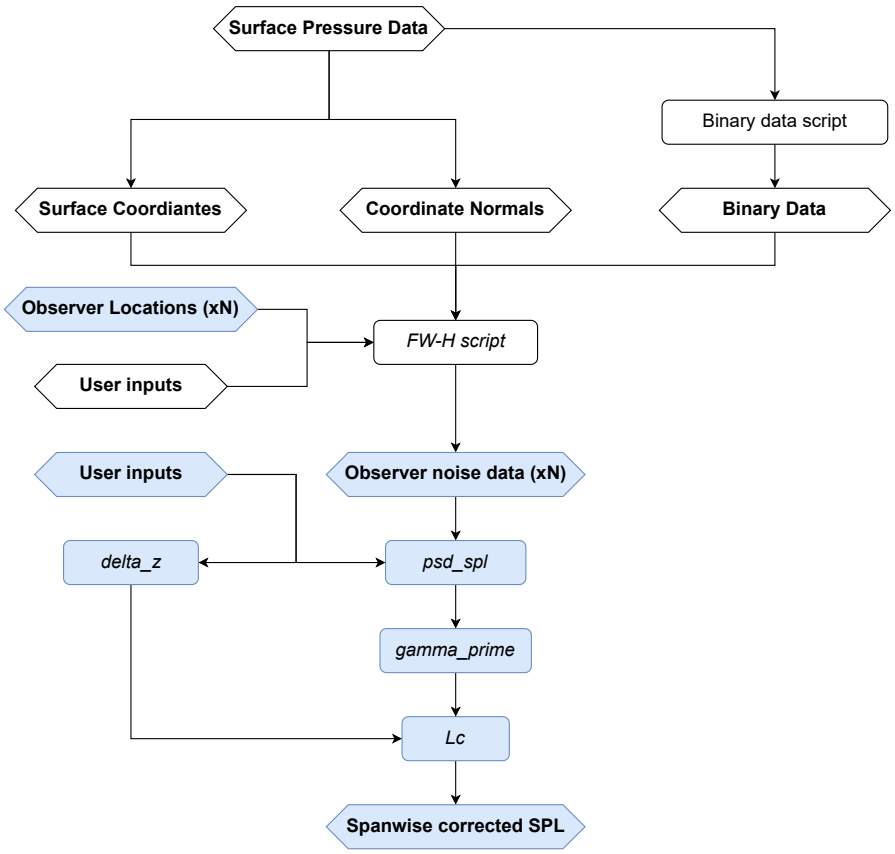

Figure 4.5: Flowchart of the spanwise correction.

As previously explained, the Surface Pressure Data obtained from SU2 is used to generate the Surface Coordinates, Coordinate Normals, and Binary Data files. These files along with the user inputs and observer locations are used in the FW-H script. In this case, the number of Observer Locations files must be made according to the number of sections N based on its position to the observer at the far-field. Using these files in the FW-H script, Observer Noise Data files will be generated based on the number of sections.

The blue User Inputs consist of specifying the chord length c, free-stream velocity U_∞, the simulated span length L_s, the number of sections N, and the reference sound pressure p_{ref} which is typically $20\mu Pa$ as previously mentioned in Section 4.4.

The *psd_spl* is a function where the PSD of the far-field acoustic pressure is determined using Welch's PSD estimate [61]. *delta_z* is a variable where the $\Delta z_{i,j}$ in Equation 4.14 is calculated, and *gamma_prime* is a variable where the $\gamma'_{i,j}$ in Equation 4.13 is calculated. A data set for the $\Delta z_{i,j}$ and $\gamma'_{i,j}$ have been obtained, the value of the coherence length L_c is estimated

using a linear system

$$A = L_c \cdot B \tag{4.16}$$

where

$$A = \sqrt{ln\left(\frac{1}{\gamma'_{i,j}}\right)}, \qquad B = \Delta z_{i,j} \tag{4.17}$$

Chapter 5

Results and Discussion

In this chapter, the results of this thesis will be presented. This includes the findings of the CFD simulation and the acoustic analysis conducted on the NACA0012 airfoil at light-stall, angle of attack of $\alpha = 15°$. This chapter systematically details the aerodynamic performance metrics and the far-field acoustic signatures obtained through the simulations. Additionally, it explores the impact of spanwise correction techniques on the accuracy of noise predictions, comparing the computational outcomes with experimental benchmarks and addressing the research questions posed earlier.

5.1 NACA0012 Test Case

5.1.1 Test Case Description

The test case for this study focuses on the NACA0012 airfoil, with all the relevant parameters listed in Table 5.2. In the table, Case 1 is compared to the experimental results from Mayer [34] and Case 2 with Raus et al. [46] from Table 5.1. As the airfoil in the light-stall configuration will start to experience significant flow separation on the upper surface, a different choice of span length might lead to an incorrect prediction. Therefore, the span lengths were chosen to resemble the experimental models closely. Such a choice tends to be more computationally expensive, thus a spanwise correction method where a smaller span is corrected to the desired length has been investigated in this chapter. In Mayer's experiment, a tripping tape was placed on the airfoil at $x/c = 0.1$. In the experiment conducted by Raus, the tripping tape was placed between $x/c = 0.2$ and $x/c = 0.4$ on both sides. The acoustic measurements and static and dynamic pressure information are provided in those experimental studies.

Parameters	Mayer [34]	Raus et al. [46]
Chord length (c)	0.3 m	0.12 m
Span length (b)	0.5 m	0.3 m
Chord-based Reynolds number (Re_c)	4.2×10^5	4.1×10^5
Free-stream velocity (U_∞)	20 m/s	50 m/s
Free-stream Mach number (M_∞)	0.058	~ 0.1458
Free-stream temperature	293.15 K	-
Angle of attack (α)	15°	15°

Table 5.1: Flow parameters in experiments for the NACA0012 light-stall.

Parameters	Case 1	Case 2
Chord length (c)	0.3 m	0.12 m
Span length (b)	0.45 m	0.3 m
Chord-based Reynolds number (Re_c)	4.1×10^5	4.1×10^5
Free-stream velocity (U_∞)	20.12 m/s	50 m/s
Free-stream Mach number (M_∞)	0.058	0.1458
Free-stream temperature	300 K	293 K
Angle of attack (α)	15°	15°

Table 5.2: Flow parameters for the simulated NACA0012 cases.

Mesh and Boundary Conditions An O grid mesh has been made for both cases where the elements are fine near the surface of the airfoil and coarsen towards the far-field boundary. For Case 1, the far-field is set as a circular domain that extends up to $90c$ with a mesh consisting of about 2×10^6 hexahedral elements. For Case 2, the mesh for Case 1 has been modified and scaled down to match the corresponding chord and span lengths in the experiments. This mesh consists of 3.4×10^6 hexahedral elements. The meshes have a $y+$ value of approximately 1 in the direction normal to the wall. This ensures that the turbulence near the wall is captured accurately. As DDES simulations are computationally intensive, a mesh refinement analysis has not been made.

In both simulations, the no-slip and adiabatic boundary conditions were applied to the airfoil surface. The far-field boundary condition has been applied to the outermost surface, and a symmetric boundary condition was also used. Figure 5.1 shows the grid generated for Case 1.

5.1.2 Simulation Setup

In this section, the simulation setup used is briefly described. The FVM is used and discretized using JST scheme. The time steps chosen for Case 1 and 2 are $\Delta t = 0.01675$ CTU and $\Delta t = 0.10417$ CTU, respectively. CTU is the convective time unit defined as $CTU = t \cdot U_\infty / c$.

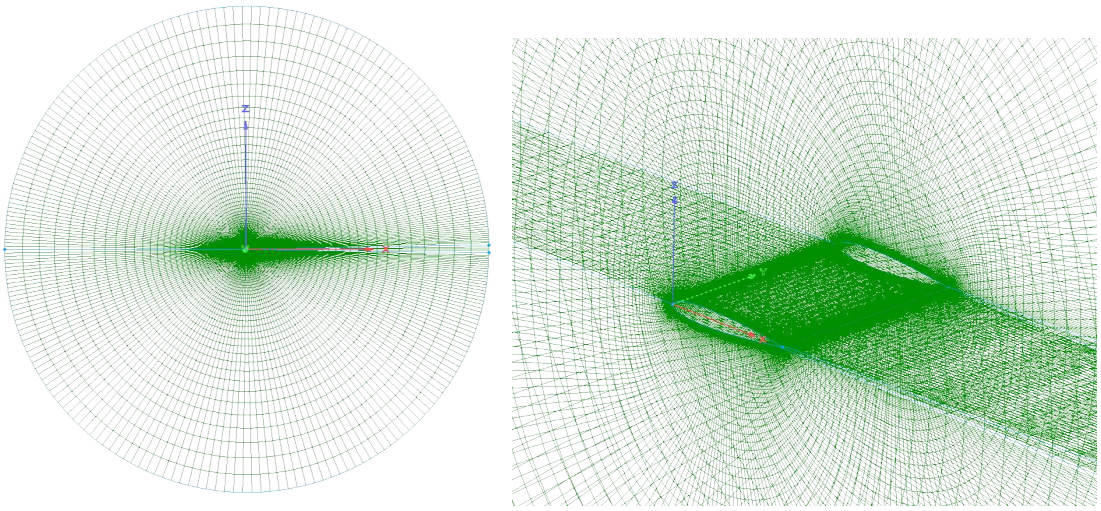

(a) (b)

Figure 5.1: O-mesh of NACA0012 airfoil.

5.2 Flow Field Results

In this section, the results of the flow simulation are presented. These plots illustrate key flow features. Some of the flow results that will be discussed include the flow field vorticity, the pressure coefficient, and the boundary layer. Figures 5.2 and 5.3 show the history of lift and drag coefficients. The window chosen for those graphs shows the CTUs chosen for the analysis of the simulations.

In Figures 5.2 and 5.3, the histories of the lift and drag coefficients are plotted after the initial transience. The selected windows for both graphs correspond to the duration considered for the analysis. These durations were used to calculate the time averaging for the pressure, boundary layer analysis, and acoustic analysis. The average lift coefficient is about 0.7 for both figures. The average lift coefficient is approximately 0.7 in both figures, which is close to the values reported by Mayer [34] and Raus et al. [46], at 0.7 and 0.75, respectively.

Figure 5.4 plots the contours of non-dimensional spanwise vorticity ($\omega_y c/U_\infty$) for Case 1. These figures display the flow evolution captured at different time instances. As the airfoil approaches the light-stall, it experiences periodic vortex shedding in the wake region. The flow starts separating from the surface, creating alternating vorticity regions at the leading and trailing edges. This is stronger at higher angles of attack. The color map indicates the strength of the spanwise vorticity, with red representing the strong positive vorticity and blue representing the strong negative vorticity. In Figure 5.4d, the shear layer visibly rolls up at the trailing and leading edges. Similarly, in Figure 5.5 the vorticity fields are presented for Case 2. Like vorticity plots for Case 1, the alternating regions of positive and negative vorticity in the wake behind the airfoil are an indication of vortex shedding. In Case 2, the vortex formation and shedding process are expected to form much quicker given the increased free-stream velocity

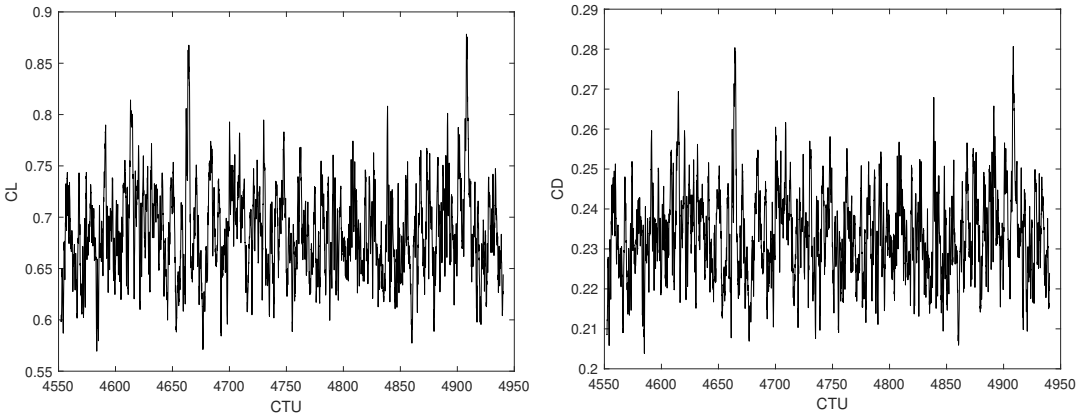

(a) Lift coefficient (C_L) (b) Drag coefficient (C_D)

Figure 5.2: Hsitory of the lift and drag coefficients for Case 1.

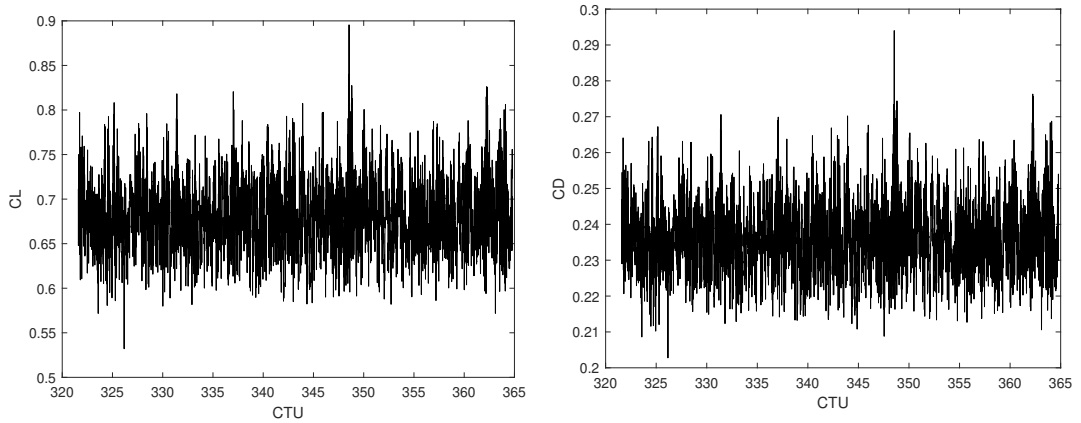

(a) Lift coefficient (C_L) (b) Drag coefficient (C_D)

Figure 5.3: Hsitory of the lift and drag coefficients for Case 2.

and reduced chord length. The scale of the vortices is also reduced due to the smaller chord length.

Figure 5.6 displays the time-averaged pressure coefficient distributions from the DDES simulation compared with the experimental data. In both cases, the pressure coefficient follows the general trend of the experimental data. It is also noticeable that the flow has separated from the leading edge, causing a stall. This occurs due to the burst of a separation bubble caused by a large adverse pressure gradient. In Case 1, it is noticeable that there is a clear discrepancy between the simulation and experiments. However, in Mayer [34] it is reported that the experiments have an offset of about $\Delta C_p = 0.12$ for angles of attack higher than 7.25° when compared to pressure distribution calculated by XFOIL [12]. The pressure distribution obtained in this simulation has an offset of about $\Delta C_p = 0.15$.

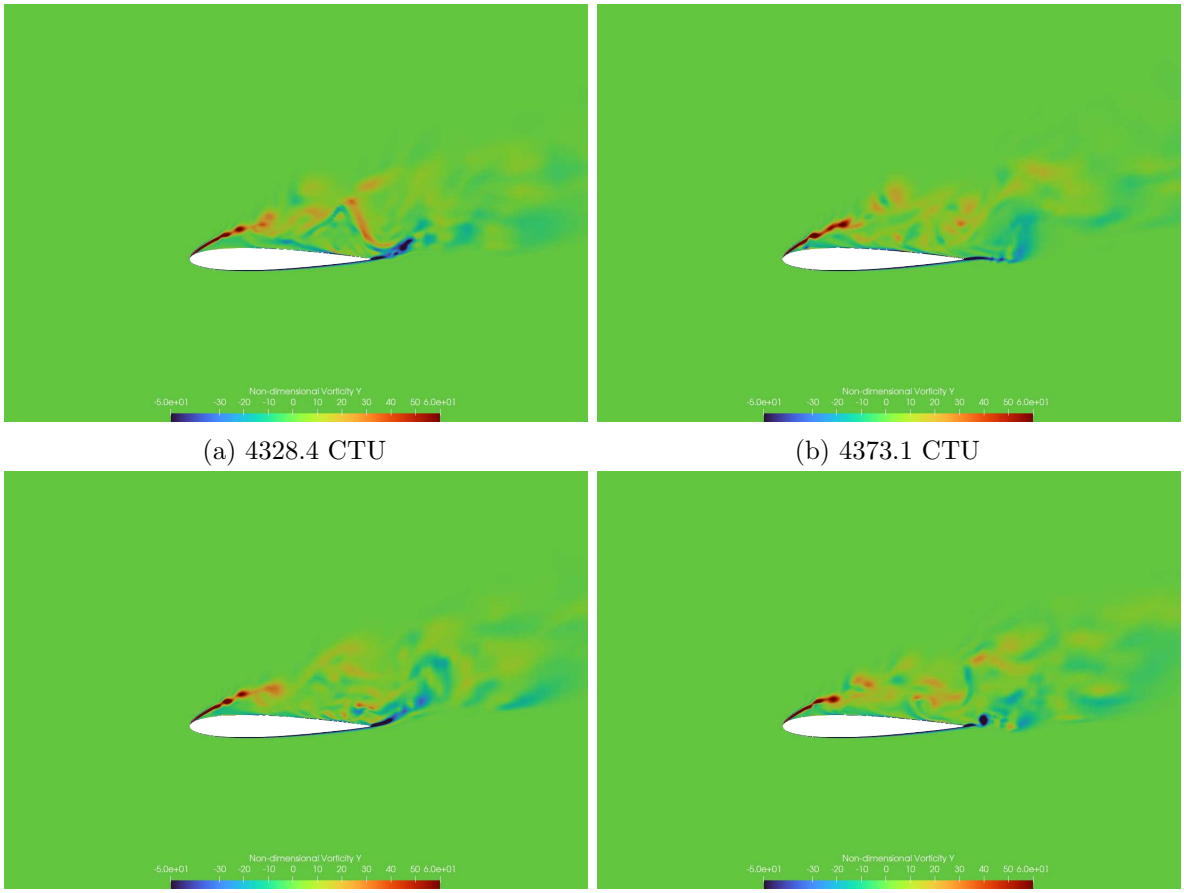

(a) 4328.4 CTU (b) 4373.1 CTU

(c) 4417.9 CTU (d) 4477.6 CTU

Figure 5.4: Non-dimensional vorticity for Case 1.

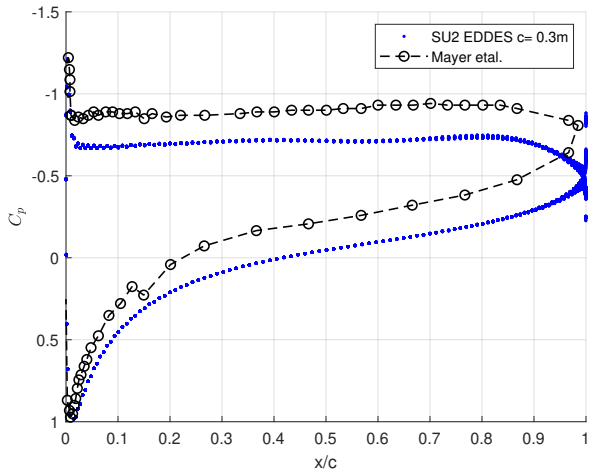

Figure 5.6: Pressure coefficient of the simulation compared to experiments for Case 1.

In Figures 5.7, the mean boundary layer profile of the mean velocity, U/U_e, from the DDES simulation for Case 1 is compared to the experimental data at two different locations on the

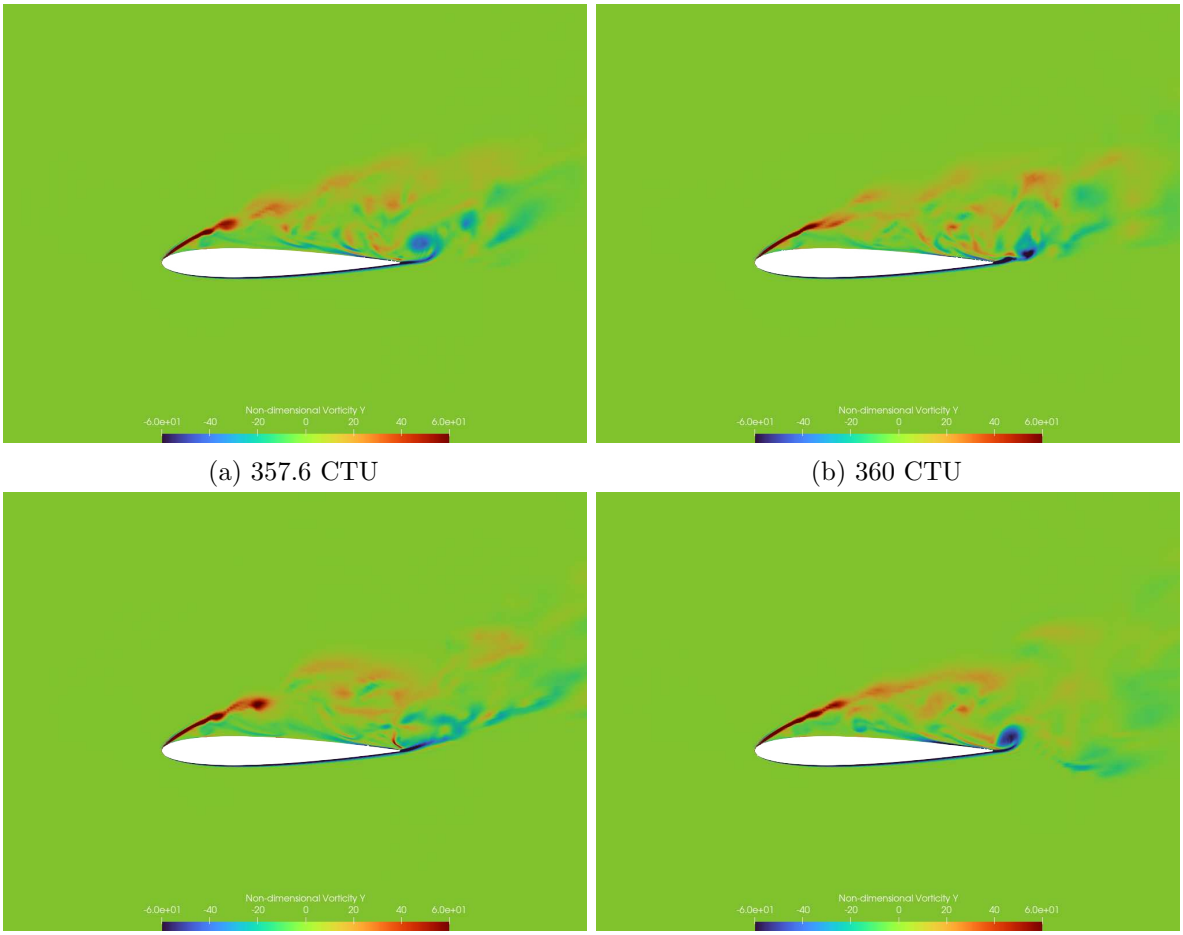

(a) 357.6 CTU (b) 360 CTU

(c) 362.4 CTU (d) 364.8 CTU

Figure 5.5: Non-dimensional vorticity for Case 2.

airfoil, namely $x/c = 0.93$ and $x/c = 0.98$. The reverse flow is indicated by the region where $U/U_e < 0$, which is characteristic of separated flows. In the experiments, the boundary layer profiles of the mean velocity have been measured using a single hot-wire probe at different locations in the wall-normal direction, z_n, on the airfoil suction side [34]. The downside of using stationary hot-wires is the inability to capture reverse flow, using such a method would result in distorted profiles. The distortion in the experimental data is observed in the figure when compared to the simulation results that follow the conventional shape. For comparison, the absolute value of reverse flow has been plotted in a dashed blue line to imitate the results of the hot-wire probe. Considering the solution obtained outside the reversed flow region, it closely matches the experimental data captured.

At $x/c = 0.93$ the mean velocity profile continually increases until it reaches a local maximum of about $z_n/c = 0.13$, the mean velocity then reaches a local minimum of $z_n/c = 0.17$. The mean velocity then continues to increase until it reaches the local free-stream velocity at $z_n/c = 0.42$. Similarly, at $x/c = 0.98$, the mean velocity reaches a local maximum at $z_n/c = 0.14$, and it

continues to increase till $z_n/c = 0.19$ where it reaches a local minimum. The mean velocity then reaches the local free-stream velocity at $z_n/c = 0.44$. The local minimum is an indicator of the reverse flow extent and the location of the local free-stream velocity, U/U_e approaching 1, indicates the boundary layer thickness. These values are consistent between the simulations and the experimental data.

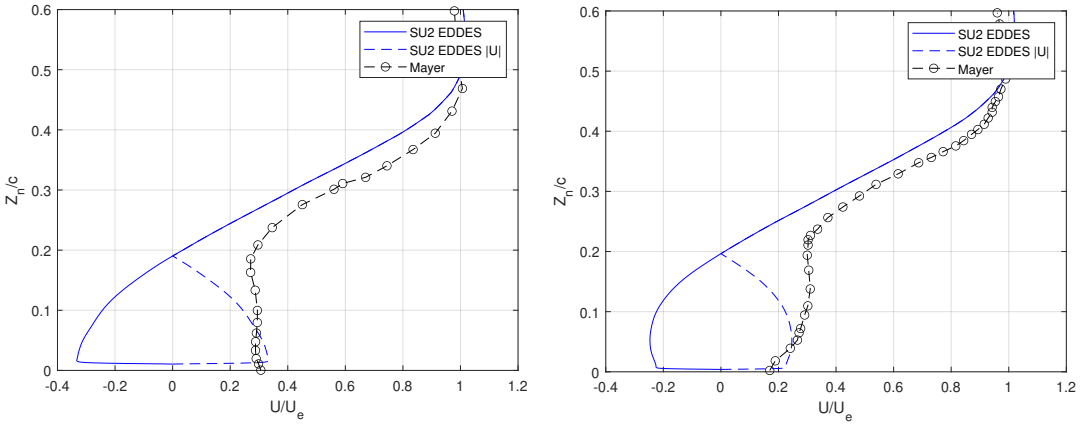

(a) $x/c = 0.93$ (b) $x/c = 0.98$

Figure 5.7: Boundary layer profiles of the mean velocity in the post-stall regime ($\alpha = 15°$).

Figure 5.8, displays the calculated boundary layer thickness based on the velocity field at different locations on the airfoil. The results obtained match well with the trend from the experiments, with a slight overprediction. The experimental and simulated boundary layer thickness increases steadily towards the trailing edge. This occurrence is expected due to the free shear layer expanding from the leading edge.

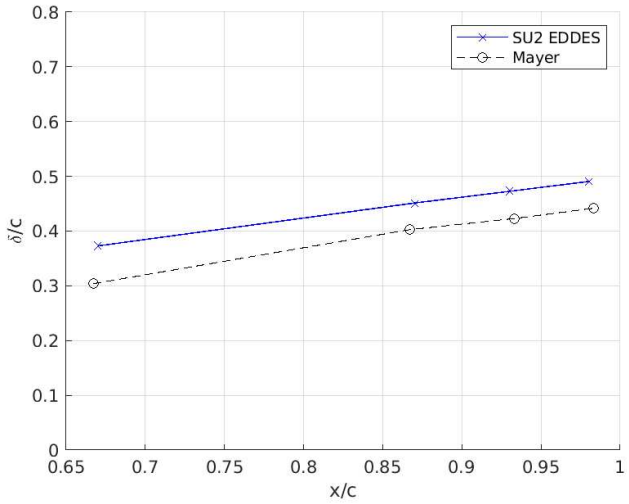

Figure 5.8: Boundary layer thickness

5.3 Acoustic Field Results

The acoustic analysis shown in this section has been implemented for a fixed solid Ffowcs William-Hawkings (FW-H) surface explained in Section 4.3. In this section, the OASPL, the SPL directivity, and the SPL at far-field will be analyzed for the 2 simulated cases. The difference in Mach numbers between Cases 1 and 2 will expectedly result in different acoustic behavior despite having the same Reynolds number. The results of these simulations are then compared to the corresponding experimental results from Mayer [34] and Raus et al. [46]. The far-field acoustic experimental results for Mayer [34] were obtained for observers located at a distance of $r/c = 5.8$, and $r/c = 16.6$ for Raus et al. [46]. The acoustic far-field results obtained from the simulations were calculated at the respective observer locations.

The OASPL plot describes the noise signal power. In Figure 5.9, the OASPL results at the respective observer locations for each case are shown. The θ in this plot represents the azimuthal angle, defined relative to the x-axis. The pattern of the directivity resembles a dipole and becomes more distinct when the observers are located further away from the airfoil. Both, Case 1 and Case 2 have a directional bias at $\theta = 90$. At that location, the noise signal for Case 1 is approximately 57.6 dB and 56.1 for Case 2. The OASPL values for both cases are similar despite the different observer locations, primarily due to the difference in Mach numbers. Generally, as the observer distance increases, the sound levels decrease. However, in Case 2, the significantly higher Mach number results in higher sound levels.

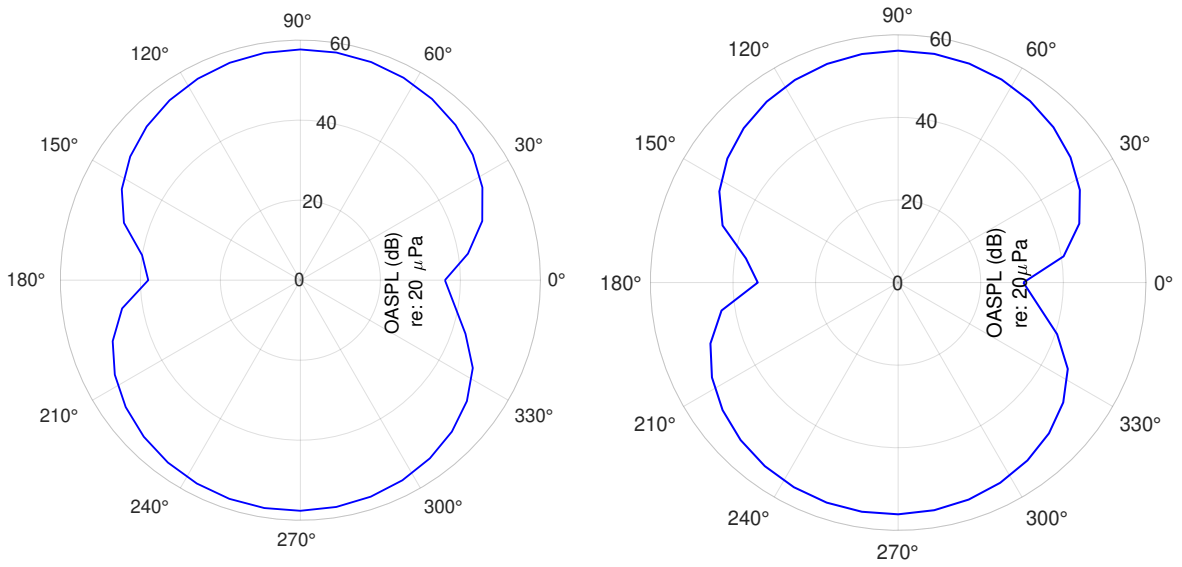

(a) Case 1 at $r/c = 5.8$ (b) Case 2 at $r/c = 16.6$

Figure 5.9: OASPL

The SPL spectrum has been plotted for both simulated cases at the far-field and compared to experimental values in Figure 5.10. The SPL for Case 1 was calculated in the mid-span

plane, at a distance of $r/c = 5.8$ away from the airfoil's trailing edge on the suction side. For Case 2 the SPL was calculated in the mid-span plane, at a distance of $r/c = 16.6$ away from the airfoil's center-chord on the pressure side. Moreau et al. [38] have observed airfoils at the light-stall exhibit a broadband noise signature between Strouhal numbers 0.5 and 8 rather than tonal noise. For Case 1 at $r/c = 5.8$, the results are close to experimental results at Strouhal number of 3, then deviate further for higher frequencies. The measurements for lower frequencies were not available, thus comparison for this range was impossible. Additionally, no peaks were observed from the experimental data. The results, however, do exhibit the features mentioned by Moreau et al. [38] for Strouhal numbers between 4 and 20. The SPL results for Case 2 at $r/c = 16.6$ show distinct discrepancies when compared to the experiments. Nevertheless, the SPL trend for Case 2 closely resembles the experiments with a peak at Strouhal number of 0.5.

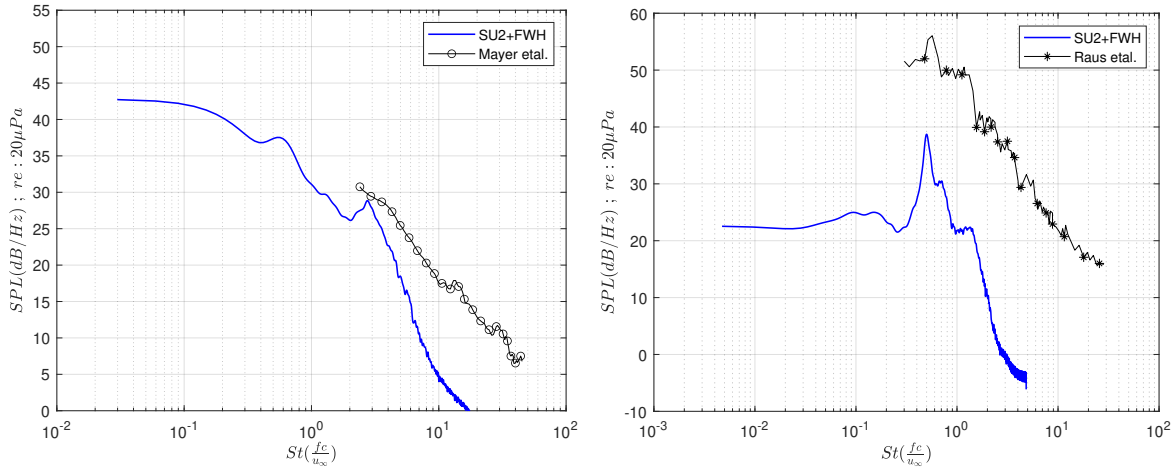

(a) Far-field SPL for Case 1

(b) Far-field SPL for Case 2

Figure 5.10: SPL at far-field for the simulated cases

To compare the results from Cases 1 and 2, the far-field observer needs to be at the same location relative to the airfoil. Figure 5.11a shows the far-field SPL for Cases 1 and 2. The observer is located $r/c = 5.8$ above the trailing edge. The acoustic data were normalized using a scale introduced by Moreau et al. [38]. The PSD is divided by $U_0^5\zeta^2$ where U_0 is the flow speed and ζ is the ratio of chord lengths, this is taken to be the ratio between the span length and the chord length. This scale assumes that acoustic intensity is proportional to the square of the chord and spanwise lengths. The spectral trend is expected to be consistent for equivalent angles of attack. A difference of about 30 dB can be observed between the normalized data between Cases 1 and 2. Using the normalized scale and having the observers at the same location, the data was expected to overlap. This is another indication that some error is present in the far-field SPL spectra in Case 2. Figure 5.11b compares the experimental measurements to provide better insight. It should be noted, however, that these measurements were taken at different observer locations. Mayer [34] at $r/c = 5.8$ above the trailing edge and Raus et

al. [46] is at $r/c = 16.6$ below the mid-chord section of the airfoil. The differences in these measurements are expected due to the varying observer locations.

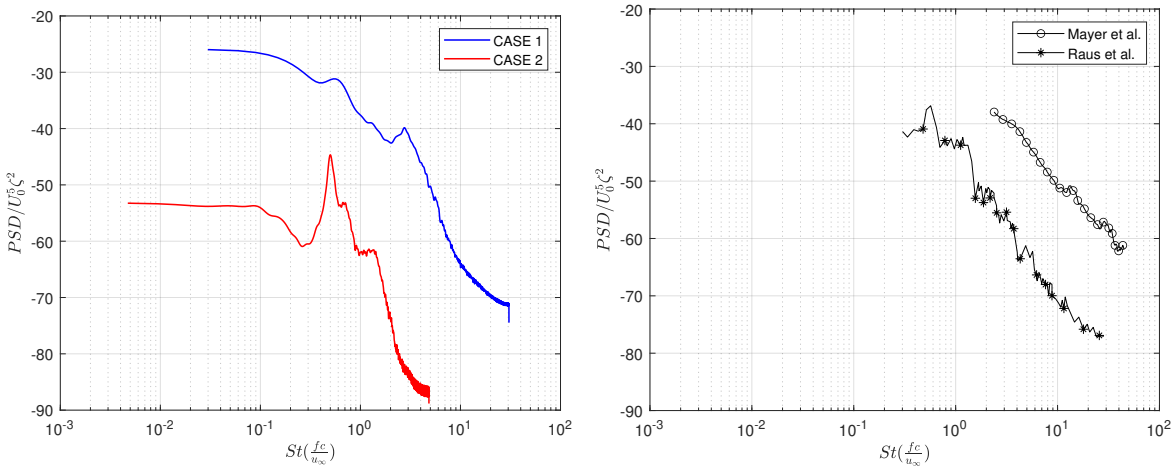

(a) For both cases at the same observer locations (b) For experiments at different observer locations

Figure 5.11: Comparison for normalized SPL at far-field

To further examine the discrepancies shown in Figure 5.10b, the PSD of the surface pressure fluctuations for both Cases, shown in Figure 5.12, were analyzed. The surface PSD for Case 1 was obtained at $x/c = 0.90$ on the airfoil surface and $x/c = 0.92$ for Case 2. The locations differ for each case because experimental data is only available at these specific points. In the surface PSD, there were inconsistencies still present between the simulation results, where the difference for Case 2 is much larger. Directivity plots are shown in Figure 5.13 for the peaks observed in the far-field SPL results, $St = 0.596$ for Case 1 and $St = 0.505$ for Case 2. These plots resemble dipoles and are symmetric in the top and bottom planes, which are quite similar to the OASPL plots with lower noise levels.

The next step taken in investigating the discrepancies in the surface pressure fluctuations was to examine the Reynolds stress. Reynolds stress is defined to represent turbulence and is caused by velocity fluctuations in different directions. In turbulent flows, the velocity at any point fluctuates around a mean value, leading to extra momentum transfer within the flow. Analyzing the Reynolds stress can help determine whether the DDES turbulence model effectively captured the separation and reattachment along the airfoil's suction side near the trailing edge. Chen et al. [7] conducted a similar analysis. In the study, two DDES simulations were made for the chord-based Reynolds number of $Re_c = 2 \times 10^5$ and $Re_c = 5 \times 10^5$. Using the FW-H framework, the simulation with $Re_c = 5 \times 10^5$ has shown inaccurate noise predictions. The Reynolds stress was examined along the normal distance from the airfoil surface for different points, shown in Figure 5.14 for both simulations. The simulation with $Re_c = 2 \times 10^5$, which has shown accurate far-field noise prediction, has a more uniform Reynolds stress distribution along the trailing edge. However, in the other simulation, it was observed that the Reynolds stress

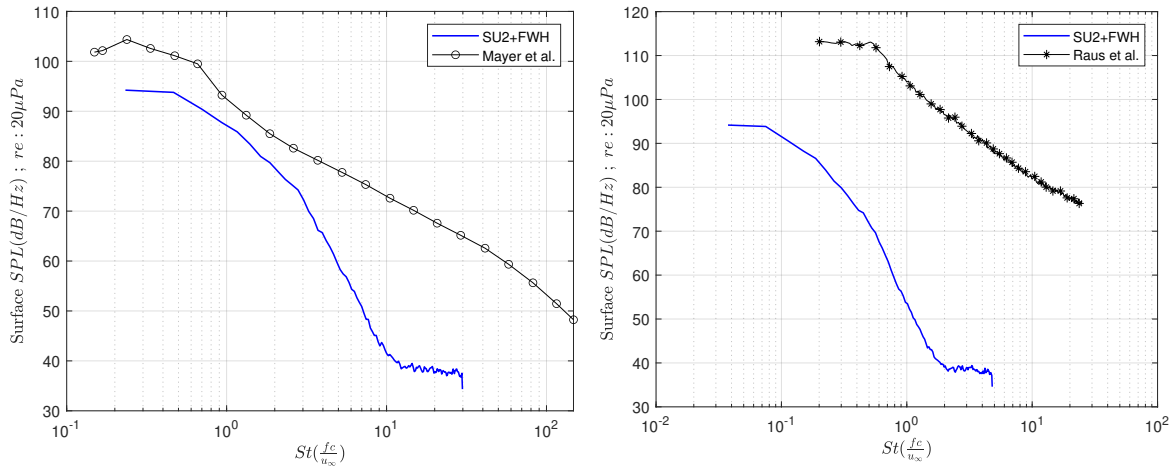

(a) Case 1 at $x/c = 0.90$ (b) Case 2 at $x/c = 0.92$

Figure 5.12: Surface pressure fluctuation PSD for the simulated cases

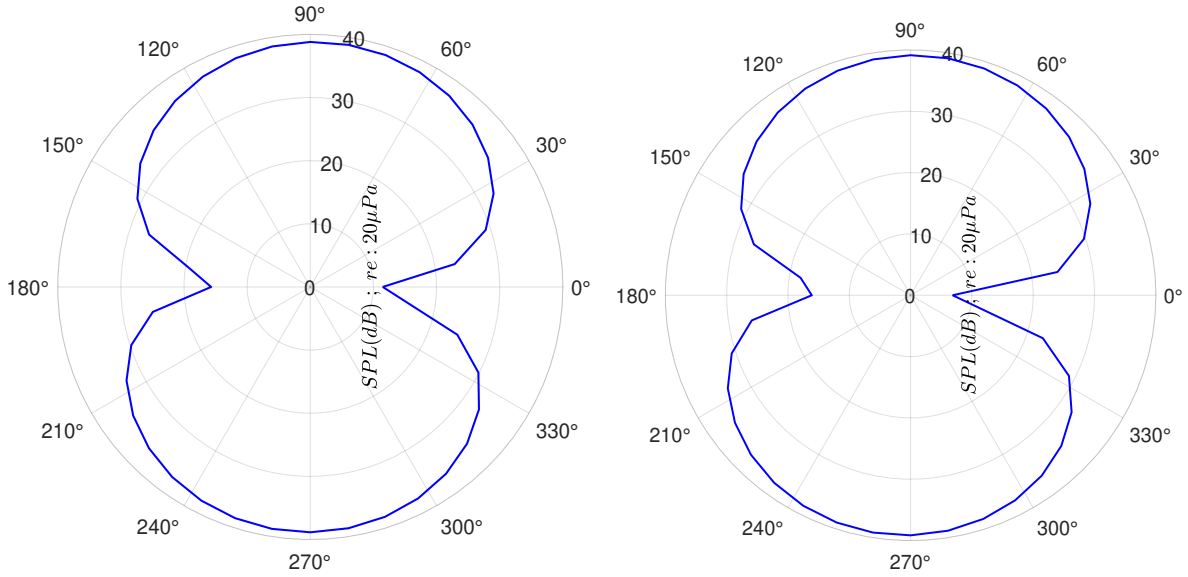

(a) Case 1, St = 0.596 (b) Case 2, St = 0.505

Figure 5.13: Directivity

distribution was very chaotic without a clear trend along the flow or normal directions. It was deduced that the Reynolds stress results for the case of $Re_c = 5 \times 10^5$ have been inaccurately captured.

Similarly, this analysis was made for Cases 1 and 2 of this study. Figure 5.15 shows the Reynolds stress distribution ($\overline{u'w'}$) along the normal distance from the airfoil surface at different points. It is observed that the Reynolds stress in Case 2 is six times greater in magnitude, however, the distribution seems to be consistent for both cases unlike what was observed in Chen et al. [7]. This indicates that the discrepancies observed in the acoustic data for Case 2

are not caused by any limitations in DDES performance.

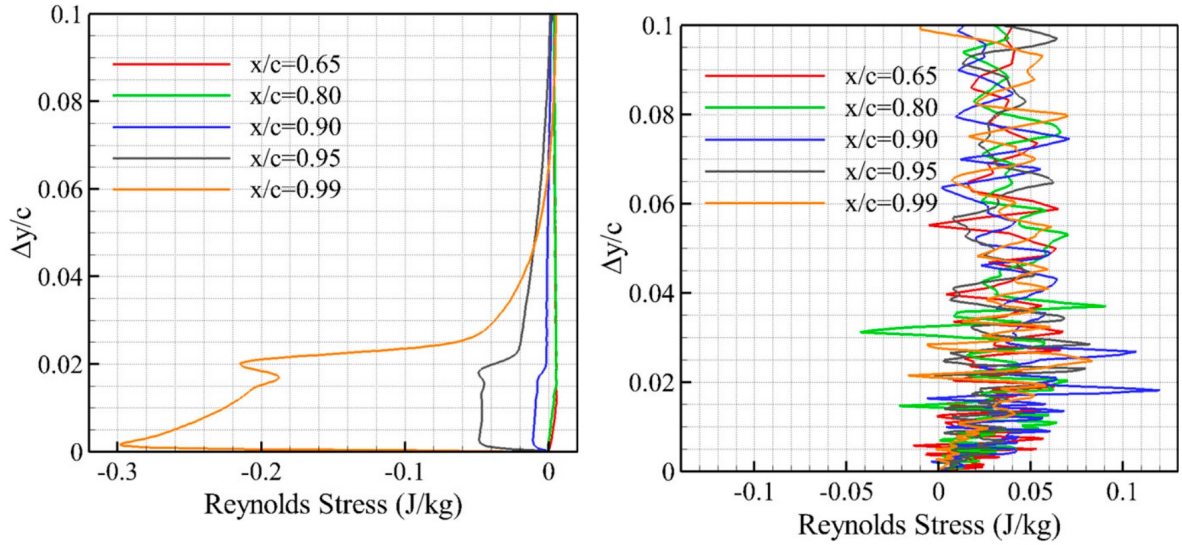

(a) $Re_c = 2 \times 10^5$, U= 20 m/s (b) $Re_c = 5 \times 10^5$, U= 50 m/s

Figure 5.14: Reynolds stress in the boundary layer suction side in Chen et al. [7].

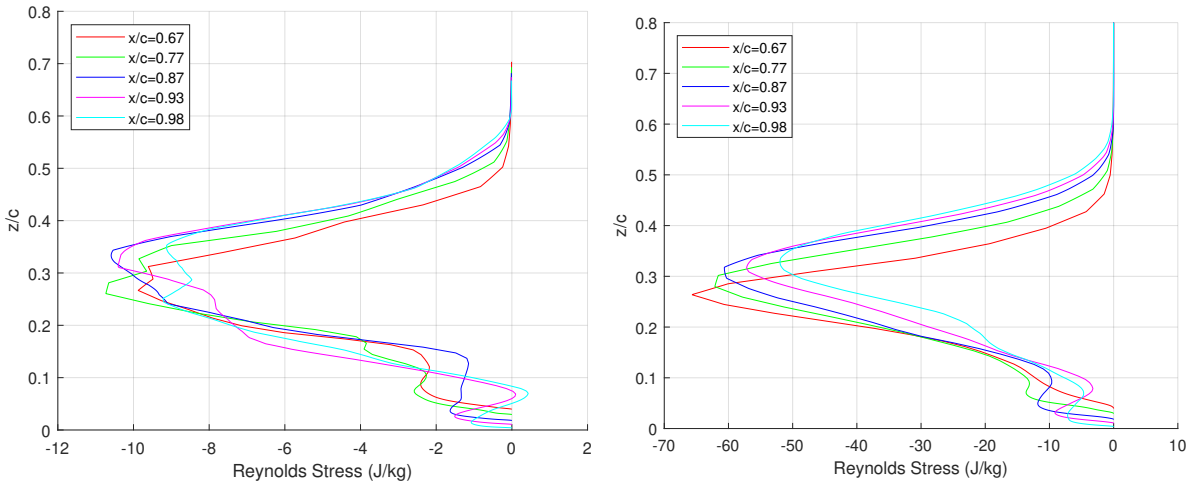

(a) Case 1 (b) Case 2

Figure 5.15: Distribution of $\overline{u'w'}$ Reynolds Stress in the boundary layer suction side

Upon revisiting the chosen parameters and mesh configuration, it was determined that the discrepancies observed in the surface pressure fluctuation PSD and far-field noise spectra in Case 2 were likely due to an inadequate time step. The consequences of choosing an inadequate time step can lead to an insufficient temporal resolution where the unsteady characteristics of the flow cannot be accurately captured. This limitation in time step resolution led to an underrepresentation of the flow's dynamic behavior, causing deviations between the simulated

results and expected outcomes. Consequently, it was concluded that a finer time step would be necessary to improve the fidelity of the surface pressure and far-field acoustic data in Case 2.

5.4 Spanwise Correction NACA0012

The spanwise correction extends the sound source's flow properties beyond the computational domain to estimate the noise generated across the entire span length. Spanwise correction is beneficial in predicting the noise generated for an entire span of an airfoil by simulating a small section. However, as no experimental data was available for a longer span with similar parameters, the simulation conducted for Cases 1 and 2 was used to test the validity of this correction.

In this analysis, a spanwise correction for the entire span length is L, and the corrected section is L_s. This correction has been performed for two cases, $N = 5$ and $N = 3$, where N represents the number of sections into which the span length is divided. For clarification, Figure 5.16 shows the airfoil in the case where the span is divided into five subsections. The geometry of the airfoil in Case 1 was cut down to the length $L_s = L/N$, this section was chosen to be the corrected section. The corrected section was not chosen to be on either end of the airfoil to circumvent the boundary effects. To obtain the PSD acoustic pressure emitted from each subsection, the cut-down section is used to resemble each subsection along the entire span. Then, an observer file is generated for each subsection where the location of the observer is relative to the cut-down section. The spanwise correction script is then used by following the steps discussed in Section 4.5.2. Similarly, the same steps were taken for the case with subsections $N = 3$.

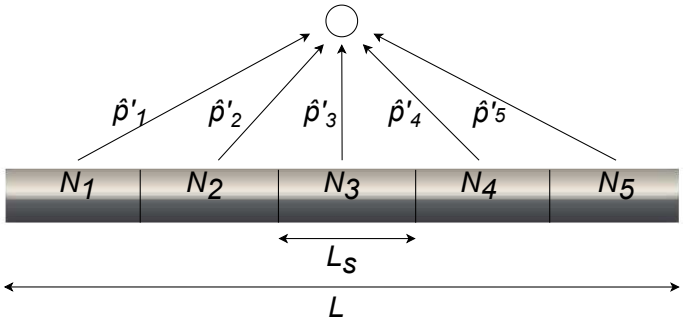

Figure 5.16: Airfoil front-view schematic of span division for $N = 5$.

In Figure 5.17, the far-field SPL results for Case 1 are plotted in blue, the SPL for the cut-down section is plotted in red, and the SPL for the spanwise correction applied to the cut-down section is presented in red dashed lines. Figure 5.17a shows the correction made for $N = 5$, and Figure 5.17b shows the corrections for $N = 3$. The correction seems to be more accurate for the case of $N = 3$, this is expected as less span length needs to be corrected for.

This behavior was prominent in a study by Aihara et al. [1], where the spanwise correction was found to be more accurate when the span length was divided into fewer sections (longer sections) compared to more sections (smaller sections). For both cases, the correction is least precise for Strouhal numbers in the range of 0.03 to 0.2, and 1 to 4 with a maximum difference of 3 dB while maintaining the same trend. For the lower range, the corrected SPL seems to be lower than the SPL of the entire span, whereas it overshoots in the higher range.

In Figure 5.18, the spanwise correction has been applied to Case 2 with the span length divided into 3 sections. Similar to Case 1, the spanwise correction falls about 2 dB behind for Strouhal numbers ranging from 0.005 to 0.03, and overshoots at a maximum of 3 dB for the range of 0.08 to 0.2. In a study by Orselli et al. [42], this proposed spanwise correction was used on a circular cylinder. Some discrepancies in the correction at lower and higher frequencies were also noted by Aihara et al. [1] and Orselli et al. [42].

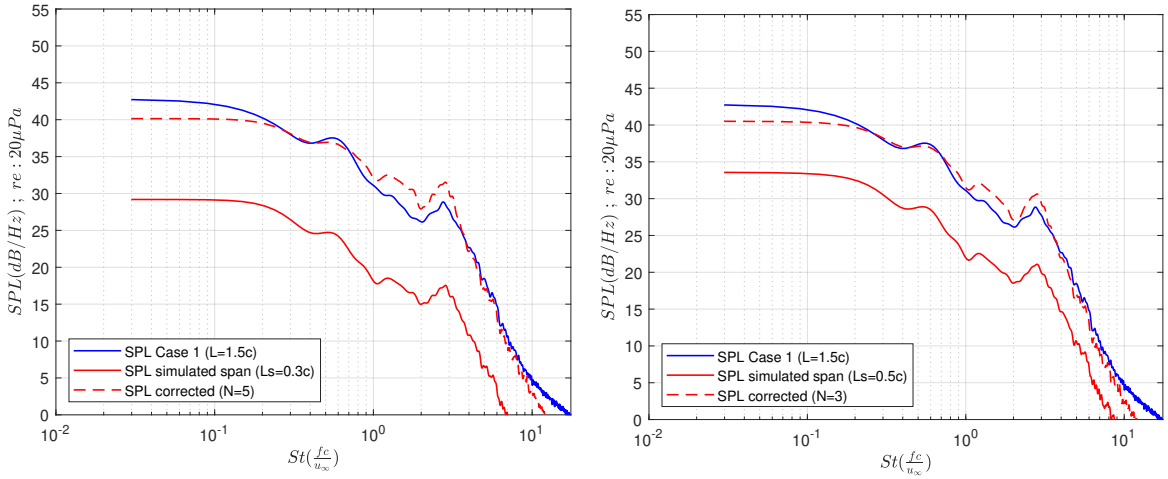

(a) SPL corrected for 5 subsections

(b) SPL corrected for 3 subsections

Figure 5.17: Corrected SPL at far-field for Case 1

In Figure 5.19, the coherence length L_c is normalized with the simulated span length L_s and the corrected SPL as a function of the Strouhal number for Case 1 and 2 when $N = 3$. For both cases, it is observed that the correction is at a maximum of 9.54 dB when L_c/L_s is greater than 1.69 and is at a minimum of 4.77 dB when L_c/L_s is less than 0.56. The SPL correction and the coherence length significantly drop to a minimum from Strouhal number equal to 13 for Case 1 and Strouhal number equal to 3 for Case 2. Aihara et al. [1] observed that at the vortex shedding frequency, the coherence length is much larger than the simulated span length. This frequency is where the main tonal peak occurs, and is related to the vortex shedding in the wake. The coherence length is smaller than $L_s/\sqrt{\pi}$ for most frequencies apart from the vortex shedding frequency, which results in adding the correction $10log(L/L_s) = 4.77$. This shows that having a precise value for those frequencies is not crucial. Seo et al. [52] also concluded that just having a reasonable approximation of the coherence length should be sufficient. Despite

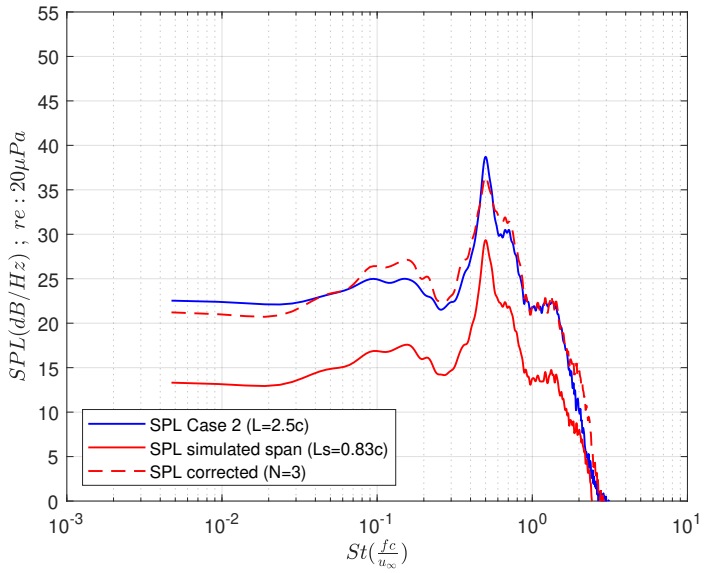

Figure 5.18: Corrected SPL at far-field for Case 2

minor discrepancies in the spanwise correction, it offers reliable and accurate SPL results for an airfoil with a long span.

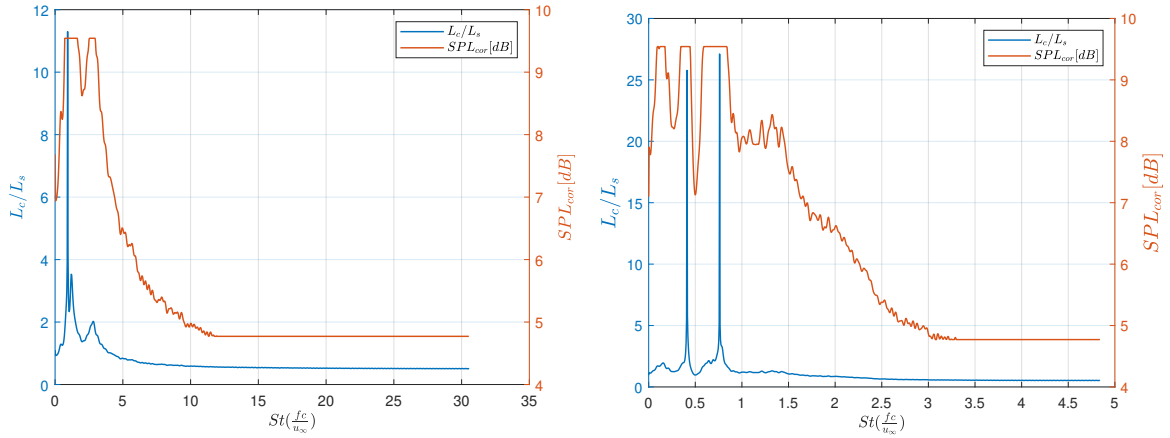

(a) Case 1

(b) Case 2

Figure 5.19: Normalized spanwise coherence length and the SPL correction as a function of St for $N = 3$.

Chapter 6

Conclusion and Recommendations

6.1 Conclusion

This study aimed to develop and validate a reliable CFD-CAA framework combining Delayed DDES with the FW-H analogy to predict far-field noise generated by light-stall conditions on a NACA 0012 airfoil. The research objectives laid out in Chapter 3 were pursued through two test cases, and the key findings are summarized below.

In Case 1, the airfoil was analyzed at a lower Mach number but the same Reynolds number as in Test Case 2. The results showed good agreement with experimental data, particularly in surface pressure fluctuations and far-field noise spectra. This alignment demonstrated the framework's capability to reliably capture the flow physics and predict the acoustic signature under these conditions

In Case 2, a higher Mach number and a different set of observer locations were used. Discrepancies were observed between the simulation results and experimental data, particularly in the far-field noise spectra. To investigate these differences, detailed checks were conducted, including an analysis of surface pressure fluctuations and Reynolds stress distributions. These analyses revealed that inadequate time step resolution likely contributed to the observed discrepancies, emphasizing the importance of proper temporal resolution in capturing unsteady flow phenomena.

In addition, a spanwise correction was investigated to address the challenge of simulating smaller spanwise domains. This correction method effectively scaled the acoustic pressure distribution along the span, leading to improved noise predictions. The results from this investigation showed excellent agreement with expected outcomes, confirming the effectiveness of the spanwise correction in reducing computational costs while maintaining accuracy.

Overall, the DDES and FW-H framework proved effective in Case 1, with results that closely matched experimental observations. In Case 2, although discrepancies were noted, they were linked to specific simulation parameters such as time step resolution. Additionally, the spanwise correction method was validated as a valuable tool for enhancing noise prediction accuracy

without the need for extensive computational domains.

6.2 Recommendations

- The discrepancies observed in the far-field noise predictions, particularly the underestimations of the acoustic sound levels, suggest further refinement of the time step resolution. Future work should explore the effects of choosing a more appropriate time step to prove the efficiency of the DDES and FW-H framework.

- The current study utilized DDES for turbulence modeling; however, exploring the performance of other models, such as Wall-Modeled Large Eddy Simulation (WMLES), could provide valuable insights. Testing different turbulence models coupled with the FW-H would help determine their effectiveness in capturing key flow features and acoustic phenomena, potentially improving the accuracy of noise predictions for various flow conditions.

- While the current study focused on the NACA0012 airfoil under light stall conditions, the availability of comprehensive acoustic data for validation remains limited. Future studies should include test cases where reliable experimental acoustic data is available, enabling more robust validation of the far-field noise predictions and enhancing confidence in the simulation results.

- While this study focused on specific stall conditions and airfoil geometry, future work could expand the methodology to other airfoil shapes and flow regimes. This would provide a broader validation of the CFD-CAA framework and its applicability to various aerodynamic noise prediction scenarios.

Bibliography

[1] A. Aihara, A. Goude, and H. Bernhoff, *Numerical prediction of noise generated from airfoil in stall using les and acoustic analogy*, Noise Vibration Worldwide, 52 (2021), pp. 295–305.

[2] R. Amiet, *Acoustic radiation from an airfoil in a turbulent stream*, Journal of Sound and Vibration, 41 (1975), pp. 407–420.

[3] D. Aylor, *Noise reduction by vegetation and ground*, Journal of the Acoustical Society of America, 51, p. 197.

[4] K. Brentner and F. Farassat, *Modeling aerodynamically generated sound of helicopter rotors*, Progress in Aerospace Sciences, (2003), pp. 83–120.

[5] T. Brooks, S. Pope, and M. Marcolini, *Airfoil self-noise and prediction*, (1989).

[6] D. Casalino, *An advanced time approach for acoustic analogy predictions*, Journal of Sound and Vibration, (2003), pp. 583–612.

[7] N. Chen, H. Liu, Q. Liu, X. Zhao, and Y. Wang, *Effects and mechanisms of les and ddes method on airfoil self-noise prediction at low to moderate reynolds numbers*, AIP Advances, 11 (2021).

[8] T. Colonius and S. Lele, *Computational aeroacoustics: progress on nonlinear problems of sound generation*, Progress in Aerospace Sciences, 40 (2004), pp. 345–416.

[9] S. Deck, *Recent improvements in the zonal detached eddy simulation (zdes) formulation*, Theoretical Computational Fluid Dynamics, (2012), pp. 523–550.

[10] G. DeSena, *Pressure distribution on an airfoil*, (2012).

[11] P. Drazin, *Kelvin–helmholtz instability*, Encyclopedia of Atmospheric Sciences, (2003), pp. 1068–1072.

[12] M. Drela, *XFOIL: An Analysis and Design System for Low Reynolds Number Airfoils*, (1989), pp. 1–12.

[13] T. Economon, F. Palacios, S. Copeland, T. Lukaczyk, and J. Alonso, *Su2: An open-source suite for multiphysics simulation and design*, AIAA, 54 (2016).

[14] X. Fang and Z. Wang, *Onthelow-frequency flapping motion in flow separation*, Fluid Mechanics, 984 (2024).

[15] F. Farassat, *Linear acoustic formulas for calculation of rotating blade noise*, AIAA Journal, 19 (1981), pp. 1122–1130.

[16] ——, *Derivation of formulations 1 and 1a of farassat*, (2007).

[17] A. Faria, J. Saab, S. Rodriguez, and M. Pimenta, *Discussion on turbulent inflow noise prediction*, Artigo Brazil Wind Power, 04 (2022).

[18] S. Glegg and W. Devenport, *Aeroacoustics of Low Mach Number Flows*, Elsevier, 2017.

[19] O. Guasch, A. Pont, J. Baiges, and R. Codina, *Finite element hybrid and direct computational aeroacoustics at low mach numbers in slow time-dependent domains*, Computers and Fluids, 239 (2022).

[20] C. Harris, *Absorption of sound in air versus humidity and temperature*, Journal of the Acoustical Society of America, 40 (1966), p. 148.

[21] A. Henderson, *A parallel visualization application*, ParaView Guide, (2007).

[22] A. Horn, *Sound source behavior: Near field, transition, and far field.*

[23] A. Jameson, W. Schmidt, and E. Turkel, *Numerical solution of the euler equations by finite volume methods using runge-kutta time stepping schemes*, AIAA Paper, (1981), pp. 1981–1259.

[24] C. Kato, A. Iida, Y. Takano, H. Fujita, and M. Ikegawa, *Numerical prediction of aerodynamic noise radiated from low mach number turbulent wake*, 31st Aerospace Sciences Meeting, (1993).

[25] G. Lacagnina, P. Chaitanya, T. Berk, J. Kim, P. Joseph, B. Ganapathisubramani, S. Hasheminejad, T. Chong, O. Stalnov, M. Shahab, M. Omidyeganeh, and A. Pinelli, *Mechanisms of airfoil noise near stall conditions*, Physical Review Fluids, 4 (2019).

[26] S. Lee, L. Ayton, F. Bertagnolio, S. Moreu, T. Chong, and P. Joseph, *Turbulent boundary layer trailing-edge noise: Theory, computation, experiment, and application*, Progress in Aerospace Sciences, 126 (2021).

[27] J. Leishman, *Introduction to Aerospace Flight Vehicles*, Embry-Riddle Aeronautical University, 2022.

[28] G. Leloudas, W. Zhu, J. Sørensen, W. Shen, and S. Hjort, *Prediction and reduction of noise from a 2.3 mw wind turbine*, Physics Conference Series, 75 (2007).

[29] A. Lidtke, *Predicting radiated noise of marine propellers using acoustic analogies and hybrid eulerian-lagrangian cavitation models*, 2017.

[30] M. Lighthill, *On sound generated aerodynamically i. general theory*, Proc. R. Soc. Lond. A Math. Phys., 211 (1952), pp. 564–587.

[31] S. Liou and J. Steffen, *A new flux splitting scheme*, Journal of Computational Physics, 107 (1993), pp. 23–39.

[32] W. Liu, *A review on wind turbine noise mechanism and de-noising techniques*, Renewable Energy, (2017).

[33] N. Masmoudi, Y. Wang, D. Wu, and Z. Xhang, *Tollmien-schlichting waves in the subsonic regime*, (2023).

[34] Y. Mayer, *Aeroacoustic characteristics of static and dynamic stall*, (2020).

[35] F. Menter, *Improved two-equation k-omega turbulence models for aerodynamic flows*, 1992.

[36] E. Molina, J. Alonso, B. Zhou, M. Righi, and R. Silva, *Flow and noise predictions around tandem cylinders using ddes approach with su2*, (2019).

[37] E. Molina, C. Spode, R. Silva, D. Manosalvas-Kjono, S. Nimmagadda, T. Economon, J. Alonso, and M. Righi, *Hybrid rans/les calculations in su2*, 23rd AIAA Computational Fluid Dynamics Conference, (2017).

[38] S. Moreau, M. Roger, and J. Christophe, *Flow features and self-noise of airfoils near stall or in stall*, 15th AIAA/CEAS Aeroacoustics Conference, (2009).

[39] P. Moriarty, *Nrel airfoil noise*, (2005).

[40] P. Nataraj, *Airfoil self-noise predictions using ddes and the fwh analogy*, (2022).

[41] G. Naterer, O. Jianu, and M. Rosen, *Noise polution prevention in wind turbines: Status and recent advances*, 2011.

[42] R. Orselli, J. Meneghini, and F. Saltara, *Two and three-dimensional simulation of sound generated by flow around a circular cylinder*, 30th AIAA aeroacoustics conference, (2009).

[43] F. Palacios, M. Colonno, A. Aranake, A. Campos, S. Copeland, T. Economon, A. Lonkar, T. Lukaczyk, T. Taylor, and J. Alonso, *Stanford university unstructured (su2): An open-source integrated computational environment for multi-physics simulation and design.*, 51st AIAA Aerospace Sciences Meeting including the New Horizons Forum and Aerospace Exposition, (2013).

[44] F. Perot, J. Auger, H. Giardi, X. Gloerfelt, and C. Baily, *Numerical prediction of the noise radiated by a cylinder*, 9th AIAA/CEAS Aeroacoustics Conference, (2003).

[45] D. Raus, B. Cotté, R. Monchaux, E. Jondeau, P. Souchotte, and M. Roger, *Experimental study of the dynamic stall noise on an oscillating airfoil*, Journal of Sound and Vibration, 537 (2022).

[46] D. Raus, L. Sicard, B. Cotté, R. Monchaux, E. Jondeau, P. Souchotte, and M. Roger, *Experimental characterization of the noise generated by an airfoil oscillating above stall*, AIAA AVIATION, (2021).

[47] E. Ray, *Modeling sound propagation*, Industrial Noise Series.

[48] P. Roe, *"approximate riemann solvers, parameter vectors, and difference schemes*, Journal of Computational Physics, 43 (1981), pp. 357–372.

[49] s. Burgmann and W. Schröder, *Investigation of the vortex induced unsteadiness of a separation bubble via time-resolved and scanning piv measurements*, Experiments in Fluids, 45 (2008), pp. 675–691.

[50] M. Sanders, *Study on the application of digital mems microphones for aeroacoustic noise source localization for large drones*, 2017.

[51] F. Santos, L. Botero-Bolívar, C. Venner, and L. Santana, *Inflow turbulence distortion for airfoil leading-edge noise prediction for large turbulence length scales for zero-mean loading*, The Journal of the Acoustical Society of America, 153 (2023), pp. 1811–1822.

[52] J. Seo, K. Chang, and Y. Moon, *Aerodynamic noise prediction for long-span bodies*, 12th AIAA/CEAS Aeroacoustics Conference, (2006).

[53] M. Shur, P. Spalart, and A. Travin, *An enhanced version of des with rapid transition from rans to les in separated flows*, 95 (2015), pp. 709–737.

[54] Siemens, *Sound fields: Free versus diffuse field, near versus far field*, 2020.

[55] E. Sorgüven and Y. Dogan, *Acoustic optimization for centrifugal fans*, Noise Control Engineering Journal, 60 (2012), pp. 379–391.

[56] P. R. Spalart, S. Deck, M. L. Shur, K. D. Squires, M. K. Strelets, and A. Travin, *A new version of detached-eddy simulation, resistant to ambiguous grid densities*, Theoretical Computational Fluid Dynamics, 20 (2006), pp. 181–195.

[57] F. Toro, *Riemann solvers and numerical methods for fluid dynamics: A practical introduction*, Springer–Verlag, (1999), pp. 573–580.

[58] B. Truax, *Sound propagation*, HANDBOOK FOR ACOUSTIC ECOLOGY, (1999).

[59] J. M. Tuner and J. W. Kim, *Effect of spanwise domain size on direct numerical simulations of airfoil noise during flow separation and stall*, Physics of Fluids, 32 (2020).

[60] J. Turner and J. Kim, *Aerofoil dipole noise due to flow separation and stall at a low reynolds number*, International Journal of Heat and Fluid Flow, 86 (2020).

[61] P. Welch, *The use of fast fourier transform for the estimation of power spectra: A method based on time averaging over short, modified periodograms*, IEEE Transactions on Audio and Electroacoustics, 15 (1967), pp. 70–73.

[62] J. F. Williams and D. Hawkings, *Sound generation by turbulence and surfaces in arbitrary motion*, Philosophical Transactions of the Royal Society of London. Series A, 264 (1969), pp. 321–342.

[63] W. Wolf and K. Lele, *Trailing-edge noise predictions using compressible large-eddy simulation and acoustic analogy*, AIAA Journal, 50 (2012).

[64] L. Wu, X. Jing, and X. Sun, *Prediction of vortex-shedding noise from the blunt trailing edge of a flat plate*, Journal of Sound and Vibration, 408 (2017), pp. 20–30.

[65] S. Yahya, S. Anwer, and S. Sanghi, *Performance of different sgs models of les for low mach number channel flow*, Procedia Engineering, 38 (2012), pp. 1192–1208.

[66] S. Yarusevych and P. Sullivan, *Coherent structures in an airfoil boundary layer and wake at low reynolds numbers*, Physics of Fuids, 18 (2006).

[67] K. Zaman, D. Mckinzie, and C. Rumsey, *A natural low-frequency oscillation of the flow over an airfoil near stalling conditions*, Fluid Mechanics, 202 (1989), pp. 403–442.

Appendix A

Configuration Files

A.1 CASE 1

```
%%%%%%%%%%%%%%%%%%%%%%%%%%%%%%%%%%%%%%%%%%%%%%%%%%%%%%%%%%%%%%%%%%%%%%%%%%%%%%%%
%                                                                              %
% Stanford University unstructured (SU2) configuration file                    %
% Case description: CASE 1 NACA0012                                            %
% Author: Michael Zaki                                                        %
% Institution:      %
% Date:                                                                        %
% File Version SU2 v5.0                                                        %
%                                                                              %
%%%%%%%%%%%%%%%%%%%%%%%%%%%%%%%%%%%%%%%%%%%%%%%%%%%%%%%%%%%%%%%%%%%%%%%%%%%%%%%%

% ------------- DIRECT, ADJOINT, AND LINEARIZED PROBLEM DEFINITION ------------%
%
% Physical governing equations (POTENTIAL_FLOW, EULER, NAVIER_STOKES,
%                               MULTI_SPECIES_NAVIER_STOKES, TWO_PHASE_FLOW,
%                               COMBUSTION)
SOLVER= RANS
%
% Specify turbulence model (NONE, SA, SA_NEG, SST)
KIND_TURB_MODEL= SA
%
% Specify Hybrid RANS/LES for SA family (NONE, SADES, SADDES)
HYBRID_RANSLES= SA_EDDES
%
% DES Constant (0.65)
```

```
DES_CONST= 0.65
%
% Mathematical problem (DIRECT, ADJOINT, LINEARIZED, ONE_SHOT_ADJOINT)
MATH_PROBLEM= DIRECT
%
% Restart solution (NO, YES)
RESTART_SOL= YES
% Compute the average solution for unsteady simulations (NO, YES)
COMPUTE_AVERAGE= YES
%
% Restart the average process from a previous averaged solution (NO, YES)
%RESTART_AVERAGE= NO
%
% ----------- COMPRESSIBLE AND INCOMPRESSIBLE FREE-STREAM DEFINITION ----------%
%
% Mach number (non-dimensional, based on the free-stream values)
MACH_NUMBER= 0.05795
%
% Angle of attack (degrees)
AOA= 15
%
% Side-slip angle (degrees)
SIDESLIP_ANGLE= 0.0
%
% Free-stream pressure (101325.0 N/m^2 by default, only Euler flows)
%FREESTREAM_PRESSURE= 101325
%
% Free-stream temperature (273.15 K by default)
FREESTREAM_TEMPERATURE= 300
%
% Reynolds number (non-dimensional, based on the free-stream values)
REYNOLDS_NUMBER=  4.10752E5
%
% Reynolds length (1 m, 1 inch by default)
REYNOLDS_LENGTH= 1

% -------------- COMPRESSIBLE AND INCOMPRESSIBLE FLUID CONSTANTS --------------%
%
```

```
% Different gas model (STANDARD_AIR, IDEAL_GAS, VW_GAS, PR_GAS)
FLUID_MODEL= STANDARD_AIR
%
% Ratio of specific heats (1.4 (air), only for compressible flows)
GAMMA_VALUE= 1.4
%
% Specific gas constant (287.87 J/kg*K (air), only for compressible flows)
GAS_CONSTANT= 287.87

% ---------------------- REFERENCE VALUE DEFINITION --------------------------%
%
% Reference origin for moment computation
REF_ORIGIN_MOMENT_X = 0.25
REF_ORIGIN_MOMENT_Y = 0.00
REF_ORIGIN_MOMENT_Z = 0.00
%
% Reference length for pitching, rolling, and yawing non-dimensional moment
REF_LENGTH= 1.0
%
% Reference area for force coefficients (0 implies automatic calculation)
REF_AREA=0
%
% Flow non-dimensionalization (DIMENSIONAL, FREESTREAM_PRESS_EQ_ONE,
%                              FREESTREAM_VEL_EQ_MACH, FREESTREAM_VEL_EQ_ONE)
REF_DIMENSIONALIZATION= DIMENSIONAL
%REF_DIMENSIONALIZATION= FREESTREAM_PRESS_EQ_ONE
%
% ------------------------ TIME-DEPENDENT SIMULATION -----------------------------%
%
% Time domain simulation
TIME_DOMAIN= YES
%TIME_DOMAIN= NO
%
% Unsteady simulation (NO, TIME_STEPPING, DUAL_TIME_STEPPING-1ST_ORDER,
%                      DUAL_TIME_STEPPING-2ND_ORDER, HARMONIC_BALANCE)
TIME_MARCHING= DUAL_TIME_STEPPING-2ND_ORDER
%
% Time Step for dual time stepping simulations (s) -- Only used when UNST_CFL_NUMBER = 0.0
```

```
% For the DG-FEM solver it is used as a synchronization time when UNST_CFL_NUMBER != 0.0
TIME_STEP= 0.00025
%
% Total Physical Time for dual time stepping simulations (s)
MAX_TIME= 8000.0
%
% Unsteady Courant-Friedrichs-Lewy number of the finest grid
UNST_CFL_NUMBER= 0.0
%
%%  Windowed output time averaging
% Time iteration to start the windowed time average in a direct run
WINDOW_START_ITER = 324500
%
% Window used for reverse sweep and direct run. Options (SQUARE, HANN, HANN_SQUARE, BUMP)
WINDOW_FUNCTION = SQUARE
%% Number of internal iterations (dual time method)
INNER_ITER= 40
% Iteration number to begin unsteady restarts
RESTART_ITER= 324001

% -------------------- BOUNDARY CONDITION DEFINITION -------------------------%
%
%
% Navier-Stokes (no-slip), constant heat flux wall  marker(s) (NONE = no marker)
% Format: ( marker name, constant heat flux (J/m^2), ... )
MARKER_HEATFLUX= ( airfoil, 0.0 )
%
% Navier-Stokes (no-slip), isothermal wall marker(s) (NONE = no marker)
% Format: ( marker name, constant wall temperature (K), ... )
MARKER_ISOTHERMAL= ( NONE )
%
% Far-field boundary marker(s) (NONE = no marker)
MARKER_FAR= ( farfield )
%
MARKER_PERIODIC= ( front, back, 0.0, 0.0, 0.0, 0.0, 0.0, 0.0, 0.0, 0.45, 0.0)
% Symmetry boundary marker(s) (NONE = no marker)
%MARKER_SYM= ( Sym1, Sym2 )
```

```
%
% Marker(s) of the surface in the surface flow solution file

MARKER_PLOTTING = ( airfoil )
%MARKER_PLOTTING = ( Sym2 )
%
% Marker(s) of the surface where the non-dimensional coefficients are evaluated.
MARKER_MONITORING = ( airfoil )
%
% Marker(s) of the surface where obj. func. (design problem) will be evaluated
MARKER_DESIGNING = ( airfoil )

% ------------- COMMON PARAMETERS TO DEFINE THE NUMERICAL METHOD --------------%
% Numerical method for spatial gradients (GREEN_GAUSS, LEAST_SQUARES,
%                                         WEIGHTED_LEAST_SQUARES)
NUM_METHOD_GRAD= WEIGHTED_LEAST_SQUARES
%NUM_METHOD_GRAD= GREEN_GAUSS
%
% Courant-Friedrichs-Lewy condition of the finest grid
CFL_NUMBER= 10.0
%
% Adaptive CFL number (NO, YES)
CFL_ADAPT= YES
%
% Parameters of the adaptive CFL number (factor down, factor up, CFL min value,
%                                        CFL max value )
CFL_ADAPT_PARAM= ( 1.0, 1.05, 1.25, 50.0 )
%
% Runge-Kutta alpha coefficients
RK_ALPHA_COEFF= ( 0.66667, 0.66667, 1.000000 )
%
% Number of total iterations
TIME_ITER= 365001
%ITER=500000
%%
% ------------------------ LINEAR SOLVER DEFINITION ---------------------------%
%
% Linear solver or smoother for implicit formulations (BCGSTAB, FGMRES, SMOOTHER_JACOBI,
```

```
%                                                       SMOOTHER_ILU0, SMOOTHER_LUSGS,
%                                                       SMOOTHER_LINELET)
LINEAR_SOLVER= FGMRES
%
% Preconditioner of the Krylov linear solver (ILU0, LU_SGS, LINELET, JACOBI)
LINEAR_SOLVER_PREC= ILU
%LINEAR_SOLVER_ILU_FILL_IN= 0
%
% Minimum error of the linear solver for implicit formulations
LINEAR_SOLVER_ERROR= 1E-6
%
% Max number of iterations of the linear solver for the implicit formulation
LINEAR_SOLVER_ITER= 20
%
% -------------------- FLOW NUMERICAL METHOD DEFINITION -----------------------%
%
% Convective numerical method (JST, LAX-FRIEDRICH, CUSP, ROE, AUSM, HLLC,
%                              TURKEL_PREC, MSW)
CONV_NUM_METHOD_FLOW=JST
%CONV_NUM_METHOD_FLOW= ROE
%ROE_LOW_DISSIPATION= NTS
%
% Spatial numerical order integration (1ST_ORDER, 2ND_ORDER, 2ND_ORDER_LIMITER)
MUSCL_FLOW= NO
%MUSCL_FLOW= NO
%
% Slope limiter (VENKATAKRISHNAN, BARTH_JESPERSEN)
%SLOPE_LIMITER_FLOW=VENKATAKRISHNAN
SLOPE_LIMITER_FLOW=NONE
%
% Entropy fix coefficient (0.0 implies no entropy fixing, 1.0 implies scalar
%                          artificial dissipation)
ENTROPY_FIX_COEFF= 0.0
%
% 1st, 2nd and 4th order artificial dissipation coefficients
%AD_COEFF_FLOW= ( 0.15, 0.5, 0.02 )
%
% Viscous limiter (NO, YES)
```

```
%VISCOUS_LIMITER_FLOW= NO
%
% Time discretization (RUNGE-KUTTA_EXPLICIT, EULER_IMPLICIT, EULER_EXPLICIT)
TIME_DISCRE_FLOW= EULER_IMPLICIT
%
% Relaxation coefficient
%RELAXATION_FACTOR_FLOW= 1.0
%
% JST dissipation coefficient
JST_SENSOR_COEFF = (0.5, 0.001)

% -------------------- TURBULENT NUMERICAL METHOD DEFINITION ------------------%
%
% Convective numerical method (SCALAR_UPWIND)
CONV_NUM_METHOD_TURB= SCALAR_UPWIND
%
% Spatial numerical order integration (1ST_ORDER, 2ND_ORDER, 2ND_ORDER_LIMITER)
MUSCL_TURB= NO
%
% Slope limiter (VENKATAKRISHNAN)
SLOPE_LIMITER_TURB= NONE
%
% Viscous limiter (NO, YES)
%VISCOUS_LIMITER_TURB= NO
%
% Time discretization (EULER_IMPLICIT)
TIME_DISCRE_TURB= EULER_IMPLICIT
%
% Reduction factor of the CFL coefficient in the turbulence problem
%CFL_REDUCTION_TURB= 1.0
%
% Relaxation coefficient
%RELAXATION_FACTOR_TURB= 1.0

% ------------------------------ SOLVER CONTROL -----------------------------%
%
% Convergence field
CONV_FIELD= RMS_DENSITY
```

```
%
% Min value of the residual (log10 of the residual)
CONV_RESIDUAL_MINVAL= -14
%
% Start convergence criteria at iteration number
CONV_STARTITER= 0
%
% Number of elements to apply the criteria
CONV_CAUCHY_ELEMS= 100
%
% Epsilon to control the series convergence
CONV_CAUCHY_EPS= 1E-5
%

% ------------------------ GRID ADAPTATION STRATEGY -------------------------%
%
% Percentage of new elements (% of the original number of elements)
%NEW_ELEMS= 5
%
% Kind of grid adaptation (NONE, PERIODIC, FULL, FULL_FLOW, GRAD_FLOW, FULL_ADJOINT,
%                          GRAD_ADJOINT, GRAD_FLOW_ADJ, ROBUST,
%                          FULL_LINEAR, COMPUTABLE, COMPUTABLE_ROBUST,
%                          REMAINING, WAKE, SMOOTHING, SUPERSONIC_SHOCK,
%                          TWOPHASE)
%KIND_ADAPT= PERIODIC
%
% Scale factor for the dual volume
%DUALVOL_POWER= 0.5
%
% Adapt the boundary elements (NO, YES)
%ADAPT_BOUNDARY= YES

% ------------------------ INPUT/OUTPUT FILE INFORMATION --------------------------%
%
% Mesh input file
MESH_FILENAME= /scratch-shared/hozdemir/naca12_UoB/freq1/Mesh_naca0012_clean_Ogrid.su2
%
% Mesh input file format (SU2, CGNS)
```

```
MESH_FORMAT= SU2
%
% Mesh output file
MESH_OUT_FILENAME= mesh_out.su2
%
% Restart flow input file
SOLUTION_FILENAME= restart/restart_flow.dat
%
% Restart adjoint input file
SOLUTION_ADJ_FILENAME= solution_adj.dat
%
% Output tabular file format (TECPLOT, CSV)
TABULAR_FORMAT= CSV
%
% Files to output
% Possible formats : (TECPLOT, TECPLOT_BINARY, SURFACE_TECPLOT,
%  SURFACE_TECPLOT_BINARY, CSV, SURFACE_CSV, PARAVIEW, PARAVIEW_BINARY, SURFACE_PARAVIEW,
%  SURFACE_PARAVIEW_BINARY, MESH, RESTART_BINARY, RESTART_ASCII, CGNS, STL)
% default : (RESTART, PARAVIEW, SURFACE_PARAVIEW)
%OUTPUT_FILES= (RESTART, SURFACE_PARAVIEW)
OUTPUT_FILES= (RESTART, PARAVIEW, SURFACE_PARAVIEW)
%
% Output file convergence history (w/o extension)
CONV_FILENAME= history
%
% Output file with the forces breakdown
BREAKDOWN_FILENAME= forces/forces_breakdown.dat
%
% Output file restart flow
RESTART_FILENAME= restart/restart_flow.dat
%
% Output file restart adjoint
RESTART_ADJ_FILENAME= restart_adj.dat
%
% Output file flow (w/o extension) variables
VOLUME_FILENAME= flow/flow
%
% Output file adjoint (w/o extension) variables
```

```
VOLUME_ADJ_FILENAME= adjoint
%
% Output Objective function
VALUE_OBJFUNC_FILENAME= of_eval.dat
%
% Output objective function gradient (using continuous adjoint)
GRAD_OBJFUNC_FILENAME= of_grad.dat
%
% Output file surface flow coefficient (w/o extension)
SURFACE_FILENAME= surface/surface_flow
%
% Output file surface adjoint coefficient (w/o extension)
SURFACE_ADJ_FILENAME= surface_adjoint
%
% Read binary restart files (YES, NO)
%READ_BINARY_RESTART= YES
%
% Writing convergence history frequency (dual time, only written to screen)
WRT_PERFORMANCE= YES
%
% Writing frequency for volume/surface output
%OUTPUT_WRT_FREQ= 1000
%OUTPUT_FILES= (RESTART, PARAVIEW, SURFACE_PARAVIEW)
OUTPUT_WRT_FREQ= 1000, 1000, 1
%
WRT_FORCES_BREAKDOWN=YES
%
SCREEN_OUTPUT=(TIME_ITER,INNER_ITER,RMS_DENSITY,RMS_MOMENTUM-X,RMS_NU_TILDE,LIFT,DRAG)
%
HISTORY_OUTPUT=(ITER, RMS_RES,AERO_COEFF)
%
VOLUME_OUTPUT=(TIME_AVERAGE,COORDINATES,PRIMITIVE)
```

A.2 CASE 2

```
%%%%%%%%%%%%%%%%%%%%%%%%%%%%%%%%%%%%%%%%%%%%%%%%%%%%%%%%%%%%%%%%%%%%%%%%%%%%%%%%
%                                                                              %
```

```
% Stanford University unstructured (SU2) configuration file                    %
% Case description: CASE 2 NACA0012                                            %
% Author: Michael Zaki                                                        %
% Institution:      %
% Date:                                                                        %
% File Version SU2 v5.0                                                        %
%                                                                              %
%%%%%%%%%%%%%%%%%%%%%%%%%%%%%%%%%%%%%%%%%%%%%%%%%%%%%%%%%%%%%%%%%%%%%%%%%%%%%%%

% ------------- DIRECT, ADJOINT, AND LINEARIZED PROBLEM DEFINITION ------------%
%
% Physical governing equations (POTENTIAL_FLOW, EULER, NAVIER_STOKES,
%                               MULTI_SPECIES_NAVIER_STOKES, TWO_PHASE_FLOW,
%                               COMBUSTION)
SOLVER= RANS
%
% Specify turbulence model (NONE, SA, SA_NEG, SST)
KIND_TURB_MODEL= SA
%
% Specify Hybrid RANS/LES for SA family (NONE, SADES, SADDES)
%HYBRID_RANSLES= NONE
HYBRID_RANSLES= SA_EDDES
%
% DES Constant (0.65)
DES_CONST= 0.65
%
% Mathematical problem (DIRECT, ADJOINT, LINEARIZED, ONE_SHOT_ADJOINT)
MATH_PROBLEM= DIRECT
%
% Restart solution (NO, YES)
RESTART_SOL= YES
% Compute the average solution for unsteady simulations (NO, YES)
COMPUTE_AVERAGE= YES
%
% Restart the average process from a previous averaged solution (NO, YES)
%RESTART_AVERAGE= NO
%
% ----------- COMPRESSIBLE AND INCOMPRESSIBLE FREE-STREAM DEFINITION ----------%
```

```
%
% Mach number (non-dimensional, based on the free-stream values)
MACH_NUMBER= 0.145772
%
% Angle of attack (degrees)
AOA= 15
%
% Side-slip angle (degrees)
SIDESLIP_ANGLE= 0.0
%
% Free-stream pressure (101325.0 N/m^2 by default, only Euler flows)
%FREESTREAM_PRESSURE= 101325
%
% Free-stream temperature (273.15 K by default)
FREESTREAM_TEMPERATURE= 293
%
% Reynolds number (non-dimensional, based on the free-stream values)
REYNOLDS_NUMBER=  4.1E5
%
% Reynolds length (1 m, 1 inch by default)
REYNOLDS_LENGTH= 1

% -------------- COMPRESSIBLE AND INCOMPRESSIBLE FLUID CONSTANTS --------------%
%
% Different gas model (STANDARD_AIR, IDEAL_GAS, VW_GAS, PR_GAS)
FLUID_MODEL= STANDARD_AIR
%
% Ratio of specific heats (1.4 (air), only for compressible flows)
GAMMA_VALUE= 1.4
%
% Specific gas constant (287.87 J/kg*K (air), only for compressible flows)
GAS_CONSTANT= 287.87

% ---------------------- REFERENCE VALUE DEFINITION --------------------------%
%
% Reference origin for moment computation
REF_ORIGIN_MOMENT_X = 0.25
REF_ORIGIN_MOMENT_Y = 0.00
```

```
REF_ORIGIN_MOMENT_Z = 0.00
%
% Reference length for pitching, rolling, and yawing non-dimensional moment
REF_LENGTH= 1.0
%
% Reference area for force coefficients (0 implies automatic calculation)
REF_AREA=0
%
% Flow non-dimensionalization (DIMENSIONAL, FREESTREAM_PRESS_EQ_ONE,
%                              FREESTREAM_VEL_EQ_MACH, FREESTREAM_VEL_EQ_ONE)
REF_DIMENSIONALIZATION= DIMENSIONAL
%REF_DIMENSIONALIZATION= FREESTREAM_PRESS_EQ_ONE
%
% ------------------------ TIME-DEPENDENT SIMULATION -----------------------------%
%
% Time domain simulation
TIME_DOMAIN= YES
%TIME_DOMAIN= NO
%
% Unsteady simulation (NO, TIME_STEPPING, DUAL_TIME_STEPPING-1ST_ORDER,
%                      DUAL_TIME_STEPPING-2ND_ORDER, HARMONIC_BALANCE)
TIME_MARCHING= DUAL_TIME_STEPPING-2ND_ORDER
%
% Time Step for dual time stepping simulations (s) -- Only used when UNST_CFL_NUMBER = 0.0
% For the DG-FEM solver it is used as a synchronization time when UNST_CFL_NUMBER != 0.0
TIME_STEP= 0.00025
%
% Total Physical Time for dual time stepping simulations (s)
MAX_TIME= 8000.0
%
% Unsteady Courant-Friedrichs-Lewy number of the finest grid
UNST_CFL_NUMBER= 0.0
%
%%  Windowed output time averaging
% Time iteration to start the windowed time average in a direct run
WINDOW_START_ITER = 100500
%
% Window used for reverse sweep and direct run. Options (SQUARE, HANN, HANN_SQUARE, BUMP) Squa
```

```
WINDOW_FUNCTION = SQUARE
%% Number of internal iterations (dual time method)
INNER_ITER= 40
% Iteration number to begin unsteady restarts
RESTART_ITER= 100001

% -------------------- BOUNDARY CONDITION DEFINITION -------------------------%
%
%
% Navier-Stokes (no-slip), constant heat flux wall  marker(s) (NONE = no marker)
% Format: ( marker name, constant heat flux (J/m^2), ... )
MARKER_HEATFLUX= ( airfoil, 0.0 )
%
% Navier-Stokes (no-slip), isothermal wall marker(s) (NONE = no marker)
% Format: ( marker name, constant wall temperature (K), ... )
MARKER_ISOTHERMAL= ( NONE )
%
% Far-field boundary marker(s) (NONE = no marker)
MARKER_FAR= ( farfield )
%
%MARKER_PERIODIC= ( front, back, 0.0, 0.0, 0.0, 0.0, 0.0, 0.0, 0.0, 0.45, 0.0)
% Symmetry boundary marker(s) (NONE = no marker)
MARKER_SYM= ( front, back )

%
% Marker(s) of the surface in the surface flow solution file

MARKER_PLOTTING = ( airfoil )
%MARKER_PLOTTING = ( Sym2 )
%
% Marker(s) of the surface where the non-dimensional coefficients are evaluated.
MARKER_MONITORING = ( airfoil )
%
% Marker(s) of the surface where obj. func. (design problem) will be evaluated
MARKER_DESIGNING = ( airfoil )

% ------------- COMMON PARAMETERS TO DEFINE THE NUMERICAL METHOD -------------%
% Numerical method for spatial gradients (GREEN_GAUSS, LEAST_SQUARES,
```

```
%                                          WEIGHTED_LEAST_SQUARES)
NUM_METHOD_GRAD= WEIGHTED_LEAST_SQUARES
%NUM_METHOD_GRAD= GREEN_GAUSS
%
% Courant-Friedrichs-Lewy condition of the finest grid
CFL_NUMBER= 10.0
%
% Adaptive CFL number (NO, YES)
CFL_ADAPT= YES
%
% Parameters of the adaptive CFL number (factor down, factor up, CFL min value,
%                                        CFL max value )
CFL_ADAPT_PARAM= ( 1.0, 1.05, 1.25, 50.0 )
%
% Runge-Kutta alpha coefficients
RK_ALPHA_COEFF= ( 0.66667, 0.66667, 1.000000 )
%
% Number of total iterations
TIME_ITER= 365001
%ITER=500000
%%
% ------------------------ LINEAR SOLVER DEFINITION ----------------------------%
%
% Linear solver or smoother for implicit formulations (BCGSTAB, FGMRES, SMOOTHER_JACOBI,
%                                                      SMOOTHER_ILU0, SMOOTHER_LUSGS,
%                                                      SMOOTHER_LINELET)
LINEAR_SOLVER= FGMRES
%
% Preconditioner of the Krylov linear solver (ILU0, LU_SGS, LINELET, JACOBI)
LINEAR_SOLVER_PREC= ILU
%LINEAR_SOLVER_ILU_FILL_IN= 0
%
% Minimum error of the linear solver for implicit formulations
LINEAR_SOLVER_ERROR= 1E-6
%
% Max number of iterations of the linear solver for the implicit formulation
LINEAR_SOLVER_ITER= 20
%
```

```
% -------------------- FLOW NUMERICAL METHOD DEFINITION ----------------------%
%
% Convective numerical method (JST, LAX-FRIEDRICH, CUSP, ROE, AUSM, HLLC,
%                              TURKEL_PREC, MSW)
CONV_NUM_METHOD_FLOW=JST
%CONV_NUM_METHOD_FLOW= ROE
%ROE_LOW_DISSIPATION= NTS
%
% Spatial numerical order integration (1ST_ORDER, 2ND_ORDER, 2ND_ORDER_LIMITER)
MUSCL_FLOW= NO
%MUSCL_FLOW= NO
%
% Slope limiter (VENKATAKRISHNAN, BARTH_JESPERSEN)
%SLOPE_LIMITER_FLOW=VENKATAKRISHNAN
SLOPE_LIMITER_FLOW=NONE
%
% Entropy fix coefficient (0.0 implies no entropy fixing, 1.0 implies scalar
%                          artificial dissipation)
ENTROPY_FIX_COEFF= 0.0
%
% 1st, 2nd and 4th order artificial dissipation coefficients
%AD_COEFF_FLOW= ( 0.15, 0.5, 0.02 )
%
% Viscous limiter (NO, YES)
%VISCOUS_LIMITER_FLOW= NO
%
% Time discretization (RUNGE-KUTTA_EXPLICIT, EULER_IMPLICIT, EULER_EXPLICIT)
TIME_DISCRE_FLOW= EULER_IMPLICIT
%
% Relaxation coefficient
%RELAXATION_FACTOR_FLOW= 1.0
%
% JST dissipation coefficient
JST_SENSOR_COEFF = (0.5, 0.001)

% -------------------- TURBULENT NUMERICAL METHOD DEFINITION ------------------%
%
% Convective numerical method (SCALAR_UPWIND)
```

```
CONV_NUM_METHOD_TURB= SCALAR_UPWIND
%
% Spatial numerical order integration (1ST_ORDER, 2ND_ORDER, 2ND_ORDER_LIMITER)
MUSCL_TURB= NO
%
% Slope limiter (VENKATAKRISHNAN)
SLOPE_LIMITER_TURB= NONE
%
% Viscous limiter (NO, YES)
%VISCOUS_LIMITER_TURB= NO
%
% Time discretization (EULER_IMPLICIT)
TIME_DISCRE_TURB= EULER_IMPLICIT
%
% Reduction factor of the CFL coefficient in the turbulence problem
%CFL_REDUCTION_TURB= 1.0
%
% Relaxation coefficient
%RELAXATION_FACTOR_TURB= 1.0

% ------------------------------ SOLVER CONTROL ------------------------------%
%
% Convergence field
CONV_FIELD= RMS_DENSITY
%
% Min value of the residual (log10 of the residual)
CONV_RESIDUAL_MINVAL= -14
%
% Start convergence criteria at iteration number
CONV_STARTITER= 0
%
% Number of elements to apply the criteria
CONV_CAUCHY_ELEMS= 100
%
% Epsilon to control the series convergence
CONV_CAUCHY_EPS= 1E-5
%
```

```
% ------------------------ GRID ADAPTATION STRATEGY -------------------------%
%
% Percentage of new elements (% of the original number of elements)
%NEW_ELEMS= 5
%
% Kind of grid adaptation (NONE, PERIODIC, FULL, FULL_FLOW, GRAD_FLOW, FULL_ADJOINT,
%                          GRAD_ADJOINT, GRAD_FLOW_ADJ, ROBUST,
%                          FULL_LINEAR, COMPUTABLE, COMPUTABLE_ROBUST,
%                          REMAINING, WAKE, SMOOTHING, SUPERSONIC_SHOCK,
%                          TWOPHASE)
%KIND_ADAPT= PERIODIC
%
% Scale factor for the dual volume
%DUALVOL_POWER= 0.5
%
% Adapt the boundary elements (NO, YES)
%ADAPT_BOUNDARY= YES

% ------------------------ INPUT/OUTPUT FILE INFORMATION --------------------------%
%
% Mesh input file
MESH_FILENAME= /scratch-shared/hozdemir/naca12/12cm_chord/freq1/naca12_ext_scaled.su2
%
% Mesh input file format (SU2, CGNS)
MESH_FORMAT= SU2
%
% Mesh output file
MESH_OUT_FILENAME= mesh_out.su2
%
% Restart flow input file
SOLUTION_FILENAME= restart/restart_flow.dat
%
% Restart adjoint input file
SOLUTION_ADJ_FILENAME= solution_adj.dat
%
% Output tabular file format (TECPLOT, CSV)
TABULAR_FORMAT= CSV
%
```

```
% Files to output
% Possible formats : (TECPLOT, TECPLOT_BINARY, SURFACE_TECPLOT,
%  SURFACE_TECPLOT_BINARY, CSV, SURFACE_CSV, PARAVIEW, PARAVIEW_BINARY, SURFACE_PARAVIEW,
%  SURFACE_PARAVIEW_BINARY, MESH, RESTART_BINARY, RESTART_ASCII, CGNS, STL)
% default : (RESTART, PARAVIEW, SURFACE_PARAVIEW)
%OUTPUT_FILES= (RESTART, SURFACE_PARAVIEW)
OUTPUT_FILES= (RESTART, PARAVIEW, SURFACE_PARAVIEW)
%
% Output file convergence history (w/o extension)
CONV_FILENAME= history
%
% Output file with the forces breakdown
BREAKDOWN_FILENAME= forces/forces_breakdown.dat
%
% Output file restart flow
RESTART_FILENAME= restart/restart_flow.dat
%
% Output file restart adjoint
RESTART_ADJ_FILENAME= restart_adj.dat
%
% Output file flow (w/o extension) variables
VOLUME_FILENAME= flow/flow
%
% Output file adjoint (w/o extension) variables
VOLUME_ADJ_FILENAME= adjoint
%
% Output Objective function
VALUE_OBJFUNC_FILENAME= of_eval.dat
%
% Output objective function gradient (using continuous adjoint)
GRAD_OBJFUNC_FILENAME= of_grad.dat
%
% Output file surface flow coefficient (w/o extension)
SURFACE_FILENAME= surface/surface_flow
%
% Output file surface adjoint coefficient (w/o extension)
SURFACE_ADJ_FILENAME= surface_adjoint
%
```

```
% Read binary restart files (YES, NO)
%READ_BINARY_RESTART= YES
%
% Writing convergence history frequency (dual time, only written to screen)
WRT_PERFORMANCE= YES
%
% Writing frequency for volume/surface output
%OUTPUT_WRT_FREQ= 1000
%OUTPUT_FILES= (RESTART, PARAVIEW, SURFACE_PARAVIEW)
OUTPUT_WRT_FREQ= 1000, 1000, 1
%
WRT_FORCES_BREAKDOWN=YES
%
SCREEN_OUTPUT=(TIME_ITER,INNER_ITER,RMS_DENSITY,RMS_MOMENTUM-X,RMS_NU_TILDE,LIFT,DRAG)
%
HISTORY_OUTPUT=(ITER, RMS_RES,AERO_COEFF)
%
VOLUME_OUTPUT=(TIME_AVERAGE,COORDINATES,PRIMITIVE)
```